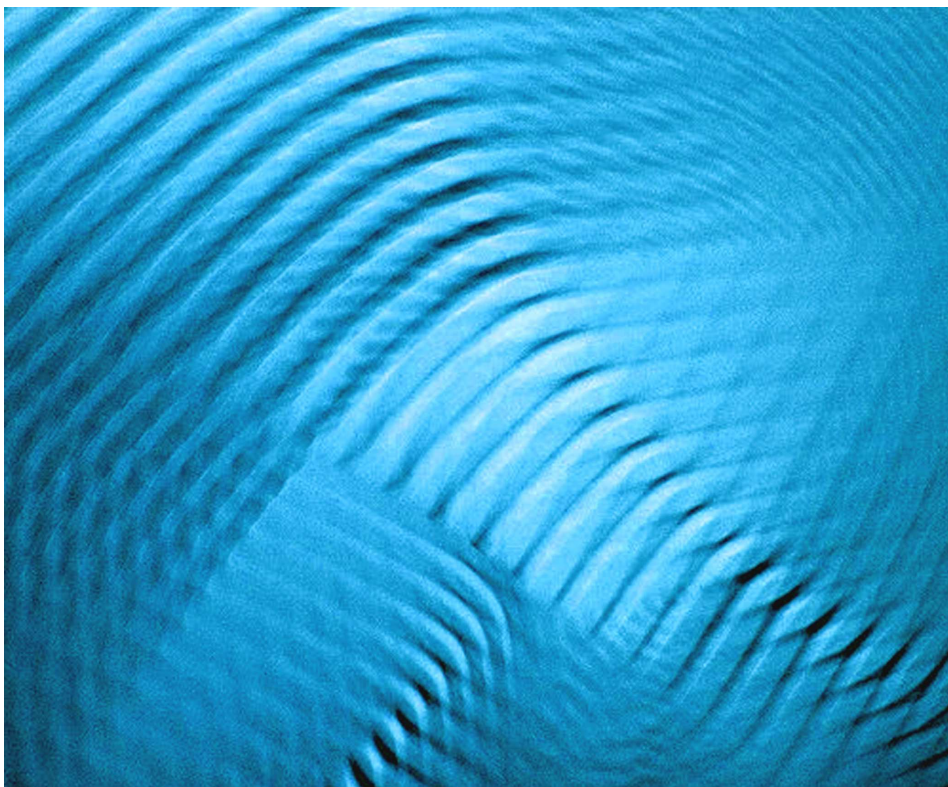


Master of Science Thesis

Aeroacoustic Investigation of Rod-Airfoil Noise based on Time-Resolved PIV

Valerio Lorenzoni

December 27, 2008



Aeroacoustic Investigation of Rod-Airfoil Noise based on Time-Resolved PIV

Master of Science Thesis

For obtaining the degree of Master of Science in Aerospace Engineering
at Delft University of Technology

Valerio Lorenzoni

December 27, 2008



Delft University of Technology

Copyright © Aerospace Engineering, Delft University of Technology
All rights reserved.

DELFT UNIVERSITY OF TECHNOLOGY
DEPARTMENT OF AERODYNAMICS

The undersigned hereby certify that they have read and recommend to the Faculty of Aerospace Engineering for acceptance the thesis entitled “**Aeroacoustic Investigation of Rod-Airfoil Noise based on Time-Resolved PIV**” by **Valerio Lorenzoni** in fulfillment of the requirements for the degree of **Master of Science**.

Dated: December 27, 2008

Examination committee:

prof. dr. ir. F. Scarano

dr. ir. C. Schram

dr. ir. B. W. van Oudheusden

ir. P. Moore

ir. M. Tuinstra

“Indeed one could hardly expect, even with the great advances in knowledge of turbulent flows which have lately been made, that such a theory could be used with confidence to predict acoustic intensities within a factor much less than 10. But, on the other hand, one could certainly make no confident estimate even to within a factor of 1000 on existing knowledge, and further, the range of intensities in which one is interested is at least 10^{14} .”

Sir James Lighthill (1952) in, *On Sound Generated Aerodynamically I.*

Preface

Aeroacoustics has stimulated the interest of the author for many years. The most interesting aspect of this subject is that of being an extremely specific branch of the aerodynamic research field and at the same time having an incredibly wide range of applicability. It represents the bridge between aerodynamic and acoustic theories and provides the key to understand the physics of several acoustic phenomena ranging from jet noise, to rocket launcher resonances, to sound generation in wind instruments.

The present work can be considered as the pilot-test of a long term European Project called FLOVIST (*Flow Visualization Inspired Aero-acoustics with Time-resolved Tomographic Particle Image Velocimetry*) which sees the collaboration of Delft University of Technology (TU Delft) and the Dutch National Aerospace Laboratory (NLR). The innovative purpose of the project is the investigation of aeroacoustic phenomena from an experimental point of view.

The author would like to thank his supervisor Prof. Fulvio Scarano for the fatherly and stimulating support during the whole master education and for the opportunity to choose this aeroacoustic topic as final MSc. thesis project, although quite new for the aerospace faculty. Special thanks are given to Prof. A. Hirshberg for introducing the author to the aeroacoustic world and for his constant priceless availability, and to dr. C. Schram for the highly productive pleasant and illuminating collaboration during the internship period. Many words of gratitude have to be given to Marthijn Tunistra for the strong friendly collaboration and the long, sometimes philosophical, aeroacoustic discussions during and after the experimental campaign. Thanks a lot to Peter Moore for the big help in improving the aeroacoustic code and in the analysis of the results, including the small controversies that at the end, further helped me improving the work by looking at it from different points of view. Grazie anche ad Andrea Turella per il lungo tempo speso nel cercare di aiutarmi con il calcolo delle pressioni...quando ancora tutto sembrava lontanissimo e grazie a Peppe per il suo impagabile ed onnipresente aiuto...soprattutto nel farmi notare dei dettagli a cui da solo non arriverei mai a pensare!

Valerio Lorenzoni

Abstract

The rod-airfoil configuration is a benchmark test case for aeroacoustic assessments of vortex-structure interaction noise. Several industrial devices are arranged in such a way that downstream bodies are embedded in the wake of upstream bodies, such as gas turbines, high lift devices, helicopters among others. Aeroacoustic predictions usually rely on time dependent flow field information obtained from CFD for the determination of the aeroacoustic sources. The present work proposes a novel approach for the aeroacoustic prediction of rod-airfoil noise based on time-resolved PIV experimental data.

The aeroacoustic emission of a NACA0012 airfoil in the Karman wake of a rod is investigated by means of 2D TR-PIV in combination with beamforming and microphone measurements. First the time evolving velocity field around the airfoil is measured using high-speed PIV. The corresponding pressure field is then deduced by spatial integration of a Poisson-based algorithm for quasi-2D incompressible flows. Pressure and velocity computed on specific surfaces around the airfoil constitute the source terms of the implemented Curle's and Ffowkes Williams-Hawkings's aeroacoustic analogies. The calculated Sound Pressure Level (SPL) is compared with the measurements obtained by far field microphones. Velocity visualizations in the spanwise direction provide qualitative information about the phase coherence of the vortical impingement along the airfoil span. Parametric studies are performed to evaluate the effect on the acoustic prediction of the position of the integration surface and the numerical discretization methods employed.

The vortex release-impinging mechanism revealed to be the main cause of the noise emission. Beamforming visualizations confirmed the major contribution of the airfoil to the total noise radiation. All the calculated acoustic spectra exhibit a main peak corresponding to the rod-shedding frequency. The high frequency components are the most affected by numerical and experimental noise. If the analysis is focused on the tonal peak of the computed spectra the method reveals an accuracy within 10 % of the measured SPL, varying with the spanwise correlation length. This provides good prospects for developments of experimental PIV-based aeroacoustic investigations.

Sommario

L'aeroacustica è la scienza che investiga l'emissione sonora dovuta a fenomeni di natura aerodinamica. L'interazione di un flusso turbolento con strutture solide è causa di emissioni acustiche ad alta intensità. Tipici esempi sono rappresentati da sistemi di ventilazione, dispositivi supplementari di portanza, rotori di elicotteri, ecc. Un tipico modello semplificato di interazione flusso-struttura è rappresentato dalla configurazione cilindro-profilo alare. Le moderne tecniche di indagine in campo aeroacustico sono in gran parte basate sulla determinazione del campo fluidodinamico attraverso metodi numerici (Computational Fluid Dynamics, (CFD)). L'aspetto innovativo del presente lavoro è l'utilizzo di misure sperimentali per la valutazione del campo (aero)acustico.

L'analisi è stata condotta su un profilo alare NACA0012 nella scia di un cilindro di diametro uguale alla metà del massimo spessore del profilo, per velocità di 10 e 15 m/s . Il campo di velocità intorno al profilo è stato misurato con tecniche di velocimetria (Particle Image Velocimetry, (PIV)) ad alta frequenza di acquisizione (2.7 kHz); visualizzazione e quantificazione delle sorgenti acustiche sono state realizzate per mezzo di "Beamforming array" ed ulteriori misure microfoniche. Il relativo campo di pressione è stato ottenuto per mezzo dell'integrazione spaziale dell'equazione di Poisson per flussi instazionari nell'ipotesi di quasi-bidimensionalità ed incomprimibilità. Pressione e velocità evaluate su diverse superfici intorno al profilo hanno costituito i termini forzanti delle analogie aeroacustiche di Curle e Ffowcs Williams-Hawkings.

L'indagine ha rivelato che la maggior parte dell'emissione sonora è dovuta al processo di interazione dei vortici con la superficie del profilo. Le visualizzazioni per mezzo di sistemi di microfoni hanno permesso la localizzazione delle principali sorgenti di rumore sulla parte anteriore del profilo. Gli spettri calcolati per mezzo delle analogie aeroacustiche presentano un picco di ampiezza in corrispondenza di una frequenza leggermente inferiore alla frequenza di Strouhal del cilindro. La notevole ampiezza delle componenti spettrali ad alta frequenza è stata attribuita a rumore numerico e ad incertezze di tipo sperimentale. Il confronto del picco di ampiezza con misure microfoniche, in posizioni corrispondenti, rivela un'accuratezza del metodo del 90 %. I risultati positivi della presente investigazione confermano l'applicabilità della tecnica PIV in campo aeroacustico.

Table of Contents

Preface	vii
Abstract	ix
Sommario	xi
1 Introduction	1
2 Aeroacoustics	5
2.1 Sound and properties of sound	7
2.2 Aeroacoustic analogies	9
2.3 Lighthill's analogy	10
2.4 Curle's analogy	14
2.4.1 Compact-body assumption and properties of a dipolar source	16
2.5 Ffowcs Williams-Hawkings analogy	19
3 Experimental Techniques	25
3.1 Short historical background	25
3.2 Particle Image Velocimetry	26
3.2.1 Seeding	27
3.2.2 Illumination	29
3.2.3 Imaging	30
3.2.4 Recording	32
3.2.5 Image analysis	32
3.2.6 Time-resolved PIV (TR-PIV)	36
3.3 Microphone measurements	37
3.3.1 Condenser microphones	37
3.3.2 Microphone sensitivity	37
3.4 Acoustic source localization techniques	41
3.4.1 Time-domain beamforming	42
3.4.2 Frequency-domain Beamforming	44

4	Experimental campaign	49
4.1	Experimental facility	49
4.2	Acoustic measurement system setup	50
4.3	PIV system setup	52
4.4	Results of the experimental campaign	54
4.4.1	Overall flow visualization	56
4.4.2	Flow visualization around the airfoil	59
4.4.3	Spanwise visualization	65
4.5	Discussion of the results of the experimental campaign	67
5	Data reduction techniques	69
5.1	Planar Pressure Imaging	69
5.1.1	PPI results	70
5.2	Aeroacoustic computation	74
5.2.1	Non-permeable Curle/FW-H	75
5.2.2	Permeable Curle/FW-H	76
5.2.3	Compact body simplification and lift evaluation	78
5.3	Numerical implementation of the algorithm	80
6	Results and discussion	83
6.1	Comparison between non-permeable and permeable surface formulations	83
6.2	Effect of the discrete method used for time derivatives	86
6.3	Influence of the integration surface	87
6.4	Integral loads approach	90
6.5	Radiation directivity	91
6.6	Comparison with the results of Casalino	95
7	Conclusions and recommendations for further investigations	99
7.1	Conclusions	99
7.2	Recommendations for further investigations	102
	Bibliography	105
A	Computational aeroacoustics	109
A.1	Computational methods	110
A.2	Direct Methods	110
A.2.1	DNS	110
A.2.2	LES	111
A.2.3	RANS	111
A.2.4	DES	111
A.3	Hybrid Methods	111
A.3.1	LEE	112

A.3.2	APE	112
A.3.3	SNGR	112
A.3.4	BEM	113
A.3.5	Boundary Conditions	113
A.3.6	Discretization Methods	113
B	Basics of Signal Processing	115
B.1	Relevant Statistical Quantities	115
B.2	Correlations and Spectra	116
B.3	DFT and FFT	117
B.4	Spectrum computation algorithm	117
B.5	Data filtering	118
C	Theory of Vortex Sound	119

Chapter 1

Introduction

Noise is universally recognized as a significant issue in regard to health and living standards. Noise regulations are becoming increasingly restrictive for both industrial and public environments. Complaints about noise due to the increase of air traffic, especially in proximity to urban centers, have led to the introduction of several restrictions for aeronautic companies. The automotive and electronics industries are currently seeking improvements in terms of comfort and usability, directly related to the acoustic properties of their products.

Noise attenuation is often associated with the concept of “acoustic insulation” by means of sound absorbing materials, which is commonly the case in room-acoustics. These insulation techniques usually become expensive and hardly applicable on large scale, for example in the case of airplanes flying over cities or trains passing by. Furthermore the effect of the insulation is confined to only specific locations. Alternative noise reduction techniques aim at suppressing the noise at its origin by directly acting on the causes of it. Controlling the source mechanisms can lead to a more effective and global acoustic reduction. Aeroacoustic studies can be included in the context of this latter approach.

Aeroacoustics investigates the mechanisms of noise generation by fluid flows and provides quantitative estimations of the emitted noise level based on the hydrodynamic characteristics of the flow. It encompasses a wide range of practical applications namely any noise generating configuration characterized by turbulent flows, heated flows or turbulent flows interacting with structures (airplanes, rocket engines, wind instruments, etc.) [27, 26]. Once the noise generating flow mechanisms are identified one could alter the flow features by varying geometric or kinetic parameters in such a way to preclude the “creation” of the hydrodynamic noise sources [52].

Aeroacoustic in aeronautics

In the aeronautic field the main noise generating elements are [42, 49]

- Jet engines
- Aerodynamic rotors (helicopters, windmills, turbofans, etc.)
- Airframe structures (undercarriage, high-lift devices, etc.)

Jet noise has been the first historically investigated aeroacoustic problem which led M. J. Lighthill in 1952 to the development of the *aeroacoustic analogy* [32] for quantitative prediction of the noise emitted by a turbulent flow. Interaction of flow vortical structures with solid boundaries revealed to be a more efficient source of noise with respect to the free turbulence. The analogy of Lighthill was consequently extended to account for the presence of solid boundaries by Curle (1955) [14] and arbitrary surface motion by Ffowcs Williams and Hawkings (1969) [22].



Figure 1.1: Typical examples of noise generating aeronautic systems

The main mechanisms of sound generation in the presence of solid structures can be classified in [43]:

Vortex shedding noise Vorticity released by a bluff body in a flow. The time varying circulation on the body due to vortex release induces a fluctuating force on the body itself which is transferred to the fluid and propagates as sound.

Turbulence-structure interaction noise Vortical structures impinging on a solid surface generate local pressure fluctuations on the body surface which feed the acoustic far field.

Trailing edge noise Particularly important for all rotating blade technologies, due to the interaction of the boundary layers instabilities with the surface edges.

Rod-airfoil configuration

The *rod-airfoil configuration* as test case of combined vortex shedding noise and turbulence-structure interaction noise has been first proposed by the group of L'École Centrale de Lyon constituted by M. Roger, M. Jacobs and D. Casalino. The main advantage of this configuration is that it offers a simplified model for analytical and numerical studies with respect to a

real vortex interaction case, still preserving the main characteristics of the noise generating phenomenon [43, 29].

For Reynolds numbers higher than 50 a rod immersed in a stream sheds a sequence of counter-rotating vortices organized in a stable pattern known as a “von Karman Street” (an extended description of the vortex shedding mechanism behind cylindrical rods has been provided by Williamson in [55]). When a solid body is placed downstream of the rod inside the Karman street, it experiences fluctuating loads which, even for non-vibrating structures, are responsible for noise emissions. Several industrial devices are arranged in such a way that downstream bodies are embedded in the wake of upstream bodies.

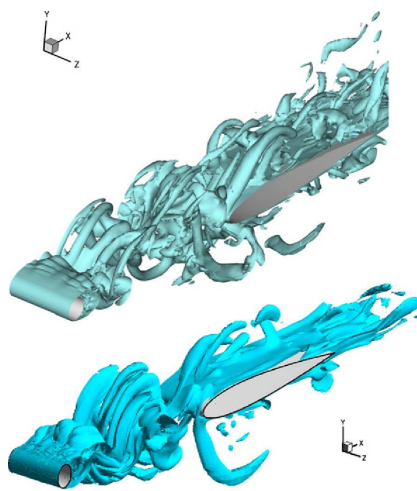


Figure 1.2: 3D visualization of the rod-airfoil interaction mechanism. Iso-vorticity contours [Greschner *et al.*, 2008]

This is typically the case of a bank of heat exchanger tubes, rotor stator configurations of turbo-engines, ventilating systems and helicopter rotors where the blade can interact with the tip-vortices released by preceding blades. Aeroacoustic investigations on a rod-airfoil configuration have been performed by Casalino (2002) [10, 11] by means of URANS simulations for the characterization of the flow field and a permeable Ffowcs Williams-Hawkings aeroacoustic analogy for the noise prediction. The results of the flow simulation were compared with an analytical derivation of the airfoil response at interaction with vortices and the predicted acoustic radiation with far field microphone measurements. Jacob (2004) [29] performed a benchmark analysis of the rod-airfoil configuration based on Large Eddy Simulations (LES) and Unsteady Reynolds Averaged Navier Stokes (URANS) techniques. The numerical simulation were combined with pressure measurements by means of transducers at the air-

foil surface and PIV visualization for detection of the flow structure mainly responsible for the noise emission. Further improvements of the latter prediction method resulted from the implementation of detached eddy simulations (DES) [24] (2008) conducted by the Institute of Fluid Mechanics of the Berlin University of Technology in collaboration with Centre Acoustique du LMFA-UMR of the Ecole Centrale de Lyon and the Italian Aerospace Research Center (C.I.R.A.). Numerical investigations on the same configuration have been performed inside the framework of European Project PROBAND [28]. The results obtained by the application of several computational aeroacoustic (CAA) techniques have been compared with experimental measurements for the assessment on the broadband noise prediction. The specifics of the various numerical techniques are shortly described in Appendix A.

Aeroacoustic investigation techniques

Characterization of the acoustic field is the first step toward the investigation of an aeroacoustic problem. Microphones are the tools usually employed for acoustic measurements. The use

of a single microphone, however, only provides information about the spectral composition of the sound field. The state of the art in experimental aeroacoustics relies on beamforming algorithms and the simultaneous use of arrays of microphones which allow for both the quantification and the spatial localization of the acoustic sources. Beamforming arrays are currently the most powerful experimental tools in aeroacoustic investigations.

An alternative approach to aeroacoustic problems consists in the analytical-numerical extrapolation of the noise radiation from the knowledge of the hydrodynamic characteristics of the flow. Although this methodology is apparently less immediate than the direct measurement of the radiated acoustic field, it provides a deeper insight into the physical processes responsible for the sound generation. The characterization of the sources of noise then becomes one of the crucial points of the aeroacoustic prediction.

The unsteady nature of acoustic propagation requires the knowledge of the time evolution of the aeroacoustic noise sources. This is usually achieved by implementation of high resolution CFD techniques. The innovative aspect of the present analysis is the prediction of noise by use of *time-resolved PIV* for the characterization of the unsteady velocity field. PIV based aeroacoustic predictions have been already successfully carried out by Schram (2003) [45] on the vortex pairing due to acoustically driven instabilities in the shear layer of a subsonic jet, by means of Powell's analogy and Möhring integral formulation. The group of Schröder (2004) [48] performed simultaneous PIV and acoustic measurements on the trailing edge of a flat board at high recording rate for detection of the statistical flow features responsible for the noise emission.

To the knowledge of the author, PIV techniques for aeroacoustic prediction on a rod-airfoil configuration have not previously been employed. The scope of the present work is to demonstrate, within the technical limits of this specific experiment, the feasibility of using time-resolved PIV experimental data for aeroacoustic noise prediction.

The first chapter provides a general introduction to aeroacoustics and the analytical formulation of the aeroacoustic analogies that have been used for the noise computation. Chapter 3 provides a general overview of the experimental techniques adopted during the experimental campaign. Follows in Chapter 4 the description of the experimental facility and the results of the velocity and acoustic measurements. Chapter 5 describes the procedure followed for the implementation of the pressure solver and aeroacoustic algorithms. In Chapter 6 the results of the implementation of the aeroacoustic analogies are presented and a comparison with microphone measurements and data from the literature is provided. Finally in Chapter 7 the general conclusions of the investigation with recommendations for further investigations are drawn.

Chapter 2

Aeroacoustics

Aeroacoustics investigates the aerodynamic generation of sound. Modern aeroacoustic science was initiated in the 1950's with the pioneering work of Sir James Lighthill who derived a theory for the estimation of the *intensity* of sound radiated by a turbulent flow. Prior to this, flow-generated noise studies mainly focused on the relation between the frequency of the fluid fluctuations and the emitted sound.

The “Aeolian Tones”, typical of a wire held in the wind, have historically stimulated scientific and non scientific interest, such that in 18th century the “Aeolian harp” became a common household instrument. The frequency of the aeolian tone was mathematically related to flow parameters by V. Strouhal who, as a result of quantitative observations, introduced the non dimensional frequency known, in honor of him, as the *Strouhal number*. Lord Rayleigh related the Strouhal number to the flow Reynolds number and further recognized that the direction of most intense sound emission coincides with the direction of the fluctuating force on the wire. H. Bernard in 1908 explicitly connected the Strouhal's tone to the eddy pattern of the wake, organized in what we now know as *Karman Wake* after the analytical derivation proposed by T. von Karman (1911) on the stability of the vortex pair configuration. Quantitative estimations of sound emission had not yet been done. In the early 1950's jet aircrafts were about to enter civil service and some pioneer aerodynamicists like E. J Richards [21] foresaw that investigation was needed to study possible acoustic problems connected with jet engines. At that time, when also Ffowcs Williams started working on those, still unclear, aeroacoustic topics, Sir James Lighthill published his master paper *On sound Generated Aerodynamically* (1952) widely recognized as an eloquent expression of elegance and practical usability. The modern field of aeroacoustic is regarded at that point have begun.

The work of Lighthill established the theoretical background generally referred to for investigation of aerodynamic noise [32]. Lighthill first introduced the concept of *aeroacoustic analogy* which consists of replacing the actual noise generating flow field with an equivalent system of noise sources acting on a uniform stagnant fluid governed by standard acoustic propagation equations. The aerodynamic characterization of the sources then becomes the main issue in noise prediction. This work was extended by N. Curle in 1955 [14] to include the effect of flow-body interaction on the sound generation and further generalized by J. E. Ffowcs Williams and D. L. Hawkings at the end of the sixties (1969) [22] to account for arbitrary surface motion. This latter formulation was devised specifically for noise predictions in rotor blades aerodynamics, such as in the helicopter and turbine industries [18, 9].

Sound is produced in a fluid when the existing vortical motion experiences *time variations* in a Lagrangian sense. At equilibrium centrifugal forces are balanced by pressure gradients. When the vortical structures experience rapid inertial variations, i.e. whenever they are forced to reorganize because of interaction with other vortices, shear layers or solid boundaries, local pressure fluctuations are generated. In some cases part of these pressure fluctuations propagate away from the flow region as sound. Free vortex interactions as investigated by Lighthill, have quadrupolar nature and are quite inefficient in terms of sound generation, especially at low Mach numbers, since any fluid tends to compensate a pressure variation with a local reciprocal motion. In the case of vorticity interacting with a solid boundary the reciprocal motion is prevented by the surface, resulting in a dipolar, higher intensity sound generation.¹

Sound radiation is extremely weak compared to fluid pressure fluctuations, in particular at low Mach numbers. A sound pressure level (SPL) of about 120 dB that human beings perceive as “terribly loud” corresponds to an acoustical pressure fluctuation of approximately 20Pa , which is four orders of magnitude lower than the ambient pressure. One of the basic assumptions for aeroacoustic investigations is that the acoustic intensity level is so small compared to the hydrodynamic pressure fluctuations that sound propagation does not influence the main flow. Under this assumption the flow and the acoustics can be decoupled and it is possible to analyze them separately. However, this is not possible when the acoustic fluctuations play a dominant role in the generation of flow instabilities such as in duct flows with the presence of standing-wave resonance patterns or in acoustic-shear layers interaction where Tollmien-Schlichting instabilities in the shear layer can be triggered by acoustic waves. A detailed description of the interaction between flow fluctuations of different nature (hydrodynamic, acoustic and entropy), based on second order expansion of perturbed conservation equations was provided by Chu and Kovásznyai (1958)[43].

Little importance has been given so far to aeroacoustic noise in industry compared to vibration issues. The causes of this lack of interest could be addressed to the masking effect of frame-noise onto flow-induced noise and, first of all, to the complexity of an accurate flow description, in particular, for turbulent flows over complex geometries at the large Reynolds numbers of practical interest. Continuous progress in modern Computational Fluid Dynamics (CFD) techniques allow for an increasingly accurate time-resolved characterization of flow fields down to the smallest flow scales, for moderate Reynolds number. The most common approach in aeroacoustic investigations relies on CFD based descriptions of the *source-flow* field. A brief description of the state of the art in computational aeroacoustics (CAA) is given in Appendix A. Widespread modern aeroacoustic approaches see the combination of numerically derived fluid parameters with wave propagation solvers in the framework of what is called an *Hybrid Method*.

The innovative aspect of the present work is the use of experimental PIV data for the flow characterization at relatively high Reynolds numbers. The acoustic propagation was obtained exploiting Curle’s analogy, in both discrete and integral formulation, and the Ffowcs-Williams Hawkins analogy.

¹This can be easily verified by putting a finger in front of our mouth while blowing.

2.1 Sound and properties of sound

A sounding object produces local pressure fluctuations of the air particles surrounding it. These local fluctuations propagate as isentropic energy-carrying waves, called *sound waves*. One commonly refers to *sound* when the waves are organized in a *well structured* harmonic sequence at “pleasant” audible levels, like in the case of musical instruments², and to *noise* when dealing with an unstructured spectral composition at relatively high intensity level. The propagation velocity is determined by the properties of the medium as

$$c = \sqrt{\left(\frac{\partial p}{\partial \rho}\right)_{s=s_0}} = \text{for perfect gas} = \sqrt{\gamma RT}, \quad (2.1)$$

where R is the gas constant, $\gamma = \frac{C_p}{C_v}$ the specific heats ratio and T the absolute temperature in $^{\circ}K$. The subscript $s = s_0$ indicates isentropic process. For an isentropic transformation the energy equation rewritten in terms of entropy variation leads to the Poisson relation between local pressure and density, namely: $p \propto \rho^\gamma$ that, combined with the definition of sound in equation (2.1), results in a linear relation between small pressure and density fluctuations through the square of sound speed

$$p' = c^2 \rho'. \quad (2.2)$$

The basic fluid dynamics conservation equations of mass and momentum for a compressible fluid read

$$\frac{\partial \rho}{\partial t} + \frac{\partial \rho v_i}{\partial x_i} = 0, \quad (2.3)$$

$$\rho \frac{\partial v_i}{\partial t} + \rho v_j \frac{\partial v_i}{\partial x_j} = -\frac{\partial p}{\partial x_i} + \frac{\partial \sigma_{ij}}{\partial x_j} = -\frac{\partial (p \delta_{ij} - \sigma_{ij})}{\partial x_j}. \quad (2.4)$$

If we consider acoustic propagation as an isentropic perturbation of an equilibrium uniform reference state, described by the variables ρ_0 , p_0 and v_0 , the perturbed field variables can be rewritten as

$$\begin{aligned} \rho' &= \rho - \rho_0, \\ p' &= p - p_0, \\ v' &= v - v_0. \end{aligned}$$

For a quiescent base flow $v_0 = 0 \rightarrow v' = v$ and for small perturbation quantities such that $p' \ll p_0$, $\rho' \ll \rho_0$, the conservation equations can be linearized by neglecting higher order perturbation terms yielding, respectively for mass and momentum are

$$\frac{\partial \rho'}{\partial t} = -\rho_0 \frac{\partial v_i}{\partial x_i}, \quad (2.5)$$

and

$$\rho_0 \frac{\partial v_i}{\partial t} = -\frac{\partial p'}{\partial x_i}. \quad (2.6)$$

The linearized equations can be combined together by elimination of the term $\rho_0 \frac{\partial v_i}{\partial x_i}$ resulting in

$$\left(\frac{1}{c_0^2} \frac{\partial^2}{\partial t^2} - \nabla^2\right) [(p - p_0) \delta_{ij}] = 0, \quad (2.7)$$

²The harmonic composition of the sound produced by a musical instrument determines the timber and the quality of the instrument.

which is the homogeneous wave equation for the pressure perturbation $p' = p - p_0$ also known as D'Alambert's equation. The general solution of equation (2.7) is

$$p' = F(\mathbf{n} \cdot \mathbf{x} - c_0 t), \quad (2.8)$$

where F is determined by initial and boundary conditions. For harmonic waves with frequency $f = 2\pi\omega$ the solution can be rewritten as

$$p' = A e^{i(\omega t - \mathbf{k} \cdot \mathbf{x})}, \quad (2.9)$$

where A is the amplitude and $\mathbf{k} = \frac{\omega}{c_0} \mathbf{n}$ is the vector wave number in the direction of propagation \mathbf{n} (perpendicular to the wavefronts). The latter formulation clearly reveals the character of the sound wave as temporal local oscillation associated with a convection process. The particle velocity caused by the pressure fluctuation can be found by substitution of equation (2.9) in the linearized momentum equation yielding

$$\mathbf{v}_{\text{ac}} = \mathbf{n} \frac{p'}{\rho_0 c_0}. \quad (2.10)$$

The quantity $\rho_0 c_0$ is called the *acoustic impedance (for plane waves)*. It can be compared to the impedance of an electronic circuit, in conformance with a frequently used electronic similarity, in which the pressure is represented by a voltage and the resulting particle velocity by an electric current.

For spherical wave propagation the acoustic impedance is given by

$$\mathbf{v}_{\text{ac}} = \mathbf{n} \frac{p'}{\rho_0 c_0} \left(1 + \frac{1}{i k r} \right), \quad (2.11)$$

which shows that acoustic impedance has a direct dependence on the sound frequency through the wave number $k = \frac{\omega}{c}$ and the distance from the source r .

Sound absorption is the mechanism by which energy carried by acoustic waves is converted into thermal energy, leading to attenuation of the acoustic wave field. In air the main mechanisms causing significant sound absorption are:

- Viscosity
- Heat conductivity
- Molecular thermodynamic relaxation

Due to the above mechanisms sound propagation has a dispersive nature. The energy dissipation generally increases with the frequency of the propagating sound [8]. Heat conductivity and molecular relaxation become significant only for propagation distances of the order of a few hundred wavelengths. Viscous effects are also usually neglected in a sound field because pressure induces a far greater stress field than viscosity at the frequencies of most practical interest. The ratio between the viscous term $\left(\frac{\partial^2 \tau_{ij}}{\partial x_i \partial x_j} \right)$ and pressure fluctuation $\left(\frac{1}{c_0^2} \frac{\partial^2 p'}{\partial t^2} \right)$ for plane waves scales as $\left(\frac{\nu}{\rho_0 c_0} \right)$ which for air at standard conditions is of the order of 10^{-8} .

Applying the *curl* operator to the linearized momentum equation (2.6) one obtains

$$\frac{\partial}{\partial t} (\nabla \times v) = 0, \quad (2.12)$$

which analytically shows that sound does not introduce any rotation of fluid elements. The reason for this is because the forces arising from the pressure gradient are conservative and act through the mass center of the fluid particles. The acoustic velocity v can then be rewritten as gradient of a potential

$$v_i = \frac{\partial \varphi}{\partial x_i},$$

and the pressure, for an initially quiet flow, becomes

$$p' = -\rho \frac{\partial \varphi}{\partial t}. \quad (2.13)$$

The last equation reveals that unlike steady aerodynamics, where the pressure is related to velocity through the non-linear Bernoulli term ρv^2 , in linear acoustics the pressure fluctuations are exclusively related to time variations of the velocity potential. Steady flows have “no voice” [26]. Sharp geometrical changes, rapid variation in boundary conditions, flow properties or structural properties can excite an acoustical radiation ([49] [12]). The radiated sound field has been shown to be typically linear, however the flows that generate it are usually nonlinear, unsteady and turbulent. In general the more unsteady the turbulence is, the higher is the acoustic radiation. The bridge between acoustic linear propagation and chaotic turbulent flows is formally provided by the aeroacoustic analogies.

2.2 Aeroacoustic analogies

Aeroacoustic analogies are reformulations of the basic conservation equations which explicitly relate wave-like propagating disturbances to hydrodynamic flow phenomena. The word analogy, first introduced by Lighthill in [32], stems from replacing the actual unsteady turbulent flow field with an *analogous* linear compressible irrotational acoustic field subject to an external stress tensor. A wave propagation operator is isolated and usually placed at the left hand side of an equation while all the forcing terms of multiple nature that feed the acoustic propagation, e.g. non linear convective terms, flow inhomogeneities, viscous effects, constitute the right hand side of the analogy equation in the form

$$\left(\frac{1}{c_0^2} \frac{\partial^2}{\partial t^2} - \nabla^2 \right) [c_0^2 (\rho - \rho_0) \delta_{ij}] = \bar{A}, \quad (2.14)$$

in which \bar{A} represents a spatially and temporally distributed forcing term enclosing all the hydrodynamic phenomena. The pressure has been replaced by density making use of equation (2.2). The resulting equations are still valid and respect the basic conservation laws from which have been derived.

The crucial issues connected to this formulation are the characterization of the source term and the hypotheses needed to solve the equations. In the course of the 50 years that have passed since the original analogy proposed by Lighthill several other “analogies” have been developed in order to best define both the acoustic domain and the source term in the way that most suited the specific problem under consideration. The use of one propagating field variable with respect to another is quite arbitrary, as long as this represents a local temporal oscillation with respect to a steady (or uniformly moving) reference medium. The source terms are also modified by the choice of the field variable. Pressure fluctuation p' is commonly used while

dealing with heated flow since the formulation directly shows the presence of a monopolar term arising from unsteady heating [25]. Howe [27] in extending Powell's "Theory of vortex sound" [40], considered the fluctuation of the total enthalpy $B' = B - B_0 = \frac{p}{\rho} + \frac{1}{2}v^2 - \frac{p_0}{\rho_0}$ as propagating variable. The resulting source terms, for non heated flows and using specific Taylored Green's functions accounting for solid boundaries, are constituted by purely kinematic quantities (see Appendix C). An alternative formulation based on conservation of the flow invariants has been proposed by Möhring. The latter is again based on only kinematic quantities, which are more accurately evaluated in experimental approaches, and increases the robustness of Howe's formulation as demonstrated by Schram [45]. Solutions of the resulting inhomogeneous wave equations are usually found by means of a 2D or 3D Green's function for the wave operator in either time or frequency domain. A clear description of the procedure is presented by Hirshberg and Schram in [25].

The following sections give a brief description of the analogies which have been used the present work. Starting from Lighthill's basic formulation in sequence Curle's and Ffowcs Williams analogies are derived, with particular attention to their similarities and peculiarities.

2.3 Lighthill's analogy

Sir James Lighthill asserted that the sound generated by the turbulence in the real fluid is exactly equivalent to that produced in an ideal, stationary acoustic medium forced by a stress distribution represented by the tensor T_{ij} , later called the *Lighthill's stress tensor*.

Multiplying the continuity equation by v_i and adding it to the momentum equation (2.4), the following *Reynolds form* of the momentum equation is obtained

$$\frac{\partial \rho v_i}{\partial t} = -\frac{\Pi_{ij}}{\partial x_j}, \quad (2.15)$$

where Π , called the *momentum flux tensor* reads

$$\Pi_{ij} = \rho v_i v_j + (p - p_0)\delta_{ij} - \sigma_{ij}, \quad (2.16)$$

the constant p_0 is inserted for convenience. Lighthill's stress tensor is given by the difference between the actual momentum flux tensor and the corresponding tensor in an linear acoustic medium:

$$T_{ij} = \Pi_{ij} - \Pi_{ij}^0 = \rho v_i v_j + ((p - p_0) - c_0^2(\rho - \rho_0))\delta_{ij} - \sigma_{ij}. \quad (2.17)$$

Π_{ij}^0 indicates the the momentum flux tensor in a linear acoustic medium where the linear relation between pressure and density fluctuation for an isentropic acoustic disturbance of equation (2.2) holds. Lighthill's tensor incorporates not only the generation of sound, but its convection with the flow, its propagation with variable speed and gradual dissipation by conduction and viscosity.

Equation (2.15) can be rearranged in the following way:

$$\frac{\partial(\rho v_i)}{\partial t} + \frac{\partial[c_0^2(\rho - \rho_0)]}{\partial x_i} = \frac{\partial T_{ij}}{\partial x_j}. \quad (2.18)$$

Eliminating the term ρv_i as previously done for equation (2.7) finally *Lighthill's equation* is obtained

$$\left(\frac{1}{c_0^2} \frac{\partial^2}{\partial t^2} - \nabla^2\right)[c_0^2(\rho - \rho_0)] = \frac{\partial^2 T_{ij}}{\partial x_i \partial x_j}. \quad (2.19)$$

Lighthill's equation is exact since it is a rearrangement of the basic conservation equations. In this form, anyway, the analogy does not present a closed analytical solution, unless simplifying assumptions are made, because the sound production mechanism and the propagation (namely the right and left hand side of the equation) are still coupled. Lighthill in his paper [32] proposed some fundamental assumptions about the main flow and the propagation medium, claiming that the sound generation by the mixing fluid is the dominant mechanism, especially at the high Reynolds numbers of interest in aeronautics. At high Reynolds numbers viscous effects are much smaller than inertial effects and provided that any difference in temperature is merely due to kinetic heating or cooling (no heated jets or thermal sources) the non-isentropic effects, at relatively low Mach numbers, can also be neglected. If the acoustic radiation is assumed to take place in a uniform atmosphere at rest the only velocity component of $\rho v_i v_j$ is the acoustic velocity and, except for very large-scale propagations, viscous effects and entropy non-homogeneities have no influence. Therefore, the stress system of equation (2.17) cancels out and the pressure propagation outside the flow region is governed by the homogeneous acoustic wave equation (2.7).

Another basic assumption made by Lighthill for the solution of the analogy is that the produced sound has negligible magnitude compared to the flow fluctuations and no back-reactions of the acoustic waves on the dynamics of main flow is foreseen. This excludes from the analysis flow fields in resonating system such as wind instruments or cavity flows.

Again the condition of low Mach ensures that the flow acts as nearly incompressible; the relative density variations for isentropic flows scale as $\frac{\Delta p}{c_0^2}$. Assuming a dependence of the pressure with the square of the velocity, density variations due to the elasticity of the medium are proportional to M^2 and can be thus neglected in the bulk of the fluid compared to hydrodynamic pressure variations. Lighthill stress tensor can thus be approximated by:

$$T_{ij} \simeq \rho v_i v_j \simeq \rho_0 v_i v_j = T_{ij}^{inc}, \quad (2.20)$$

where T_{ij}^{inc} indicates an incompressible Lighthill tensor. The speed of sound in air at standard conditions is $c \approx 343 \text{ m/s}$ while the effective particle oscillation velocity, even for a quite loud sound propagating as a plane wave, is of the order of 10^{-4} m/s . This order of magnitude estimation explains the difficulty of detecting the displacement due to compressibility effects while analyzing a fluid flow. Incompressible CFD simulations are usually performed for aeroacoustic source description. This strongly reduces the computational costs (see Appendix A) and is relatively valid for low Mach numbers but can introduce considerable errors in case of confined flows over extended geometries as clearly reported by Schram and Hirshberg in [46, 47].

Once the mentioned hypothesis are made, sound radiation can be evaluated from the knowledge of the hydrodynamic source terms, by means of standard integration techniques.

Integration by means of Green's functions

The inhomogeneous wave equation (2.19) is usually integrated by means of a 3-dimensional or 2-dimensional Green's functions in either the time or frequency domain, a detailed derivation is made by Hirshberg and Schram in [25]. The standard free-space 3D Green's function in the time-domain reads

$$G(\mathbf{x}, \mathbf{y}, t, \tau) = \frac{\delta\left(t - \tau - \frac{r}{c}\right)}{4\pi r}, \quad (2.21)$$

in which $r = |\mathbf{x} - \mathbf{y}|$ is the modulus of the distance between the source and the listener, c is the propagation velocity, in this case the speed of sound.

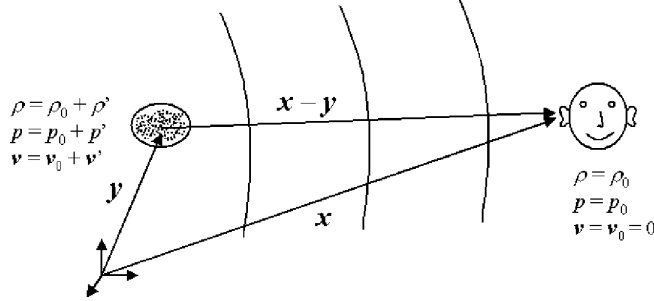


Figure 2.1: Source-listener locations in Lighthill's analogy [Hirshberg and Schram, 2002]

The function G is the solution of the equation:

$$\left(\frac{\partial^2}{\partial t^2} - c^2 \nabla^2 \right) G = \delta(\mathbf{x} - \mathbf{y}) \delta(t - \tau). \quad (2.22)$$

A fundamental property of the 3-D Green's function for subsonic flows, is that each elementary source, positioned at \mathbf{y} and time τ , is non-zero at the listener position \mathbf{x} at time t , at only one specific instant indicated by the argument of the delta function. When the source moves supersonically along a curved path more than one single source point can eventually reach the listener at the same time t ; this leads to the occurrence of “super bangs” for aircrafts. Every source contribution has to be evaluated at the proper *Retarded Time* t_r that is function of r , as it will be specified later.

A new time integration method has been proposed by Casalino in [10]. It is based on an *Advanced Time Integration* which allows the parallel computation of the fluid field and the acoustic propagation in numerical approaches.

The general solution proposed by Lighthill for “unbounded flows” is given by a spatial distribution of impulse sources of strength T_{ij} that results in

$$\rho - \rho_0 = \frac{1}{4\pi c_0^2} \frac{\partial^2}{\partial x_i \partial x_j} \int_{V_y} T_{ij} \left(\mathbf{y}, t - \frac{r}{c_0} \right) \frac{dV}{r}. \quad (2.23)$$

The integral is taken over all space but it only gives effective contribution to the radiation in the region where sources are present. It is therefore common practise to confine the integration region to a finite flow source region V_y . However, the truncation of the source region can pose problems for the numerical implementation of the analogies [35].

With the approximations introduced by Lighthill the integral equation (2.23) reduces to

$$p'(\mathbf{x}, t) = \frac{1}{4\pi} \frac{\partial^2}{\partial x_i \partial x_j} \int_{V_y} \rho_0 v_i v_j \left(\mathbf{y}, t - \frac{r}{c_0} \right) \frac{dV}{r}. \quad (2.24)$$

Far-field approximation

Measurements or evaluations of the sound radiation are usually made at location far away from the source region, in the so called *acoustic far-field* for which $|\mathbf{x}| \gg |\mathbf{y}|$. Then the

distance $r = |\mathbf{x} - \mathbf{y}|$ between the listener and the source, using a Taylor expansion to the first order ³, reduces to just $|\mathbf{x}|$ meaning that the relative distance between source points and source-reference frame origin are negligible compared to the listener-origin distance.

When the listener is located in the acoustic far-field the curvature of propagated spherical waves reduces consistently and the planar wave simplification can be made. This allows the replacement of the spatial derivatives in equation (2.23) with time derivatives, which are often more easily estimated in certain approaches (this is however not always the case dealing with experimental measurements as it will be discussed in section 5). The equivalence can be easily proven by the following transformation

$$\begin{aligned} \frac{\partial}{\partial x_j} f_j \left(\mathbf{y}, t - \frac{|\mathbf{x} - \mathbf{y}|}{c_0} \right) &\approx \frac{\partial}{\partial t} f_j \left(\mathbf{y}, t - \frac{|\mathbf{x}|}{c_0} \right) \frac{\partial}{\partial x_j} \left(t - \frac{|\mathbf{x}|}{c_0} \right) \\ &= -\frac{x_j}{c_0 |\mathbf{x}|} \frac{\partial}{\partial t} f_j \left(\mathbf{y}, t - \frac{|\mathbf{x}|}{c_0} \right) \end{aligned} \quad \text{for } |\mathbf{x}| \rightarrow \infty. \quad (2.25)$$

Lighthill's solution making use of the previous relation can be reformulated as

$$p'(\mathbf{x}, t) = \frac{x_i x_j}{4\pi c_0^2 |\mathbf{x}|^2} \frac{\partial^2}{\partial t^2} \int \rho_0 v_i v_j \left(\mathbf{y}, t - \frac{r}{c_0} \right) \frac{dy^2}{r}. \quad (2.26)$$

Solutions of the above equation are usually found numerically using several discretization methods. The implementation is, however, far from trivial especially concerning the extension of the source region and the accuracy of the discrete method since the quantities to be estimated are usually of the same order of magnitude of the numerical noise introduced by the resolution method, in particular for non-smooth flow data.

Eighth power law

An immediate useful estimation of the intensity of the radiated field has been proposed by Lighthill, in terms of typical velocities and lengths in the flow. Since aerodynamic sound is generated by flow instabilities which are directly related to the flow properties U, ρ, μ, L, c one can expect the emitted sound to be related to the same properties. The amplitude of the stress tensor T_{ij} is evidently proportional to the square of a characteristic velocity in the flow U^2 while the amplitude of the radiated field due to T_{ij} is proportional to its strength multiplied by the square of its frequency $\frac{U}{L}$ (Stokes' effect), analytically indicated by the double time derivative.

From equation (2.26) it follows that a jet radiates into the far field with an efficiency that varies with the fourth power of the velocity

$$\begin{aligned} p'(\mathbf{x}, t) &\sim \frac{U^2}{L^2} \frac{1}{c_0^2 |\mathbf{x}|} \rho_0 U^2 L^3 \\ &= \rho_0 c_0^2 M^4 \frac{L}{|\mathbf{x}|}. \end{aligned} \quad (2.27)$$

³For extended source regions, phase differences can be accounted for by retaining the second term of the series expansion $\frac{\mathbf{x} \cdot \mathbf{y}}{c_0 |\mathbf{x}|}$ resulting in the so called Fraunhofer approximation.

The total acoustic power P radiated for example by a round jet of diameter D can be estimated to scale as

$$\begin{aligned} P &\sim |\mathbf{x}|^2 \frac{p'^2}{\rho_0 c_0} \\ &\sim \rho_0 D^2 c_0^3 M^8, \end{aligned} \quad (2.28)$$

which is the famous “eight power law” found by Lighthill for the intensity of the sound radiation by unbounded turbulence. It is found to give intensity estimations comparable with experimental data for several jet configurations and a wide range of Mach numbers including compressible and supersonic regimes.

2.4 Curle’s analogy

Lighthill’s analogy applies to configurations in which there are no solid boundaries or in which the effect of the solid boundaries can be neglected. Lighthill himself, however, firmly remarked that solid bodies can play an important role in sound generation mechanisms. N. Curle in 1955 [14] extended Lighthill’s theory taking into account the effects of such solid boundaries. Curle’s aeroacoustic analogy is nowadays widely employed in aviation and automotive industry. The influence of solid boundaries immersed in an unsteady flow on the radiated sound field is twofold:

- Sound waves are reflected and diffracted at the surfaces of the bodies.
- A dipolar source distribution is generated at the solid boundaries.

When flow instabilities lie close to a solid surface, pressure recovery by fluid acceleration is prevented by the presence of the boundary. Pressure fluctuation at the surface are in turn transmitted back to the fluid and partially propagate as sound. The pressure variation at the solid surface can be imagined as a distributed time-varying force. A fluctuating force can be directly related to an acoustic source of dipolar nature. Even if the *direct* flow emission is neglected, for low Mach numbers flows [32, 23], there is an energy transfer from the vorticity in the proximity of the body, into pressure fluctuations at the surface which cause an higher intensity emission level with respect to free turbulence.

Starting from the basic conservation equation of mass and momentum, in the absence of external forces, the derivation of Curle’s equation begins similarly to that of Lighthill’s until integration over the source domain is performed. The differential form of the analogy proposed by Lighthill reads

$$\frac{\partial^2 \rho'}{\partial t^2} - c_0^2 \frac{\partial^2 \rho'}{\partial x_i^2} = \frac{\partial^2 T_{ij}}{\partial x_i \partial x_j}. \quad (2.29)$$

Integration by means of a three-dimensional free space 3-D Green’s function $G(\mathbf{x}, \mathbf{y}, t, \tau)$ in presence of solid boundaries leads to the a general solution

$$p'(\mathbf{x}, t) = \int_{-\infty}^{t^+} \int_{V_y} \frac{\partial^2 T_{ij}}{\partial y_i \partial y_j} G(\mathbf{x}, \mathbf{y}, t, \tau) dV d\tau - c_0^2 \int_{-\infty}^{t^+} \int_{\partial V_y} \left[\rho' \frac{\partial G}{\partial y_i} - G \frac{\partial \rho'}{\partial y_i} \right] n_i dS d\tau. \quad (2.30)$$

The surface integral, in Curle's analogy, coincides with the surface of the bodies immersed in the fluid ∂V_y . The volume integral embeds the source region subtracted by the solid bodies. At the listener position also Curle's analogy, as well as Lighthill's analogy, supposes a uniform stagnant fluid in which the linear relation between pressure and density fluctuations in equation (2.2) holds. The volume integral can be integrated by parts in such a way that the partial derivatives are shifted from the Lighthill's stress tensor T_{ij} to the Green's function. Further using the symmetry property of the Green's function $\frac{\partial G}{\partial y} = -\frac{\partial G}{\partial x}$ the derivatives can be brought out of the integral operator yielding

$$p'(\mathbf{x}, t) = c_0^2 \rho'(\mathbf{x}, t) = \int_{-\infty}^{t^+} \int_{V_y} \frac{\partial^2 G}{\partial y_i \partial y_j} T_{ij} dV d\tau + \int_{-\infty}^{t^+} \int_{\partial V_y} \left(\frac{\partial T_{ij}}{\partial y_j} G - T_{ij} \frac{\partial G}{\partial y_j} \right) n_i dS d\tau - c_0^2 \int_{-\infty}^{t^+} \int_{\partial V_y} \left[\rho' \frac{\partial G}{\partial y_i} - G \frac{\partial \rho'}{\partial y_i} \right] n_i dS d\tau. \quad (2.31)$$

The time integration can be eliminated because of causality and replaced by a specific retarded time t_e for the integrand. The derivative $\frac{\partial T_{ij}}{\partial y_j}$ can be evaluated using the momentum equation

$$\frac{\partial T_{ij}}{\partial y_j} = \frac{\partial}{\partial y_j} (\rho v_i v_j + (p' - c_0^2 \rho')) \delta_{ij} - \sigma_{ij} = -\frac{\partial \rho v_i}{\partial \tau} - c_0^2 \frac{\partial \rho'}{\partial y_j}. \quad (2.32)$$

Substitution of equation 2.32 in 2.31 yields

$$\begin{aligned} \rho'(\mathbf{x}, t) &= \int_{-\infty}^{t^+} \int_{V_y} \frac{\partial^2 T_{ij}}{\partial y_i \partial y_j} G dV d\tau \\ &+ \int_{-\infty}^{t^+} \int_{\partial V_y} \left[\left(-\frac{\partial \rho v_i}{\partial \tau} - c_0^2 \frac{\partial \rho'}{\partial y_i} \right) G - (\rho v_i v_j + (p' - c_0^2 \rho')) \delta_{ij} - \sigma_{ij} \right] \frac{\partial G}{\partial y_j} n_i dS d\tau \\ &- c_0^2 \int_{-\infty}^{t^+} \int_{\partial V_y} \left(\rho' \frac{\partial G}{\partial y_i} - G \frac{\partial \rho'}{\partial y_i} \right) n_i dS d\tau. \end{aligned} \quad (2.33)$$

For high-Reynolds number flows the convective transport dominates over the molecular transport and viscous effects can be neglected in the bulk of the fluid. In the source region, for low Mach numbers, also compressibility effects, due to the elasticity of the medium, can be disregarded. Near the walls, on the other hand, viscous tangential stresses and entropy variations play an important role. However, in real configurations, these phenomena are usually overwhelmed by the normal stresses and generally neglected.

Exploiting the symmetry properties of the free-space 3D Green's function: $\frac{\partial G}{\partial y} = -\frac{\partial G}{\partial x}$ and $\frac{\partial G}{\partial t} = -\frac{\partial G}{\partial \tau}$, together with the mass conservation relation, for low Mach number open flows, equation 2.33 reduces to:

$$\begin{aligned} p'(\mathbf{x}, t) &= \frac{1}{4\pi} \frac{\partial^2}{\partial x_i \partial x_j} \int_{V_y} \frac{\rho_0 v_i v_j}{r} \Big|_{t=t_e} dV + \\ &- \frac{1}{4\pi} \frac{\partial}{\partial t} \int_{\partial V_y} \frac{\rho v_i}{r} \Big|_{t=t_e} n_i dS + \\ &+ \frac{1}{4\pi} \frac{\partial}{\partial x_j} \int_{\partial V_y} \frac{p' \delta_{ij} + \rho v_i v_j}{r} \Big|_{t=t_e} n_i dS. \end{aligned} \quad (2.34)$$

Derivation of equation (2.34) from equation (2.33) presupposes that the fluid model does account for compressibility effects. This is usually not the case in numerical simulations where, in order to reduce the computational costs, incompressible flow simulations are preferred. On the other hand, experimental PIV flow data are, in general, not accurate enough to resolve the flow features related to density variations, especially at low Mach numbers. Neglecting compressibility using Curle's approach, however, has minor influence on the acoustic prediction as long as the body can be considered compact, i.e. as long as the body dimensions are comparable to the wavelength of the generated sound. For non-compact bodies, on the other hand, neglecting these contributions can introduce strong deviations from the expected values, as demonstrated by Hirshberg and Schram in [46, 13].

The surface integral can be eliminated by the choice of specific Green's functions which already incorporate the geometry of the scattering body (see the use of Taylored Green's functions in [23]). These functions can be calculated by Conformal Mapping techniques as shown by Howe in [27] (see Appendix C).

If the integration surface coincides with the physical body surface as in the original Curle's derivation [14, 25], and if the bodies are fixed or vibrating in their own plane, the normal velocity at the wall is zero and the velocity components at the surface drop out, leading to a simpler formulation

$$\begin{aligned}
 p'(\mathbf{x}, t) &= \frac{x_i x_j}{4\pi c_0^2 |\mathbf{x}|^2} \frac{\partial^2}{\partial t^2} \int_{V_y} \frac{\rho_0 v_i v_j}{r} \Big|_{t=t_e} dV + \\
 &- \frac{x_j}{4\pi c_0 |\mathbf{x}|} \frac{\partial}{\partial t} \int_{\partial V_y} \frac{P_{ij}}{r} \Big|_{t=t_e} n_i dS,
 \end{aligned} \tag{2.35}$$

where space derivatives have been replaced by time derivatives with the far-field assumption and the tensor $P_{ij} = p' \delta_{ij} - \sigma_{ij}$ is a generalized pressure tensor including, for completeness, also viscous effects. Equation (2.35) is the standard formulation of Curle's equation.

The acoustic pressure at the listener position is generated by two sources

Quadrupolar term Representing the *direct* contribution to the noise of the flow instabilities.

Dipolar term Fluctuating normal and tangential (usually of minor entity) stresses at the wall induced by hydrodynamic fluctuations near the body.

The surface integral, representing the modification to Lighthill's theory, is equivalent to the sound generated in a medium at rest by a distribution of dipoles of strength P_{ij} per unit area. The effect of hydrodynamic/acoustic refraction and diffraction at the solid boundaries are completely incorporated by the dipole field P_{ij} . The standard Curle's analogy, unlike FW-H analogy, does not account for the movement of the noise generating bodies.

2.4.1 Compact-body assumption and properties of a dipolar source

Simplifying assumptions for aeroacoustic predictions can be made by introducing the concept of compactness of the acoustic sources. If L indicates the characteristic source length (eddy size or immersed body size) and U the free-stream velocity, in the time $\frac{L}{U}$ in which the flow

travels a distance L , an acoustic wave, with characteristic velocity c , travels the distance $d_{ac} = \frac{cL}{U} \propto \lambda$, where λ indicates the acoustic wavelength. In the condition that $L \ll \lambda$ the noise generating source (or source region) is said to be acoustically *compact*. This means that the acoustic propagation escapes the source region very fast compared to the movement of the flow itself. The compactness relation can be rewritten as: $\frac{L}{\lambda} \propto M \ll 1$ which indicates that low-Mach-number flows are more likely to be acoustically compact.

If the dimensions of the body (or eddy) are small compared to the wavelength of the produced sound, i.e. under *Compact-Body* conditions, variation of emission time t_e over the surface can be neglected and the distance r of each point source from the listener replaced by a unique scalar distance $|\mathbf{x}|$. The body is then considered as a pointwise ‘compact’ emitter and equation 2.35 further reduces to

$$p'(\mathbf{x}, t) = \frac{x_i x_j}{4\pi c_0^2 |\mathbf{x}|^3} \frac{\partial^2}{\partial x_i \partial x_j} \int_{V_y} \rho_0 v_i v_j \Big|_{t=t_e} dV - \frac{x_j}{4\pi c_0 |\mathbf{x}|^2} \frac{\partial}{\partial t} \int_{\partial V_y} P_{ij} \Big|_{t=t_e} n_i dS. \quad (2.36)$$

An order of magnitude estimation of the surface integral, similarly to what has been done for Lighthill's volume source, would suggest

$$p'(\mathbf{x}, t) \sim \frac{U}{L} \frac{1}{c_0^2 |\mathbf{x}|} \rho_0 U^2 L^3 = \rho_0 M^3 \frac{L c_0}{|\mathbf{x}|}, \quad (2.37)$$

which reveals that the acoustic power radiated by this term scales with M^6 . For low Mach number flows, it is 2 orders of magnitude more efficient than the Lighthill's volumetric source term. Therefore the latter term is commonly neglected in the source computation, significantly reducing the computational costs.

In compact body conditions, the pressure integral at the actual surface can be interpreted as the total force exerted by the fluid on the body. Curle's equation can be rewritten in the simple and extremely useful form

$$p'(\mathbf{x}, t) = -\frac{x_j}{4\pi c_0 |\mathbf{x}|^2} \frac{\partial F_j(t_e)}{\partial t}. \quad (2.38)$$

Equation (2.38) is the analytical expression of the so called *Gutin's principle* for compact rigid bodies, which directly relates the force F_j exerted by the fluid on the body to the radiated field, in a far field approximation. The maximum radiation intensity is clearly aligned with the fluctuating force in agreement with what already observed by Rayleigh. A fixed body, according to the principles of dynamics, reacts to the force exerted by the fluid with an opposite reactive force of the same magnitude. The sound emission can be considered as due to fluctuations of the body in an otherwise steady flow. The equivalence of the active and reactive dipolar forcing term was investigated by Gutin (or Yudin) (1936) and the so called *Gutin's principle* has been lucidly reformulated by Powell in [40] as follows:

‘‘If a relatively small, fixed, rigid body in a moving fluid sustains a certain fluid force, then the resultant sound radiation relatively far from it is the same as that which would result from an equal but opposite force acting directly on another still fluid’’

A force exerted on the fluid corresponds to what is mathematically defined as *dipole*. For a periodic exchange of momentum $\dot{m}\delta$ between two locations in a flow at small distance δ a force $F = \frac{d\dot{m}\delta}{dt}$ needs to be applied on the fluid. The concept of dipole is always associated with a force.

Mathematically the dipolar nature of the surface term is represented by the term $\frac{\partial G}{\partial y_j}$ in equation (2.30). The space derivative of a Green's function can be seen as the response of two close opposite sources: $\frac{g(\vec{x}, y_i + \Delta s n_i)}{\Delta s}$ is the response to a positive source of strength $\frac{1}{\Delta s}$ located at $y_i + \Delta s n_i$, while $\frac{-g(\vec{x}, y_i)}{\Delta s}$ is the response to a negative source of strength $-\frac{1}{\Delta s}$ located at y_i .

$$\frac{\partial g(\vec{x}, \vec{y})}{\partial y_i} = \lim_{\Delta s \rightarrow 0} \frac{g(y_i + \Delta s n_i) - g(y_i)}{\Delta s}. \quad (2.39)$$

This mathematical definition of a dipole source reflects the pulsating nature of the phenomenon.

The far field of a rigid translating compact body is dominated by the “dipole” component of the field. This is physically the mechanism of sound production in the case of loudspeakers, drums or the strings of an Aeolian Harp. The compact Curle's equation in the form

$$p'(\mathbf{x}, t) = \frac{\partial}{\partial x_i} \left(\frac{F_i(t - \frac{r}{c})}{4\pi r} \right), \quad (2.40)$$

can be rewritten in polar coordinates: $x = r \cos \theta$ and $\frac{\partial r}{\partial x_i} = \cos \theta$, with θ indicating the angle with the dipole axis as

$$p'(r, \theta, t) = \frac{\cos \theta}{4\pi} \left[\frac{1}{cr} \frac{\partial F}{\partial t} + \frac{F}{r^2} \right]. \quad (2.41)$$

The term with the inverse square of the distance clearly dominates the field near the source and it is therefore called *Near-Field* component. The term linearly decreasing with the distance dominates at larger distances from the source and is consequently called *Far-field* component.

Multipoles directivity patterns

The direction of highest emission of a dipolar source lies on the line connecting the two coupled sources, called *axis of the dipole* (dotted line in Figure 2.2 (a)), an observer perpendicular to the dipole axis does not perceive any acoustic disturbance because of the mutual cancelation of the sources.

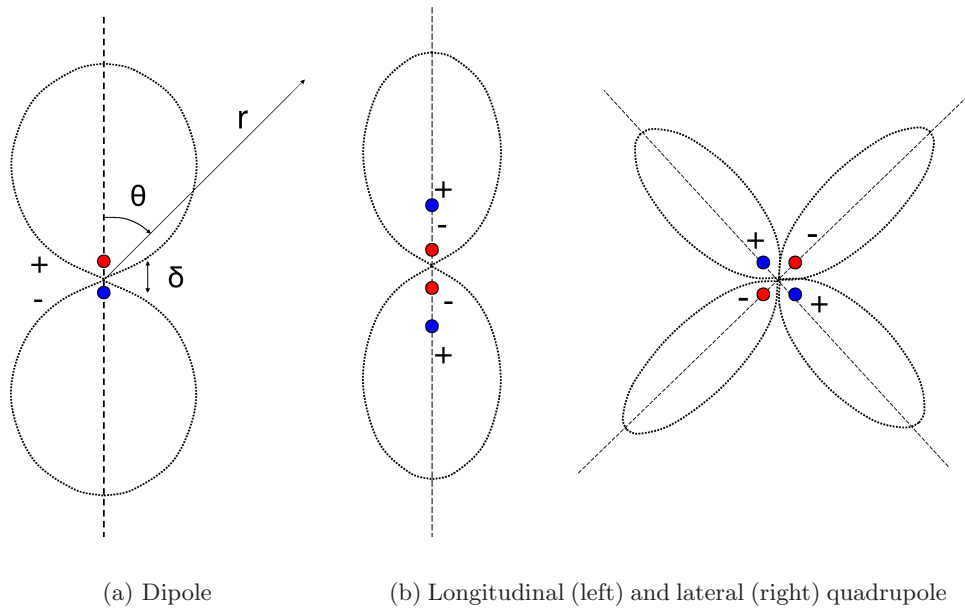


Figure 2.2: Dipolar and quadrupolar radiation pattern

Lighthill's turbulence noise emission has quadrupolar nature. A quadrupole can be seen as the combination of close dipole couples (like the dipole as combination of two monopolar close sources). The double derivative of the source term in Lighthill's equation (2.19) analytically gives rise to nine distinct quadrupoles: three longitudinal quadrupoles, in which the axis of the two dipoles lie in the same line, and six lateral quadrupoles with mutually perpendicular characteristic axes (see Figure 2.2 (b)). Quadrupolar sources also possess near and far-field components.

Monopole sources, for example a pulsating sphere or a localized heat source inside the fluid, do not possess a near field component; the sound decays everywhere as $\frac{1}{r}$ with no preferential directions. The acoustic power radiation of monopoles is the most efficient for low Mach numbers ($\sim M^4$), because there is no reciprocal cancellation of the sources as in the case of dipoles and quadrupoles.

2.5 Ffowcs Williams-Hawkings analogy

The Ffowcs Williams-Hawkings (FW-H) analogy is a further extension of Curle's analogy to include "arbitrary convective motion" of the surfaces [22, 4].

A typical application is the case of helicopter rotor blades in which the aerodynamic sound is produced by multiple combined mechanisms: fluid displacement due to blade thickness, steady and unsteady blade loadings, rotating shocks, blade-vortex interactions, blade-turbulence interaction.

Consider a finite volume of space containing a disturbed flow and rigid bodies in arbitrary motion, both flow and bodies generating sound. At large distances from the volume it is possible to replace both the fluid and the bodies by equivalent acoustic sources in a quiescent

uniform medium at rest. The fundamental idea of Ffowcs Williams and Hawkins is to introduce a system of mathematical *control surfaces* accounting for the presence of moving bodies inside the flow. The inner volume of the surface is assumed to contain the ambient fluid at rest. The discontinuity at the surface leads to the introduction of source terms in the conservation equations of mass and momentum. The derivation of the governing equations is carried out rewriting the conservation laws by making use of generalized variables, valid throughout all space, including the control surfaces. The key assumption is again that no flow-acoustic coupling occurs, i.e. that the acoustic field produced by the flow does not affect the flow in return.

The control surfaces do not necessarily need to coincide with physical surfaces. It has been shown that it is possible to exploit arbitrary “permeable” control surfaces immersed in the flow. This results in a kind of *Black-Box* approach, meaning that one is not directly interested in what is actually happening inside the control surface but rather in the effect that the latter induces at the surface itself. It is the same philosophy behind Kirchhoff formulation for wave equation, widely employed in acoustic reconstructions. Kirchhoff integration surface, however, needs to be placed in the linear propagation region outside the flow [19]. FW-H equation instead, being a pure combination of basic conservation equations, accounts for flow nonlinearities and the placement of the control surface can be almost arbitrary, provided that all the physics of the flow inside the surface are accounted for by the surface integrals.

The implementation of permeable surfaces has been clearly formulated by di Francescantonio in [18] who defined the so called Kirchhoff-Ffowcs Williams-Hawkings equation (KFWH). Later Brentner & Farassat remarked that the use of permeable surfaces was already intrinsically contained in the formulation of Ffowcs Williams and Hawkins. They further highlighted the peculiar differences between Kirchhoff and FW-H methods [9].

The power of the Ffowcs-Williams Howkings (FW-H) analogy is to synthesize the Lighthill’s and Curle’s analogy into a unique elegant formulation valid throughout all space. Howe in his Theory of Vortex Sound [27] does not make any distinction between FW-H and Curle’s analogy. It will be shown in the following that the latter analogy can be considered as a specific case of the former, in the case of solid steady integration surfaces.

If the control surface S is sufficiently smooth it can be described by the function $f(\mathbf{x}, t)$. For all the points \mathbf{x} inside the surface $f < 0$, while for all the points outside the surface $f > 0$. The surface S can move with velocity $\mathbf{u}(\mathbf{x}, t)$. The corresponding Heaviside unit function $H(f)$ is defined as follows:

$$H(f) = \begin{cases} 0 & \text{if } f < 0 \\ 1 & \text{if } f > 0 \end{cases}$$

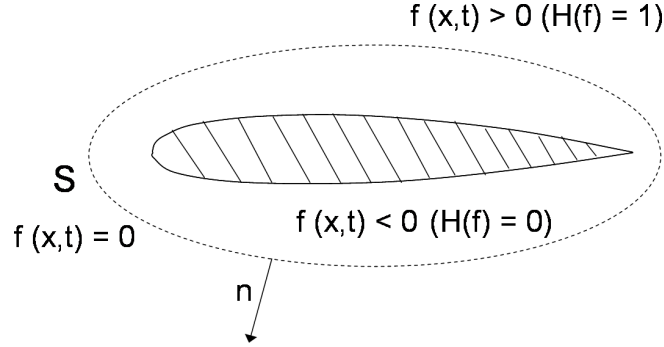


Figure 2.3: Ffowcs Williams -Hawkings integration surface

The outwards normal \mathbf{n} to S is given by

$$\mathbf{n} = \frac{\nabla f}{|\nabla f|} \Big|_{f=0}. \quad (2.42)$$

The space and time derivatives of the Heaviside function can be expressed as

$$\begin{aligned} \frac{\partial H(f)}{\partial t} &= \frac{\partial H(f)}{\partial f} \frac{\partial f}{\partial t} = -u_i \frac{\partial H(f)}{\partial f} \frac{\partial f}{\partial x_i} = -u_i \delta(f) \frac{\partial f}{\partial x_i} \\ \frac{\partial H(f)}{\partial x_i} &= \frac{\partial H(f)}{\partial f} \frac{\partial f}{\partial x_i} = \delta(f) \mathbf{n} |\nabla f|. \end{aligned} \quad (2.43)$$

Multiplying the mass and momentum equations, as given respectively in equations (2.3) and (2.18), by $H(f)$ and rearranging the derivatives by means of the properties 2.5 for the Heaviside function, continuity can be rewritten as

$$\frac{\partial H(f)(\rho - \rho_0)}{\partial t} + \frac{(\rho v_i H(f))}{\partial x_i} = \rho_0 u_i \delta(f) \frac{\partial f}{\partial x_i}, \quad (2.44)$$

and the momentum conservation equation

$$\frac{\partial(\rho v_i H(f))}{\partial t} + \frac{\partial[c_0^2(\rho - \rho_0)]}{\partial x_i} = \frac{\partial(p\delta_{ij} - \sigma_{ij})}{\partial x_j}. \quad (2.45)$$

Following the same procedure used by Lighthill, the last two equation can be combined by elimination of the term $\rho v_i H(f)$ yielding a wave-like propagation equation of the kind

$$\begin{aligned} \frac{\partial^2(\rho' H(f))}{\partial t^2} - c_0^2 \frac{\partial^2(\rho' H(f))}{\partial x_i \partial x_j} &= \frac{\partial^2}{\partial x_i \partial x_j} (T_{ij}) \\ &- \frac{\partial}{\partial x_i} \left((p'\delta_{ij} - \sigma_{ij}) \delta(f) \frac{\partial f}{\partial x_j} \right) \\ &+ \frac{\partial}{\partial t} \left(\rho_0 u_i \delta(f) \frac{\partial f}{\partial x_i} \right), \end{aligned} \quad (2.46)$$

which is the differential form of the Ffowcs Williams-Hawkings equation. This is an exact reformulation of the basic conservation equations of fluid dynamics, valid everywhere inside the control surfaces where H is identically zero and outside the control surfaces where $H = 1$.

In this sense the variables ρ' and T_{ij} represent generalized functions: zero inside the control surfaces and equal to respectively density fluctuations and the Lighthill's stress tensor outside the surfaces [9].

Ffowcs-Williams formulation infers that density fluctuations radiated by a real turbulent fluid and moving objects are exactly the same as those that would be generated by an "analogous" acoustic medium at rest, forced by three source distributions:

1. A **volume** distribution $\frac{\partial^2}{\partial x_i \partial x_j}(T_{ij})$ in the region outside the surfaces, due to Reynolds stresses, non isentropic regions and viscous stresses in the flow, acting like a **quadrupole** source.
2. A **surface** distribution $\frac{\partial}{\partial x_i} \left((p' \delta_{ij} - \sigma_{ij}) \delta(f) \frac{\partial f}{\partial x_j} \right)$ which is zero everywhere except at the boundary of the surfaces $f(\mathbf{x}, t)$, as indicated by the Dirac function, due to the interaction of the flow with moving bodies (the contribution is due to unsteady pressure fluctuations and viscous stresses at the surface) acting like a **dipole** source.
3. A surface distribution $\frac{\partial}{\partial t} \left(\rho_0 u_i \delta(f) \frac{\partial f}{\partial x_i} \right)$ which is again zero everywhere except at the surface boundary, due to the kinematics of the bodies, represented by the rate of volume injection across the surface, acting like a **monopole** source.

If the integration surface coincides with a solid body, the dipolar source represents the sound from a fluctuating surface force and the monopole source the transpiration of flow through the surface or the volume changes of the body.

Also the FW-H equation can not be directly solved unless simplifying approximations are made. Roger (2006) [43] clearly defined the necessary assumptions for general aeronautical applications in order to obtain an approximated wave equation. Some of these approximations can be partially released if the needed information is provided by an accurate flow visualization or CFD simulation. The most common approximations, similarly to the ones mentioned in Section 2.3 for the source terms are:

- Reynolds numbers are sufficiently high that viscous effects can be neglected in the bulk of the fluid and approaching the surface. Mach number is sufficiently low to neglect compressibility effects inside the flow region.
- In many cases of interest in aerodynamics the fluctuating forces arising on solid surfaces because of non-homogeneities in the surrounding flow are much higher than the surface pressure fluctuations of acoustic nature. When evaluation of the source terms is concerned the latter contribution can be neglected compared to the former. Hence diffraction effects are not taken into account. This is relatively a good approximation as long as the wavelength of the sound is large enough with respect to the emitting surface, i.e for small Helmholtz numbers $He = \frac{2\pi L}{\lambda} \ll 1$. The movement of the surface is that of a rigid body, no vibration is accounted for. When the surface coincides with a physical body surface, the second term reduces to loading forces (lift and drag) that can be easily determined by classical steady or unsteady aerodynamics. This is consequently called the loading noise and usually constitutes the most efficient contribution to radiation in many practical cases.

- The third term does not require approximations, since it is completely defined by the kinematics of the surfaces, assumed to be known. It is called thickness noise and is due to fluid displacement caused by the relative motion of the surfaces and the fluid.

The integral solution is usually determined by Green's function techniques yielding

$$\begin{aligned}
c_0^2 \rho'(\mathbf{x}, t) &= \frac{\partial^2}{\partial x_i \partial x_j} \int_{V_y} \frac{T_{ij}}{4\pi r} \Big|_{t=t_e} dV \\
&+ \frac{\partial}{\partial x_i} \int_{\partial V_y} \frac{[\rho v_i (v_j - u_j) + p' \delta_{ij} - \sigma_{ij}]}{4\pi r} \Big|_{t=t_e} n_i dS \\
&- \frac{\partial}{\partial t} \int_{\partial V_y} \frac{\rho_0 u_i + \rho (v_i - u_i)}{4\pi r} \Big|_{t=t_e} dS.
\end{aligned} \tag{2.47}$$

Equation (2.46) can be rewritten in the more compact form proposed by di Francescantonio in [18], highlights the different nature of the volume, the loading and thickness noise terms

$$\begin{aligned}
&\left(\frac{1}{c^2} \frac{\partial^2}{\partial t^2} - \nabla^2 \right) \{(\rho - \rho_0) c^2 H(f)\} = \\
&\frac{\partial^2}{\partial x_i \partial x_j} \{T_{ij} H(f)\} - \frac{\partial}{\partial x_i} \{L_i \delta(f)\} + \frac{\partial}{\partial t} \{Q \delta(f)\}
\end{aligned} \tag{2.48}$$

in which

$$\begin{aligned}
T_{ij} &= \rho v_i v_j + (p' - c_0^2 \rho') - \sigma_{ij}, \\
L &= P_{ij} \hat{n}_j + \rho u_i (u_n - v_n), \\
P_{ij} &= (p - p_0) \delta_{ij} - \tau_{ij} Q = \rho_0 U_i \hat{n}_i.
\end{aligned} \tag{2.49}$$

The term T_{ij} (quadrupole source) is the classical *Lighthill's stress tensor* accounting for nonlinear effects, vorticity, turbulence, entropy non homogeneities among others, the term L is called *Loading noise* (dipole source) and is generated by the force that acts on the fluid as a result of the presence of the body. The term Q is called *Thickness noise* (monopole source) is determined by the geometry and the kinematics of the body.

The control surface for integration of the last equation can be arbitrarily placed inside the flow region. The volumetric term is integrated over the volume external to the control surface. The loading and thickness noise sources are evaluated at the surface. The fluid contained by the surface is replaced by uniform quiescent fluid and the effect of volumetric sources embedded by the surface, in the case that the surface does not coincide with the body surface, are accounted for by the surface terms L and Q .

The previous results can be generalized to moving surfaces (bodies) using a Lagrangian coordinate system attached to each moving surface element. This results in amplitude corrections of the kind $\frac{1}{|1 - \mathbf{M} \cdot \frac{\mathbf{R}}{R}|}$ and frequency corrections determined by a variation in the retarded time known as Doppler effect.

For *steady* surfaces for which $u_i = 0$, equation (2.51), neglecting the viscous effects, reduces

to

$$\begin{aligned}
\rho'(\mathbf{x}, t) &= \frac{\partial^2}{\partial x_i \partial x_j} \int_{V_y} \frac{T_{ij}}{4\pi r} \Big|_{t=t_e} dV \\
&+ \frac{\partial}{\partial x_j} \int_{\partial V_y} \frac{\rho v_i v_j + p' \delta_{ij}}{4\pi r} \Big|_{t=t_e} n_i dS \\
&- \frac{\partial}{\partial t} \int_{\partial V_y} \frac{\rho_0 u_i + \rho v_i}{4\pi r} \Big|_{t=t_e} n_i dS.
\end{aligned} \tag{2.50}$$

Moreover for steady *non permeable* surfaces, e.g. if the integration surface coincides with a steady physical surface, the no cross flow condition implies that $\mathbf{v} \equiv \mathbf{u} = 0$ and the latter equation further reduces to

$$\rho'(\mathbf{x}, t) = \frac{x_i x_j}{|\mathbf{x}|^2} \frac{\partial^2}{\partial t^2} \int_{V_y} \frac{T_{ij}}{4\pi c_0^2 r} \Big|_{t=t_e} dV - \frac{x_j}{|\mathbf{x}|} \frac{\partial}{\partial t} \int_{\partial V_y} \frac{p' \delta_{ij}}{4\pi c_0 r} \Big|_{t=t_e} n_i dS. \tag{2.51}$$

which is the same result of Curle's represented by equation (2.34) for *steady* integration surfaces. It has been shown that FW-H analogy can be seen as a generalized formulation of Curle's equation to arbitrary permeable surfaces. Howe in [27] derives Curle's equation as a special case of Ffowcs Williams-Hawkings formulation for the case of steady non porous surfaces following the generalized variables procedure.

In the present work a unique formalism, combining Curle's and FW-H analogies, for steady surfaces, herein called Curle/FW-H equation, is implemented

$$\begin{aligned}
p'(\mathbf{x}, t) &= \frac{x_i x_j}{4\pi c_0^2 |\mathbf{x}|^2} \frac{\partial^2}{\partial t^2} \int_{V_y} \frac{T_{ij}}{r} \Big|_{t=t_e} dV \\
&- \frac{x_j}{4\pi c_0 |\mathbf{x}|} \frac{\partial}{\partial t} \int_{\partial V_y} \frac{\rho v_i v_j + p' \delta_{ij}}{r} \Big|_{t=t_e} n_i dS \\
&- \frac{1}{4\pi} \frac{\partial}{\partial t} \int_{\partial V_y} \frac{\rho v_i}{r} \Big|_{t=t_e} n_i dS.
\end{aligned} \tag{2.52}$$

As far as the integration surface is moved away from the body the mixed velocity term $\rho v_i v_j$ and the mass flux ρv_i at the surface need to be included. The numerical implementation of the latter equation is presented in Chapter 5.

Chapter 3

Experimental Techniques

This chapter briefly describes the experimental techniques used for the present work. First a short historical background on the importance of experiments in scientific investigation is provided. This is followed by the description of the principles and characteristics of particle image velocimetry (PIV) and the acoustic measurement techniques for quantification and localization of the noise sources.

3.1 Short historical background

The most immediate way to investigate a physical phenomenon is the direct close observation of the phenomenon itself. The technique of reproducing a real event in a controlled way in order to understand its intrinsic mechanisms is known as an “experiment”. Most people frequently make small experiments when, for example, we want to know if the clothes hanging on a rope will fall or not because of mass unbalance in a certain position. The results of each even small experiment, if stored and assimilated, increases the knowledge of the person who made it and the ones to whom it has been communicated. In larger scale, buildings, cars and aeroplanes are constructed following fixed criteria for maximum loads or fatigue cycles which have been experimentally recognized to be safe and do not need to be checked again.

Experiments (from latin ex-periri = “to try out”) are the foundations of the *scientific method* introduced by Galileo Galilei (1564-1642) who first marked the difference between science and philosophy. The scientific method follows some well-defined steps:

1. Casting informations
2. Observation of the phenomenon
3. Choice of the physical quantities
4. Formulation of the hypothesis
5. Elaboration of a theory able to explain the phenomenon in a wider sense
6. **Validation (or invalidation) of the theory by means of experiments**

The failure of even one experiment is sufficient to invalidate the entire theory.

The philosophical theory called “Empirism” born in the 17th century in England promulgated by J. Locke, G. Berkeley and D. Hume proclaimed the sensorial experience as the only way to acquire actual knowledge and stressed the importance of scientific method. Ronald Fisher 1890-1962 in his work *Design of an experiment* (1935) systematically described the way to plan a modern experiment. Until the last few centuries, however, the experimental field was restricted to qualitative statements, even less in the field of aerodynamics. Leonardo da Vinci in the 15th century was already able to make very detailed drawings of the nature of the structures within a water flow simply by observation. In the first half of the 18th century B. Robins projected a whirling arm for aerodynamic drag measurements. This was the big step from the passive observation of a flow by controlled reproductions of it which further evolved in 1871 in the realization of the first enclosed wind tunnel designed by F. H. Wenham. Controlled aerodynamic visualizations allowed the development of the wing for the first flight of the Wright’s brothers (1904) and the development of Prandtl’s theories began at that time. Wind tunnel studies, however, were confined to qualitative results until the last few decades when the implementation of computers and high technological tools started providing quantitative flow descriptions.

Experimental tests have been widely employed in the aeronautic field in the last decades. These allowed for the validation of several theories and the characterization of phenomena which could not be analytically predicted, such as turbulent transition or instability phenomena. Experimentally derived empirical laws are still often employed mainly dealing with boundary layers or turbulent flows [54]. The reliability of the experimental results strongly depends on the accuracy of the measured quantities. Continuous technological progress allows for increasingly detailed descriptions of the characteristic flow variables in both space and time(-frequency) domain with resolution levels close to numerical models. Notwithstanding the wide use of CFD, experiments nowadays still play a central role in aerodynamic investigations also for validation and development of numerical simulations. The main power of the experimental methods resides in the direct observation of the physical phenomenon and in the immediateness and readability of the results.

The experimental techniques used for the present study are Particle Image Velocimetry for the aerodynamic field evaluation and far-field microphone measurements together with Array Beam Forming technique for the acoustic source detection and quantification. A brief description of the mentioned techniques is given in the following sections.

3.2 Particle Image Velocimetry

Particle Image Velocimetry (PIV) is a non intrusive technique, developed in the 1980’s, which allows for detection of the velocity field in relatively short times. A complete review of PIV technique with related practical applications has been recently published by Raffel *et al.* in collaboration with many other PIV experts [41].

PIV is a powerful tool in extracting velocity information from both gaseous and liquid media over large part of the flow field; other techniques as Laser Doppler Velocimetry are restricted to a single measurement point.

A schematic of a typical modern PIV apparatus for wind tunnel tests is presented in Figure 3.1.

where R is the particle radius, a the (gravitational) acceleration, μ the dynamic viscosity and ρ_p and ρ_f the density of respectively the tracer particles and the flow. A detailed description of the frequency response for different seeding particles under different flow conditions was given by Melling in 1997. Big and heavy particles are not suitable for a proper flow detection. However, the light scattering properties of the particle depend on the particle radius, e.g. small particles scatter less; therefore a trade-off has to be made for the choice of the right particle dimension.

The commonly employed tracer particles for flow visualization experiments are listed in Table 3.1.

Table 3.1: Common seeding materials in air

Material	Specific gravity	Refractive index
Smoke	1	1.3
Silicon dioxide	2.19	1.45
Olive oil	0.97	1.3
Polystyrene latex spheres	1.05	1.59

The importance of a proper seeding is often stressed by PIV people; this is sometimes difficult to achieve, especially for high speed flows and discontinuous body geometries.

3.2.2 Illumination

The contrast of the PIV recordings is directly proportional to the scattered light power. Light is not blocked by small particles but spreads in all directions. Mie's theory describes the scattering directivity of spherical particles with diameter D_p larger than the wavelength of the incident light λ . The light scattered by small particles is a function of many factors: the ratio of the refractive index of the particles and the surrounding fluid, the size of the particles, their shape and orientation, light polarization and observation angle. Light scattering patterns, according to Mie's theory, are shown in Figure 3.2.2 for decreasing wavelengths.

The illumination is often provided by lasers because of their monochromatic light emission at high energy density with no chromatic aberrations. The most common semiconductor laser types with relative characteristics are indicated in Table 3.2. The laser material may consist of atomic or molecular gas, semiconductor or solid material. The material is brought to higher energy level by either electromagnetic or chemical excitation. According to quantum mechanics when the material comes back to its equilibrium state it "spontaneously" emits energy in the form of randomly directed photons, i.e. light. The light is collected inside a resonator and converged into a beam. Solid based lasers Nd:YAG and Nd:YLF are the most frequently used. Nd^{3+} ions are incorporated in a hosting crystal of yttrium-aluminium-garnet for the Nd:YAG laser and yttrium lithium fluoride for the Nd:YLF.

When excitation of the semiconductor is obtained by diode pumping the laser can be operated at high average power at frequencies up to over 10 kHz. Nd:YLF diode pumped laser type is particularly suited for high-speed applications and was also used for the present experiment. The fundamental wavelength $\lambda = 1053 \text{ nm}$ is turned into visible green light $\lambda = 526 \text{ nm}$ by crystal frequency doublers. The laser beam is transformed by optical lenses into a thin laser sheet (for 2D-PIV) passing through the observation region.

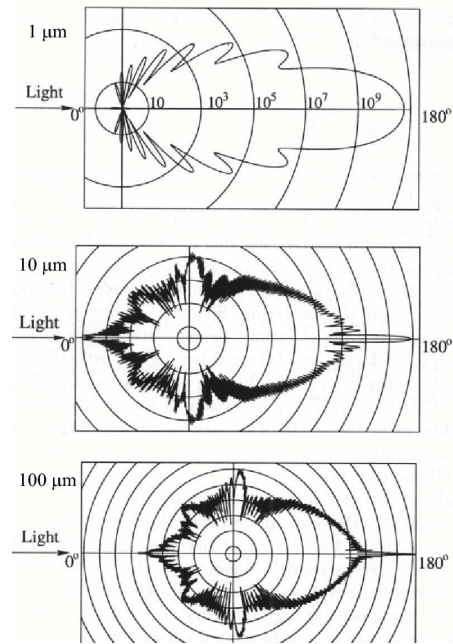
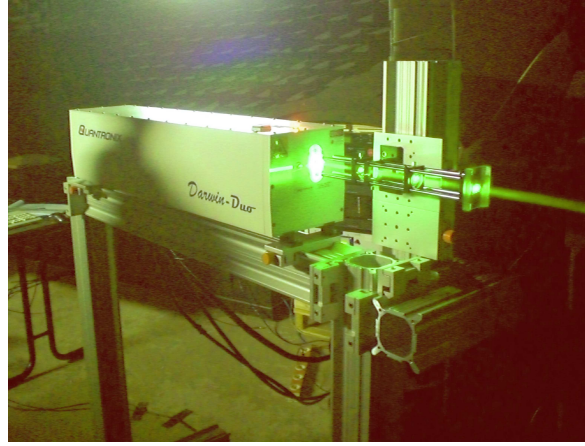


Figure 3.2: Scattering directivity for different λ [Raffel *et al.*, 1998]

Table 3.2: Common Laser Types

Laser	wavelength λ [nm]	pumping system	properties
Neodym-YAG	532 (1064)	flash lamp (diode)	Low threshold, good mechanical-thermal properties
Neodym-YLF	526 (1053)	diode	High average power, high-speed applications

**Figure 3.3:** Quantronix Nd:YLF laser used for the present experiment

3.2.3 Imaging

The illuminated particles are usually imaged by digital cameras. The light scattered by the particles is focused on the camera sensor by the objective lens. The distance between the lens and the convergence point of the rays is the focal length f . For photographic lenses the following relation commonly holds

$$\frac{1}{f} = \frac{1}{d_1} + \frac{1}{d_2}, \quad (3.2)$$

with f indicating the focal length, d_1 the distance between the lens and the image plane and d_2 the distance between the lens and the object plane. The *Magnification factor* is defined as (M):

$$M = \frac{\text{image - size}}{\text{object - size}} = \frac{d_1}{d_2} (< 1), \quad (3.3)$$

this indicates the ratio between the dimensions of the real object and its image. The focal length scaled by the aperture of the objective is called *f-stop* or *f-number* $f_{\#}$. This (non-dimensional) number regulates the depth of field (DOF) with respect to the light intensity entering the objective. Increasing the f-number (decreasing the aperture) increases the depth of field, i.e. the region in focus around the object plane, but reduces the amount of light entering the objective. This parameter is particularly important during PIV calibration in

order to obtain sufficiently big particle imaging to avoid *peak-locking* (see section 3.2.5) still maintaining a high light intensity contrast. Plane light waves impinging on a screen with a small circular aperture undergo diffraction which modifies the image size. The light scattered by tracer particles when passing through the camera objective, even for perfectly aberration free lenses, generates circular diffraction patterns called *Airy rings*. The Airy function which describes the disks size equals the square of the first order Bessel function. The zero of the Airy function is determined by

$$\frac{d_{diff}}{2x_0} = 1.22, \quad (3.4)$$

with

$$x_0 = \frac{\lambda}{D_a},$$

where λ is the light wavelength and D_a is the aperture diameter. It can be noticed that the bigger the objective aperture the smaller is the diameter of the Airy ring, which is the smallest dimension of the imaged particle.

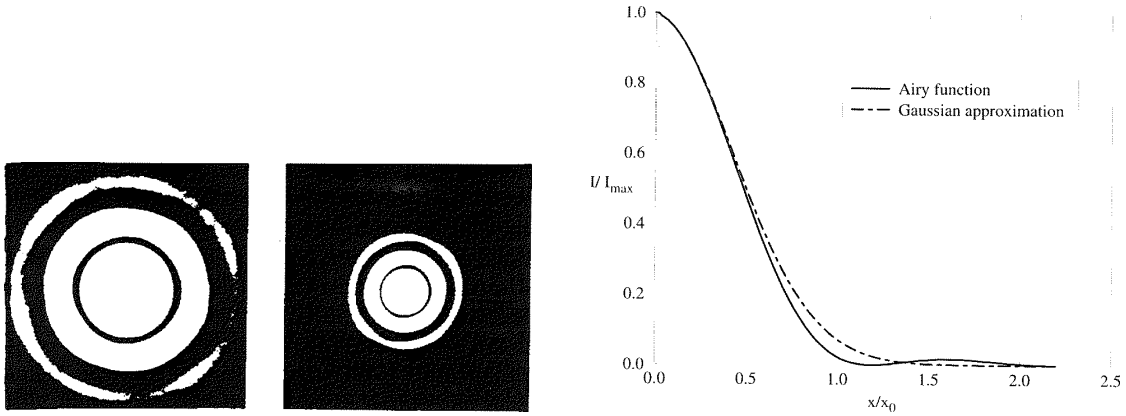


Figure 3.4: Airy pattern for different aperture (left) and Airy function compared to Gaussian function (right)

The relations (3.4), (3.2) and (3.3) can be combined together to give an approximate expression for the minimum “diffraction” limited particle image size

$$d_{diff} = 2.44f_{\#}(M + 1)\lambda. \quad (3.5)$$

The actual particle image diameter on the camera sensor can be estimated as

$$d_{im} = \sqrt{(Md_p)^2 + d_{diff}^2}, \quad (3.6)$$

where d_p is the real particle dimension and d_{im} is the imaged particle dimension. The depth of field (DOF) can be directly related to the previous quantities M , $f_{\#}$ and d_{diff} as

$$\delta_z = 2f_{\#}d_{diff}\frac{M + 1}{M^2}, \quad (3.7)$$

which shows a direct proportionality relation between the *f-number* and the DOF.

3.2.4 Recording

The image plane of the camera coincides with a sensor constituted of a 2-D array of pixels. The light collected by the sensor is digitally converted, for each pixel, into an intensity level on a gray scale. The optical and electronic characteristics of the sensors have a direct influence on the image acquisition rate and the errors connected to it. Developments of electronic recordings is very rapid. The most commonly used sensors nowadays are solid state charge coupled devices CCD and CMOS. The latter are based on active pixel sensor (APS) technology: each pixel is an isolated circuit and, in addition to the photo diode, can be provided with a local amplifier, usually MOS-FET type, or A/D converters. After the integration period the photo-electric charge is transferred through a row selector to a row bus and further amplified; the process is repeated for each row until covering the whole image. CMOS sensors allow higher image contrast with respect to CCD and eliminate blooming. These are preferred for high-speed applications since the pixel can be read out within one clock pulse while CCD cameras require 2 to 4 clock pulses per pixel read out. Cameras for high speed recording are usually provided with memory on board which allow storing the images before the transfer to the computer. The high-speed cameras for the present experiment were provided with CMOS sensors.

The camera shuttering time has to be synchronized with the time interval between the laser pulses such that to each camera exposition corresponds only one laser pulse. A sketch of this so called *frame straddling* mode for Double Frame/Single Exposure acquisition used for the present experiment is drawn in Figure 3.5. T_{shut} is the camera shuttering and data transfer

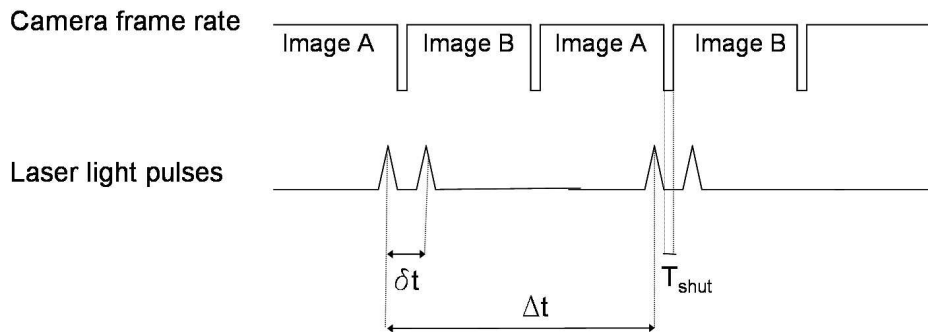


Figure 3.5: Timing diagram for PIV recording based on Double Frame/Single Exposure frame straddling mode

time, δt the laser pulses separation, Δt indicates acquisition time of an image couple.

3.2.5 Image analysis

In order to retrieve the velocity fields the acquired images have to be post-processed. There are several techniques available for image analysis. The first PIV analysis for low-seeded flows consisted in manually tracking the single particle displacement between two frames. This procedure gave scarce data density of the velocity vectors, which is indeed an increasing important matter for comparison of experimental results with numerical results. The required high data density can be achieved by means of statistical approaches based on cross-correlation

techniques ¹.

The complete image is split into small subregions called “interrogation windows”, usually containing a number of pixels power of 2: [32x32], [64x64], etc². Then cross-correlation of the light intensity for each pixel of the observation window (a) of image A is made with all the pixels of the observation windows (b) in image B, at the same location of window (a). The window (b) is shifted horizontally and vertically around the original location of window (a). Analytically the discrete cross-correlation function for a window of dimensions $[-w, w] \times [-h, h]$ can be formulated as

$$R(m, n) = \sum_{i=-w}^w \sum_{j=-h}^h I(i, j)I'(i + m, j + n), \quad (3.8)$$

where I and I' indicate the light intensity distribution on the pixels in the interrogation area at time t and $t + \Delta t$ respectively. The function $R(m, n)$ has dimensions $(4w-1) \times (4h-1)$. The distance between the correlation peak location and the origin $R(0, 0)$ indicates the most probable statistical particle displacement $\Delta \vec{x}$. Cross correlations are usually calculated as inverse transform of the power-spectrum, obtained as conjugated product of the FFT of I and I' , according to Wiener-Khinchin relationship (see Appendix B.2).

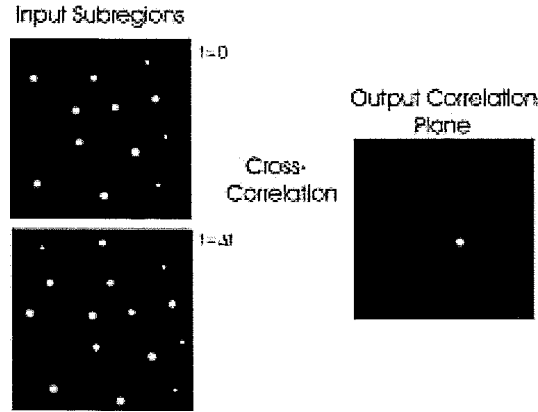


Figure 3.6: Cross-correlation of two PIV images at time t and $t + \Delta t$ [Wernet, 1999]

If the correlation is applied only on windows a_n of image A that surround the original window (a), the total number of displacement vectors $\Delta \vec{x}$ obtained from the correlations is equal to the total number of interrogation windows contained in one frame.

If the successive correlations are performed on windows a_n which partially overlap with the original position of window (a), more vectors are generated, resulting in a higher spatial resolution of the measurement, with unavoidably higher computational costs. The velocity field is then simply calculated, knowing the time interval Δt between the recorded image A and image B as

$$\vec{V} = \frac{\Delta \vec{x}}{\Delta t}. \quad (3.9)$$

PIV correlation techniques have to face the problem of particles escaping the computation domain, the so called *Loss-of-pairs*. There are two kinds of losses: in-plane loss-of pairs due to

¹See Appendix B for details on cross-correlation techniques.

²This fastens the FFT transforms, see Appendix B for details.

finiteness of the interrogation window and out-of-plane loss caused by 3D fluid motion. While the latter can only be eliminated by a 3D stereographic or tomographic approaches [20], the former can be minimized by selecting a proper dimension of the interrogation window or by exploitation of *Advanced Digital Interrogation Techniques*:

- Multiple pass interrogation
- Grid refining schemes
- Window deformation

PIV processing in the present work has been performed using the MATLAB software WIDIM (Window Deformation Iterative Multigrid) developed by Scarano and Riethmuller (1999) [44] and updated at the TU Delft. Standard correlation algorithms are based on the hypothesis of uniform particle velocity inside the interrogation window. This results to be not the case in presence of shear layers or high turbulent flows and would lead to broadening of the main peak and appearance of multiple peaks. The WIDIM algorithm first adopts a standard correlation approach on relatively big windows for a primary velocity estimation. The result is then used to deform the window (or the image) according to a low pass filtered velocity field.

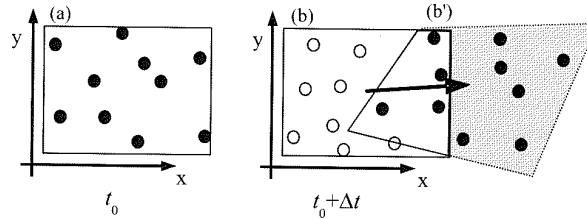


Figure 3.7: Window deformation based on previous velocity evaluation [Scarano *et al.*, 2002]

The process is repeated iteratively for a specified number of times decreasing the window size. The needed correction decreases at each iteration.

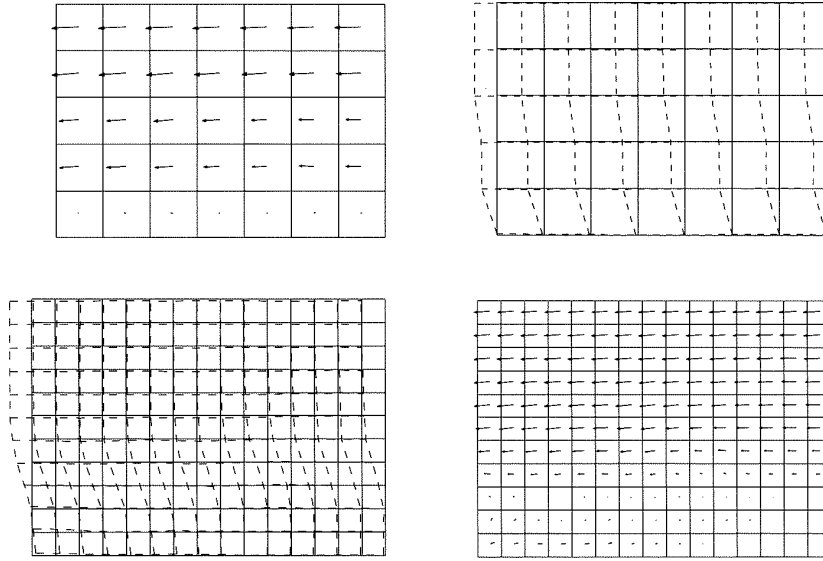


Figure 3.8: Iterative grid deformation and refinement [Scarano *et al.*, 2002]

The main advantages of the presented algorithm are:

- The main peak is located at the center of the interrogation window
- Peak broadening is reduced, reducing uncertainties in the velocity reconstruction.

A rule of thumb for a proper choice of the time separation between the laser pulses with respect to the dimensions of the observation window is that a particle should travel approximately $\frac{1}{4}$ of the window between the pulses. This can be achieved by tuning the laser pulse shift before the recording, foreseeing specific window dimensions and considering the particles moving at the free-stream velocity.

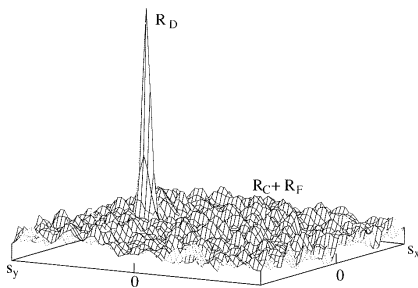


Figure 3.9: Main correlation peak (R_D) and minor correlation peaks (R_F R_C) [Raffel *et al.*, 1998]

The correlation algorithm would give a main peak value and minor peaks due to measurement noise. It is of crucial importance to distinguish between the main and the spurious peaks, i.e. to maximize the *Signal-to-Noise* ratio of the measurement. The signal-to-noise ratio in the specific case is defined as the ratio between the main peak and the sum of the minor peaks. The final space resolution of a PIV measurement depends on both optical effects (magnification factor, refractions) and processing parameters (window size, overlap, grid refinement).

When the imaged particles are much smaller than the pixel size the correlation algorithm produces a discontinuous velocity field. Only displacements that are integer multiples of the pixel size can be detected. This phenomenon is called *Peak-Locking* and it should be strongly avoided for a reliable PIV visualization. In the calibration phase the particles can be

slightly defocused on the image plane or the f -stop is increased in order to obtain dimensions of about 2-3 pixels per particle. With proper particle imaging dimensions it is possible to reveal displacements from 10 % up to 3 % of a pixel.

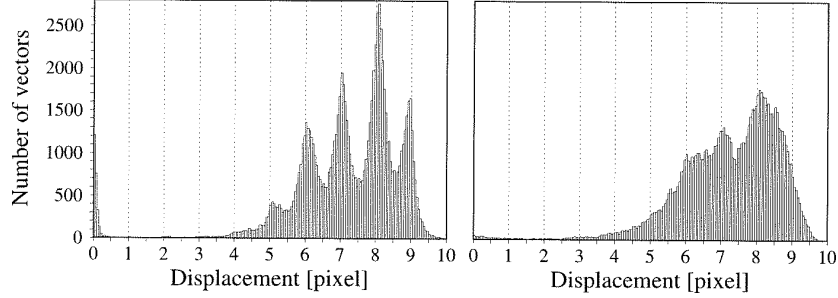


Figure 3.10: Effect of Peak-Locking on the displacement histogram. Peak locked image (left) continuous particle displacement (right) [Westermeel, 1998]

3.2.6 Time-resolved PIV (TR-PIV)

The advent of kilohertz-based repetition rate PIV systems allows the resolution of the time history of unsteady and turbulent flows at moderate flow speed. Reducing the time separation between pulse couples, Δt of Figure 3.5, it is possible to obtain a sequence of velocity vectors close enough to describe the dynamics of the flow. According to the sampling theory it is only possible to capture flow features with a maximum characteristic frequency below the Nyquist cut-off frequency, corresponding to half (or in practice even less) the camera acquisition frequency

$$F_{nyq} = \frac{F_s}{2} = \frac{1}{2\Delta t}.$$

Since sound propagation is an intrinsically unsteady phenomenon if one aims at describing the hydrodynamic causes of noise generation the knowledge of the time evolution of the flow field is an indispensable requirement. The time resolution of the velocity field allows for calculating the flow acceleration directly linked to the pressure gradient through the basic conservation equations of fluid mechanics. Pressure (and velocity) variations in time are responsible for the noise generation. An high time resolution of the velocity field would allow a reliable evaluation of the high frequency components of the computed noise spectrum.

The use of velocimetry in aeroacoustic predictions was not possible until now because of the relatively low acquisition rate of the laser-camera systems. The state of the art in modern PIV allows for image acquisitions at a rate of over 20,000 images per second with relatively high spatial resolution.

3.3 Microphone measurements

The most direct way to characterize an acoustic field is the measurement of the acoustic pressure fluctuations by means of calibrated microphones, also called “measuring microphones” [37]. A microphone is an acoustic-to-electric transducer, or sensor, that converts sound into an electrical signal [8]. The electrical signal can then be easily digitalized and processed using spectral analysis techniques. Microphones are generally classified depending on:

Measured quantity Pressure and velocity microphones.

Generation of the electric signal Condenser, capacitor, electrostatic microphones, etc.

Angular sensitivity Omnidirectional, unidirectional, cardioid microphones, etc.

In the present experiment for both far-field measurements and for the array system omnidirectional condenser pressure microphones LinearX-M51 were employed. A detailed description of several kinds of microphones with the relative functioning principles can be found in the technical documentation of Brüel & Kjær [1].

3.3.1 Condenser microphones

The electric signal in a condenser microphone is generated by the variation of the capacitance of a condenser. A sketch of the electronic scheme of a common condenser microphone is shown in Figure 3.11. One side of the condenser is constituted by a membrane which vibrates when forced by impinging acoustic waves. Variation of the distance between the membrane and the back plate generates an electric current, due to time variation of the capacitance, which is transformed into a voltage output through a resistor. The voltage measured across the resistor is an electrical image of the sound pressure which moves the membrane.

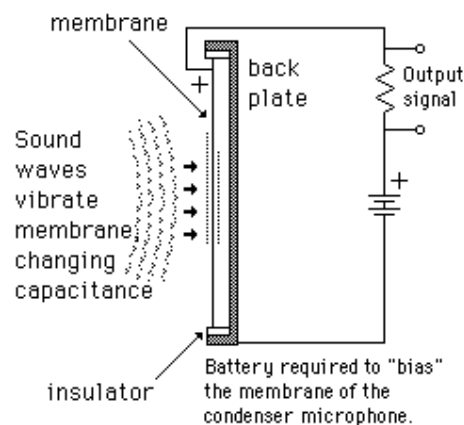


Figure 3.11: Electronic scheme of a typical condenser microphone

3.3.2 Microphone sensitivity

The sensitivity of a microphone is defined as the ratio between the output voltage and the amplitude of the pressure signal at the membrane. The sensitivity response varies both with

the inclination of the acoustic rays with respect to the microphone axis and the frequency. For an omnidirectional microphone the angular sensitivity, i.e. the solid angle θ measurable by the microphone, decreases as the frequency of the sound increases. The angular sensitivity of a LinearX-M51 microphone is shown in Figure 3.12.

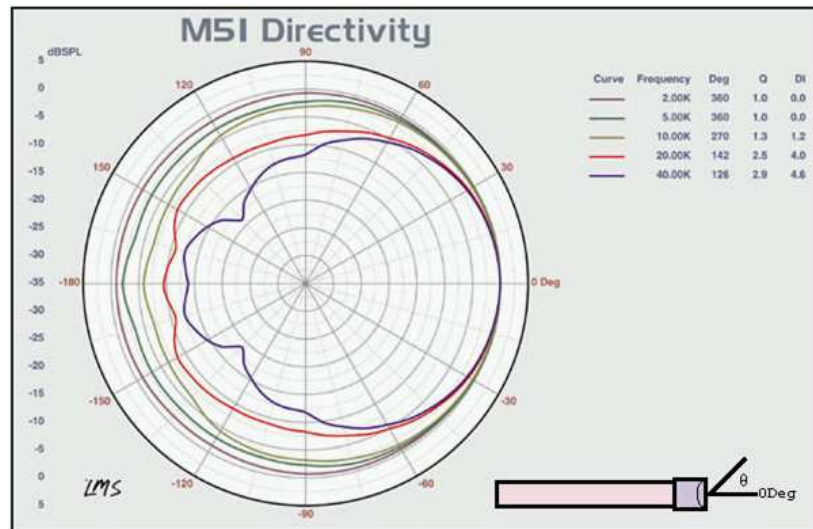


Figure 3.12: Directivity of an omnidirectional LinearX-M51 microphone vs frequency [LinearX, 2006]

For low frequencies the sensitivity of the microphone is mostly omnidirectional, while for frequencies above the 10 kHz the sensitivity lobe moves towards the front, which indicates a reduction of the directional sensitivity. The response to radiation in the direction aligned with the microphone axis does not change with frequency. Also the amplitude of the microphone response depends on the frequency of the acoustic signal. The frequency response of the Linear X-51 microphones is indicated in Figure 3.13 (left). For very low frequencies which correspond to larger oscillations the membrane displacement range becomes insufficient. For frequencies above 10 kHz the response initially increases and then rapidly drops down because the time lag of the membrane-condenser system with respect to the pressure fluctuations causes an out of phase cancelation of the detected signal. The response can be corrected by calibration of the microphone in order to obtain a constant response of the microphone with the frequency. The corrected response for a LinearX-M51 microphone is shown in Figure 3.13 (right).

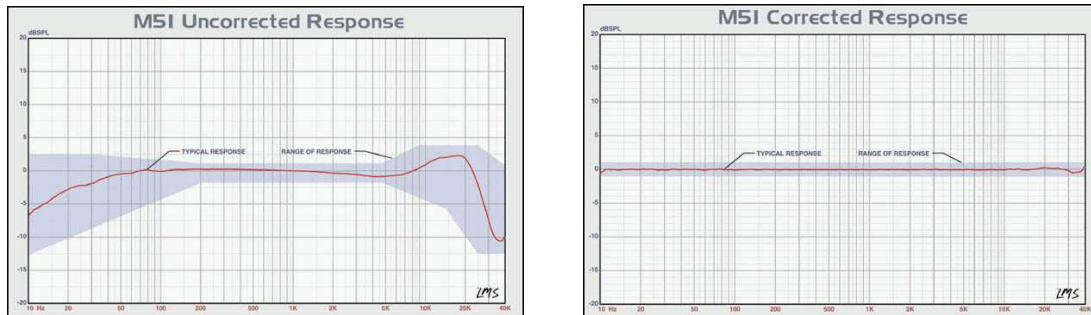


Figure 3.13: Original microphone response with frequency (left) and corrected microphone response (right) [LinearX, 2006]

In order to give an absolute measure of the sound field, calibration of the microphones is required. This can be performed by the user or can be directly provided by the constructor. Each microphone has different calibration parameters. Calibration of a measuring microphone, as personal experience of the author, is far from trivial since it requires a constant known source strength at a specific position in a purely anechoic environment.

The technical chart of a microphone indicates the construction characteristics and specifics for the use. An example of the technical chart of LinearX-M51 microphone is shown in Figure 3.14

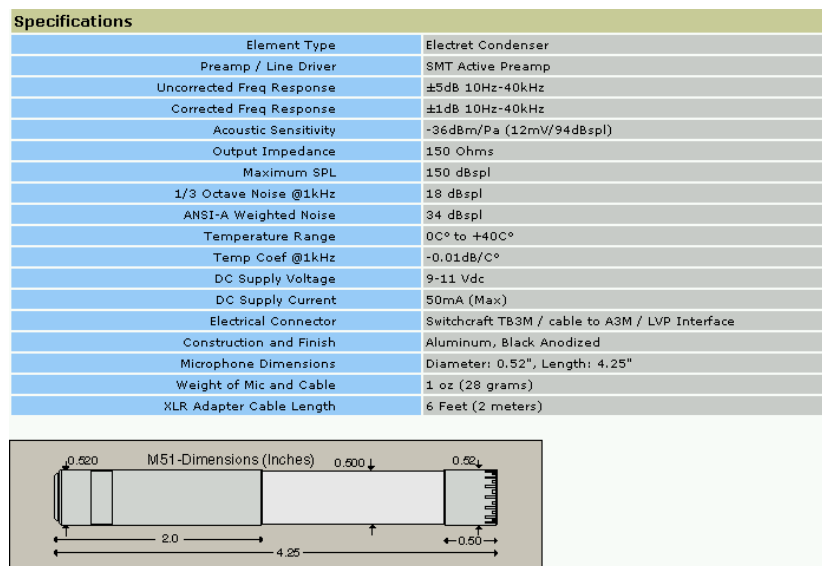


Figure 3.14: Technical chart of a LinearX-M51 microphone [LinearX, 2006]

The voltage output provided by the microphone is connected to an acquisition system and sampled at acquisition frequencies usually far above the frequency range of the microphone. Digitalization of the signal is performed by AC-DC converters and the resulting digital signal is analyzed according to spectral analysis techniques (see Appendix B).

The use of a single microphone does not provide information about the localization of the noise emitting source. This can only be achieved by the simultaneous use of several microphones

(at least two) and reconstruction algorithms. A set of simultaneously operating microphones is referred to as a “microphone array”.

3.4 Acoustic source localization techniques

The first step to attain active noise control is the localization of the sources of noise. For many years source detection has been carried out by means of acoustic mirrors. These are based on the principle of converging the rays emanated by an acoustic source to a “focal point” where a microphone is placed. The scan point is then moved at the locations of interest for the measurement by the relative movement of the object and the measurement system. The acoustic mirrors allows for detection of a wide range of frequency with a high efficiency in background noise filtering. The main drawback of this method is the long time needed for measurements. An application of the acoustic mirror for a wind tunnel measurement is shown in Figure 3.19.

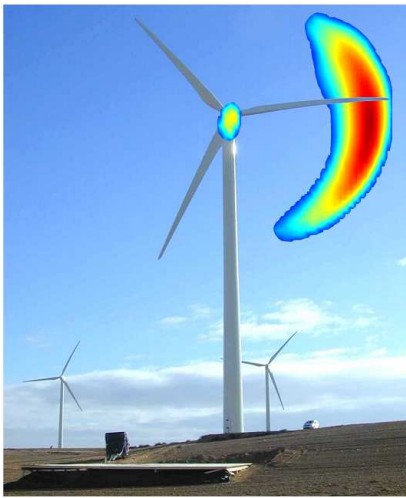


Figure 3.15: Beamforming source localization on rotating system [Oerlemans *et al.* 2007]

The technique of locating sources using phased microphone arrays is called “beamforming”. This is an algorithm applied to all the points of a scan plane. The signal recorded by each microphone of the array is time shifted (or equivalently phase shifted in the frequency domain) and modulated in amplitude to simulate the response to a potential source located at one point of the scan plane. During the processing the unknown source is moved all over the scan plane. If the position of the latter does not coincide with the actual source position the effect is the cancelation of the microphone signals due to random phase shift. Conversely if the scan point coincides with the

Modern techniques for noise source detection are based on the so called “beamforming algorithms” [50], [30] and the use of acoustic arrays. An acoustic array is a set of microphones, of which the signals are combined in such a way that sound from a specified scan point is amplified and sound from other directions is attenuated. The signals of all the microphones are combined together thorough an appropriate delay and sum processing in time domain or a corresponding phase shift in frequency domain. Only short measurements times are needed since, unlike acoustic mirrors, the scanning process is performed afterwards by softwares.

Microphone arrays are also capable to locate acoustic sources on moving objects as show in Figure 3.15 and Figure 3.16. It has been recently applied for objects in steady rectilinear motion, like trains passing by [5] and airplanes flying over [39] and rotating machinery as windmills and helicopters [51].

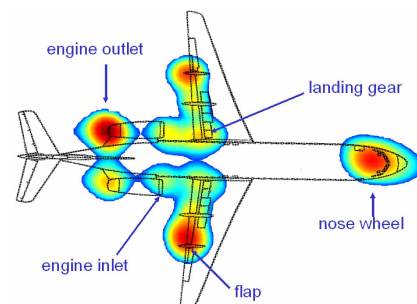


Figure 3.16: Beamforming source localization on moving body [Sijtsma *et al.* 2002]

actual noise source the algorithm gives maximum output in the evaluation of the source strength because of in-phase build up of all the microphone signals (see sketch in Figure 3.18).

Beamforming techniques can be performed both in the *time domain* and in the *frequency domain*. Most of the practical applications rely on frequency analysis of the microphone recorded signal since, unlike the time domain approach, it does not require the computation of the auto-correlation of the source signal. The principles of the most common beamforming algorithms are presented in the following sections.

3.4.1 Time-domain beamforming

Given the set of N microphones located at $\vec{x}_n = (x_n, y_n, z_n)$ with n ranging from 1 to N . Each microphone records a pressure signal

$$p_n(t) = p(\vec{x}_n, t). \quad (3.10)$$

Since the array covers only a small portion of the solid angle of the directivity pattern of a source, for far enough distances of the array from the source location, the emission directivity of a generic source can be assumed to be that of a monopole. An unknown point (monopole) source with uniform directivity is assumed to be positioned at location $\vec{\zeta}_0$ on a scan plane as shown in Figure 3.17.

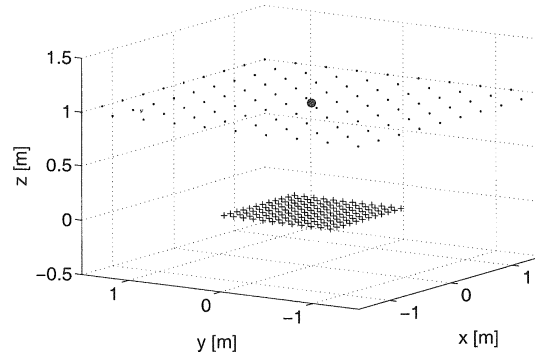


Figure 3.17: Example of microphones locations (crosses) and scan point locations (dots)

The acoustic pressure field at a general position x at time t is

$$p(\vec{x}, t) = \frac{\sigma(t - \Delta t_e)}{4\pi\|\vec{x} - \zeta_0\|}, \quad (3.11)$$

in which σ indicates emitted signal and Δt_e is the propagation time delay depending on the speed of sound c and distance between the source and the receiver as follows

$$\Delta t_e = \frac{\|\vec{x} - \zeta_0\|}{c}. \quad (3.12)$$

Delay and sum

Each microphone signal is multiplied with the distance from the potential source and time-shifted as follows

$$\bar{\sigma}(t) = \frac{1}{N} \sum_{n=1}^N 4\pi\|\vec{x}_n - \vec{\zeta}\| p_n(t + \Delta t_{r,n}), \quad (3.13)$$

where $\bar{\sigma}(t)$ is the estimated source signal and $\Delta t_{r,n}$ is the retarded emission time of the n -th microphone: $\Delta t_{r,n} = \frac{\|\vec{x}_n - \zeta\|}{c}$. Substituting the actual but unknown pressure field given by equations (3.11) into (3.13), we obtain

$$\bar{\sigma}(t) = \frac{1}{N} \sum_{n=1}^N \frac{\|\vec{x}_n - \vec{\zeta}\|}{\|\vec{x}_n - \vec{\zeta}_0\|} \sigma \left(t + \frac{1}{c} [\|\vec{x}_n - \vec{\zeta}\| - \|\vec{x}_n - \vec{\zeta}_0\|] \right). \quad (3.14)$$

When the guessed source location ζ coincides with the actual source ζ_0 the phase shift between the evaluated responses of all the microphones is zero and the algorithm gives maximum output, i.e. $\bar{\sigma}(t) = \sigma(t)$. For other locations $\|\bar{\sigma}(t)\| < \|\sigma(t)\|$ because of mutual cancellation of the signals due to the phase shift. A sketch of the principle of delay and sum beamforming algorithm is shown in Figure 3.18.

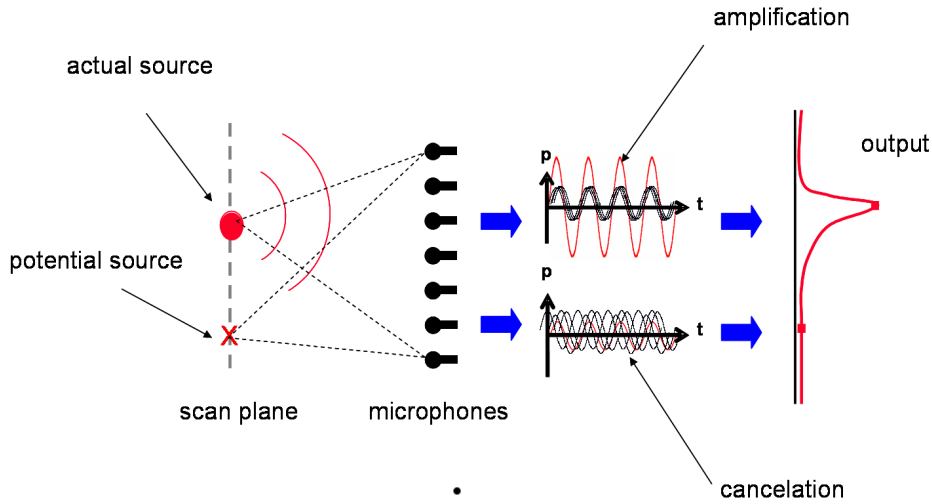


Figure 3.18: Principle of the delay and sum beamforming algorithm

Least squares

Another possible beamforming time domain algorithm is the so called Least Squares Beamforming. The source position is here estimated through minimization of the squared difference between the actual microphone signal and the signal that would be produced by a potential source at location ζ , for all the microphones. Minimization of quantity

$$J = \sum_{n=1}^N \left\| p_n(t + \Delta t_{e,n}) - \frac{\bar{\sigma}(t)}{4\pi\|\vec{x}_n - \vec{\zeta}\|} \right\|^2, \quad (3.15)$$

yields the expression

$$\bar{\sigma}(t) = \frac{\sum_{n=1}^N \frac{p_n(t + \Delta t_{e,n})}{4\pi\|\vec{x}_n - \vec{\zeta}\|}}{\sum_{n=1}^N \frac{1}{(4\pi\|\vec{x}_n - \vec{\zeta}\|)^2}}. \quad (3.16)$$

Substituting for the actual pressure of equation (3.11) into equation (3.16), the following expression results

$$\bar{\sigma}(t) = \frac{\sum_{n=1}^N \frac{\sigma\left[t + \frac{1}{c}(\|\vec{x}_n - \vec{\zeta}\| - \|\vec{x}_n - \vec{\zeta}_0\|)\right]}{(4\pi\|\vec{x}_n - \vec{\zeta}\|)(4\pi\|\vec{x}_n - \vec{\zeta}_0\|)}}{\sum_{n=1}^N \frac{1}{(4\pi\|\vec{x}_n - \vec{\zeta}\|)^2}}. \quad (3.17)$$

Again for $\zeta = \zeta_0$ the maximum output $\bar{\sigma}(t) = \sigma(t)$ is retrieved. The main difference between Delay and Sum and Least Squares Beamforming is the relative weight of the microphone signals. For Delay the microphone signal is multiplied with the distance while in the Least Square method the signal is divided by the distance. Thus, for noisy signals, the Least Square is preferable to Delay and Sum especially if the microphones are relatively far from the sources. The right hand side of equation (3.17) is difficult to quantify in the case $\zeta \neq \zeta_0$ unless the auto-correlation of the signal for each microphone is known. The knowledge of the signal decay around the source is an important parameter for the spatial resolution of the array measurement. Resolution issues are easily treated if the frequency-domain approach is used.

3.4.2 Frequency-domain Beamforming

When the Discrete Fourier transform, as described in Appendix B, is applied to the actual source signal σ and the estimated signal $\bar{\sigma}$, equation (3.17) becomes

$$\bar{a}(f) = a(f) \frac{\sum_{n=1}^N \frac{\exp\left[\frac{2\pi i f}{c}(\|\vec{x}_n - \vec{\zeta}\| - \|\vec{x}_n - \vec{\zeta}_0\|)\right]}{(4\pi\|\vec{x}_n - \vec{\zeta}\|)(4\pi\|\vec{x}_n - \vec{\zeta}_0\|)}}{\sum_{n=1}^N \frac{1}{(4\pi\|\vec{x}_n - \vec{\zeta}\|)^2}}. \quad (3.18)$$

The ratio between the actual signal amplitude $a(f)$ and the expected amplitude $\bar{a}(f)$ is independent of the source characteristics. The time signal detected by a microphone at the position \vec{x} in equation (3.11) can be expressed in frequency domain as follows

$$p(\vec{x}, f) = \frac{a(f)e^{-2\pi i f \Delta t_e}}{4\pi\|\vec{x} - \zeta\|}, \quad (3.19)$$

where $a(f)$ is the Fourier transform of $\sigma(t)$ as shown in Appendix B.3, or simply

$$p(\vec{x}, f) = a(f)g(\vec{x}, t). \quad (3.20)$$

in which

$$g(\vec{x}, f) = \frac{e^{-2\pi i f \Delta t_e}}{4\pi\|\vec{x} - \zeta\|}, \quad (3.21)$$

is the Green's function for the Helmholtz equation in a steady medium (see [27])

$$\nabla^2 g + \left(\frac{2\pi f}{c}\right)^2 g = -\delta(\vec{x} - \vec{\zeta}). \quad (3.22)$$

The Green's function g indicates the signal in frequency-domain at point \vec{x} produced by the unity amplitude monopole source positioned at ζ . If the acoustic wave is propagated in

a uniformly moving medium, for example in a wind tunnel, a more appropriate convected Helmholtz equation can be used, of the kind

$$\nabla^2 g + \frac{1}{c^2} (2\pi f + U \cdot \nabla)^2 g = -\delta(\vec{x} - \vec{\zeta}), \quad (3.23)$$

whose solution is

$$g(\vec{x}, f) = \frac{e^{-2\pi i f \Delta t_e}}{4\pi \sqrt{\vec{M} \cdot (\vec{x} - \vec{\zeta})^2 + \beta^2 \|\vec{x} - \zeta\|^2}}, \quad (3.24)$$

where \vec{M} is a vector Mach number:

$$\vec{M} = \frac{\vec{U}}{c},$$

and

$$\beta^2 = 1 - \|\vec{M}\|^2.$$

If sources with more complex directivity are considered, for example dipoles or quadrupoles, the Green's function indicated in equation (3.21) has to be partially derived with respect to the spatial source coordinate, respectively once or twice for dipoles and quadrupoles. First (-second) order partial derivative of the Green's function is representative of dipole (-quadrupole) source radiation (see Section 2.4.1).

Conventional beamforming

The pressure amplitudes of all the N microphones can be rewritten for brevity in a unique vector \mathbf{p} of length N :

$$\mathbf{p} = \begin{Bmatrix} p_1(f) \\ p_2(f) \\ \cdot \\ \cdot \\ p_N(f) \end{Bmatrix}.$$

The cross-power matrix C , containing the power spectrum of each microphone, is defined, according to Wiener-Khinchin relationship (see Appendix B), as the product of the spectrum of each microphone with the complex conjugate spectrum of all the other microphones. In compact form:

$$C = \frac{1}{2} \mathbf{p} \mathbf{p}^* \quad (3.25)$$

In the same way as for the Least Square method, the minimization of the difference between actual signal recorded by the microphone (in frequency domain in this case) and the signal produced by a potential source at location ζ allows localization of the real source. The quantity to be minimized is:

$$J = \|\mathbf{p} - \bar{a} \mathbf{g}\|^2 \quad (3.26)$$

the solution of the minimization problem is:

$$\bar{a} = \frac{\mathbf{g}^* \mathbf{p}}{\|\mathbf{g}\|^2} \quad (3.27)$$

It is usually convenient considering the auto-spectrum of the estimated amplitude function \bar{a} in the following way:

$$\bar{A} = \frac{1}{2} \bar{a} \bar{a}^* = \frac{\mathbf{g}^* C \mathbf{g}}{\|\mathbf{g}\|^4} \quad (3.28)$$

The above equation (3.28) is known as ‘‘Conventional Beamforming’’ and is the equivalent, in the frequency domain, of the Least Square Beamforming in time domain. The maximum output of the Conventional Beamforming technique generates a peak value for a specific frequency range at a certain spatial location where the source is expected to be.

Microphone array measurements can be performed in scaled wind tunnel tests or directly on the real configuration during operating conditions. An example of a wind tunnel test on a landing gear using microphone array combined with acoustic mirror measurements is shown in Figure 3.19 (top). Beamforming measurements on landing airplane have been performed by Sijtsma *et al.* in Schipol airport using the setup shown in Figure 3.20.

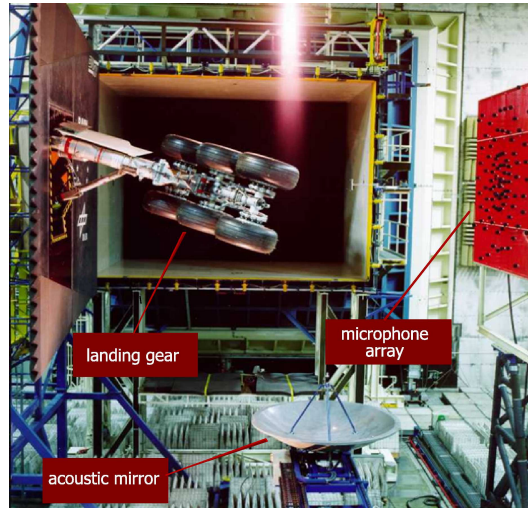


Figure 3.19: Wind tunnel test on a Boeing landing gear using a microphone array and an acoustic mirror [NLR, 2004]

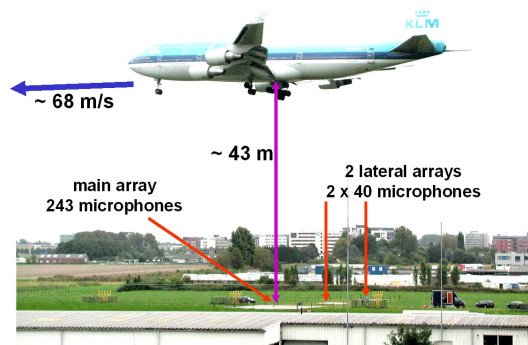


Figure 3.20: Beamforming array measurements on a landing airplanes [NLR, Schipol airport 2002]

Microphone arrays offer a large flexibility. It is nowadays the most powerful tool for experimental detection of aeroacoustic sources.

Array resolution and optimization The capability of distinguishing the acoustic source position with respect to neighboring points, is called resolution of the array. This is mathematically defined as the distance across which the peak has a 3 dB amplitude decay. In conventional beamforming a rule of thumb to estimate the spatial resolution of an array is

$$\Delta_{3dB} = \frac{425Y}{Df}, \quad (3.29)$$

in which Y is the distance between source and array, D is the diameter of the array and f is the signal frequency. The above expression indicates that the array resolution increases, meaning that the sources are better defined in space, as the frequency of the acoustic source or the relative distance between the microphones increase. This is due to a more pronounced phase shift of the microphone signal with one another during the reconstruction processing. The mentioned beamforming techniques can be optimized for side lobes suppression through signal processing and specific array design techniques as well as for moving sources and boundary layer noise elimination. An example of the microphone disposition for optimization of an array is shown in Figure 3.21

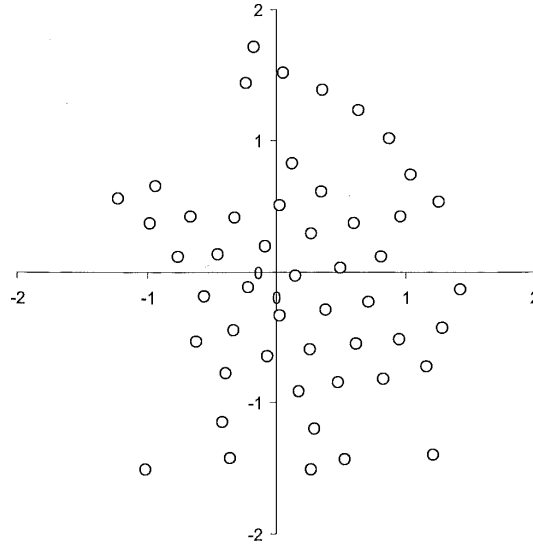


Figure 3.21: Example of microphone disposition for array optimization

These optimization techniques go beyond the scope of this general description, more details on array optimization can be found in [50].

Chapter 4

Experimental campaign

This chapter presents the results of the combined PIV and acoustic experiments carried out at the Dutch “National Aerospace Laboratory NLR”. The purpose of the experimental campaign was to obtain the unsteady flow field around an airfoil immersed in the Karman wake of a circular section rod and to measure the corresponding acoustic emission.

Beamforming technique allowed for the localization of the acoustic sources. Visualization of the time-evolving fluid structures all around the airfoil was provided by time-resolved planar PIV (see Chapter 3 for details about the techniques). Several fields of view have been examined for the visualization of specific flow features or to locally increase the spatial resolution of the velocity measurement. The most relevant observation window also for further pressure measurements is referred to as FOV-2CAM (see description in Section 4.4.2), which resulted from the use of two cameras and allowed the visualization all around the airfoil. In a preliminary phase acoustic measurements were performed for the estimation of background noise and the determination of the geometric far-field. Additional velocity measurements were performed in order to assess the spanwise correlation of the vortex impingement onto the airfoil leading edge.

The obtained velocity data have been used to calculate the planar pressure field around the airfoil by means of a Poisson based pressure deduction algorithm (see Chapter 5). The pressure and velocity data on a prescribed surface around the airfoil served as input to determine the source terms of the implemented aeroacoustic analogies.

4.1 Experimental facility

The experiment was carried out at NLR-NOP in the small anechoic facility (KAT), configured with a rectangular type nozzle. The nozzle has dimensions of $0.51 \times 0.38 \text{ m}^2$. The anechoic chamber is $5.5 \times 5.5 \times 2.5 \text{ m}^3$ large and covered with 0.5 m long foam wedges, yielding 99 % acoustic absorption above 500 Hz . A cylindrical rod was vertically mounted 22 cm (varying slightly case by case) downstream of the wind tunnel exit. A NACA0012 Plexiglas airfoil, with a chord of 10 cm, was vertically placed in the wake of the rod at zero degrees angle of attack. Both rod and airfoil were mounted on a rail system which allowed easy adjustment of the rod position and the rod-airfoil distance. The top edges of rod and airfoil were held by a connection to the frame of the wind tunnel exit nozzle. Two different cylinders of 0.6 cm

and 1 *cm* diameter were used in order to assess the effect on the sound generation, as a result of the variation of dimension and shedding frequency of the vortices. Each configuration was examined for three different free stream velocities of 10, 15 and 20 *m/s* respectively. A sketch of the experimental arrangement is shown Figure 4.1. The Reynolds number for the three

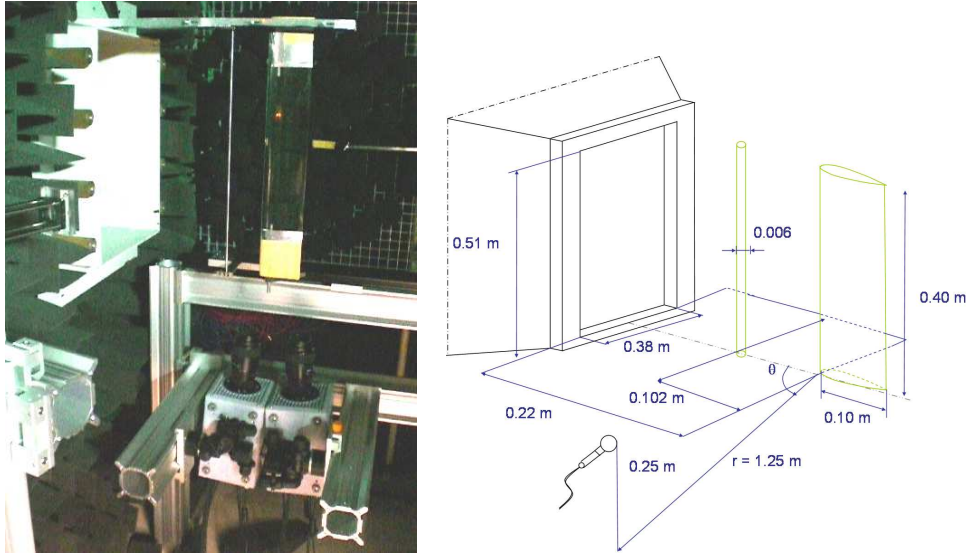


Figure 4.1: Schematic of the rod-airfoil configuration and dimensions for $V = 15 \text{ m/s}$ and a rod diameter of 6 *mm* (RUN 32 FOV 2CAM of the NLR report [34])

different velocities ranged approximatively from 80,000 (10 *m/s* free-stream) to 180,000 (20 *m/s* free-stream) with respect to the airfoil and from 5,000 to a maximum of 16,000 with respect to the cylinders. The flow Mach number at the measured environment pressure and temperature varied slightly around the value 0.043 for all the runs.

During the acoustic measurements in order to avoid possible acoustic reflections the rail system, the laser box and laser generator were covered in absorbing foam.

4.2 Acoustic measurement system setup

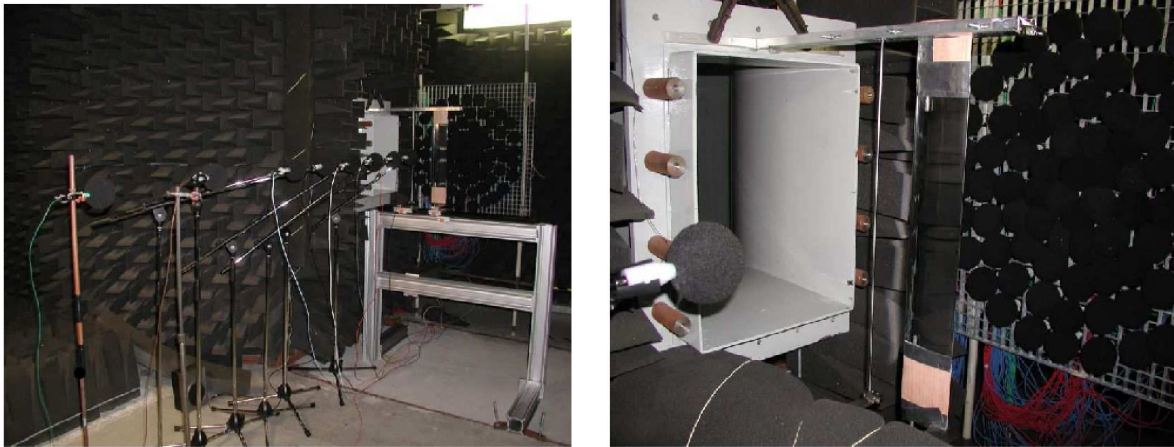
The acoustic measuring system consisted of a microphone array and two configurations of far field microphones. The circular microphone-array was placed at 0.675 *m* from the heart of the tunnel and was approximately 0.8 *m* in diameter. Two GBM-Viper systems, yielding a total number of 96 available channels, were used for the acoustic data acquisition. The 80 LinearX-M51 microphones used for the array were positioned in an unstructured manner to avoid spurious source detection. The scan plane overlapped with a surface spanned by the airfoil and cylinder at the heart line of the wind tunnel. A grid resolution was selected of 0.5 *cm* in both horizontal and vertical direction.

The specifics of the acoustic processing are indicated in Table 4.1

Table 4.1: GBM-Viper Specifics

Sample frequency:	51.2 kHz
Measuring time:	20 s
High-pass filter:	1 Hz
Low-pass filter:	25.6 kHz
Block size:	4096
Window:	Hanning
Overlap:	50%
Number of averages:	500
Frequency resolution:	12.5

The first set of microphones was constituted by eight in-line microphones used to determine the acoustic far-field. These were placed at half-span and perpendicular to the airfoil at a distance of 0.35, 0.6, 0.85, 1.1, 1.35, 1.6, 2.1 and 2.6 m as shown in Figure 4.2(left).

**Figure 4.2:** Eight in-line microphones for far-field check (left) and microphone array (right)

The second configuration of far-field microphones was used to record acoustic emission simultaneously to PIV measurements. Four free field microphones were placed at a fixed distance of 1.25 m from the airfoil leading edge, at an angle, with respect to the airfoil chord of 90° , 117° , 135° , 143° , as shown in Figure 4.3.

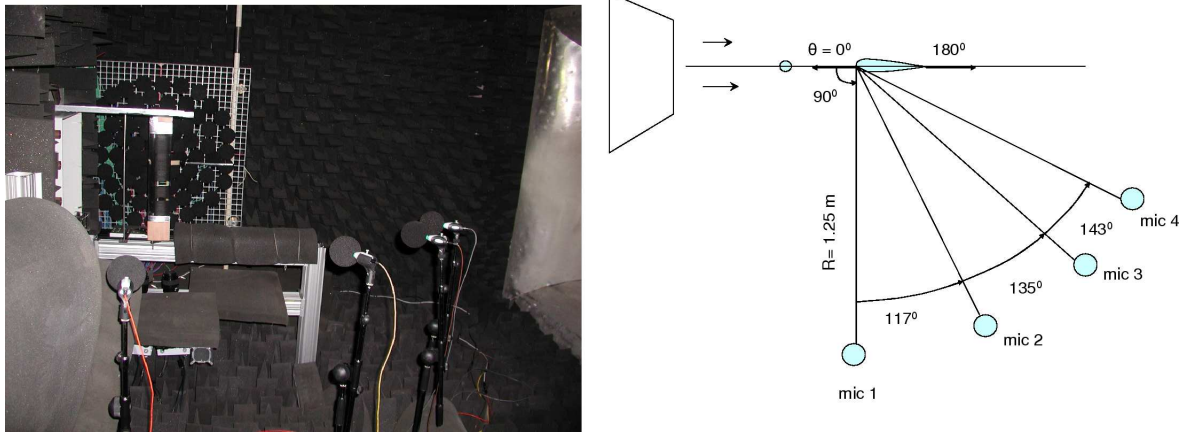


Figure 4.3: Far-field microphones set up (left) for directivity detection, top view schematic of microphones disposition (right)

On all array microphones wind shields were placed to prevent the acoustic measurements being affected by air flow passing over the microphones. The far field microphones were covered with wind shields as well, to ensure that if there was to be an influence of a wind shield on the sound measurements, all microphones would have been similarly influenced.

4.3 PIV system setup

Two-component time-resolved particle image velocimetry (2C-TR-PIV) was used to obtain planar velocity field measurements around the airfoil. By use of a Safex stage smoke generator the flow was seeded with particles of approximately $1 \mu\text{m}$ diameter. The seeding was introduced at the inlet of the wind tunnel system, which provided a homogeneously seeded flow at the test section.

The seeding was illuminated by a Quantronix Darwin Duo Nd-YLF laser. The light sheet was introduced from the side, slightly at an angle upstream with respect to the test section axis as shown in Figure 4.4. The light sheet was placed at the middle span section of the airfoil. The transparent material of the airfoil allowed the measurement of the flow-field on the opposite side of the airfoil, with exception of two shadow zones caused by light refraction through the model.

The laser was mounted perpendicularly to the incoming flow at the height of the middle span section of the airfoil. The pulse frequency was set to 2700 Hz in double-pulsed mode. The nominal pulse energy of the laser is 25 mJ at 1 kHz and is estimated to be 12 mJ at 2700 Hz. The laser pulses have a wavelength of 527 nm (visible green light) and duration of 120 ns. The time interval between the laser pulses was varied depending on the flow velocity in order to obtain a particle image displacement of approximately 10 pixels. The light sheet had a thickness of approximately 2 mm.

Two Photron Fast CAM SA1 CMOS cameras (1024x1024 pixels, 12-bit, 20 μm pixel pitch) were used for the image acquisition. The cameras can operate at full frame at a maximum frame rate of 5.4 KHz and have a storage capacity of 8 GB, allowing the acquisition of a

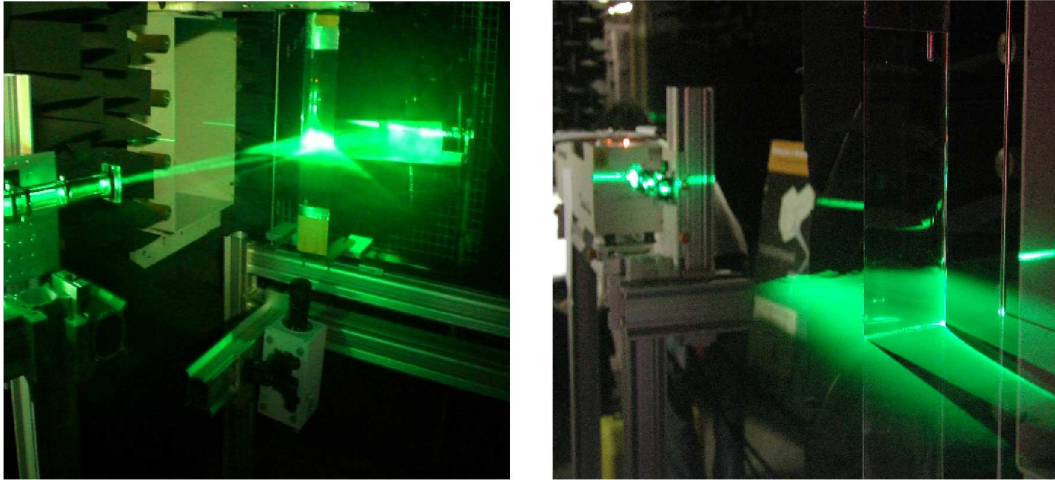


Figure 4.4: Overview of the region illuminated by the laser (left) and shadow regions behind the airfoil (right)

maximum of 5400 images (2700 pairs, 1 s) in a single measurement. The acquisition frequency was set to coincide with the frequency of the laser pulse couple in double frame acquisition mode (2700 Hz). Two cameras were employed to increase the spatial resolution. A slight inclination with respect to the vertical plane perpendicular to the airfoil cord (approximately 2°) of the optical axes of the imaging was necessary in order to obtain overlapping fields of view. Each camera was equipped with a Nikon objective with a focal length either 105 or 60 mm in order to capture the required field of view. The numerical aperture was set to $f\# = 2.8$. The synchronization between laser and camera was performed by means of a LaVision High-Speed controller and by the DAVIS 7.2 software package. Image processing was done with an iterative multi-grid window deformation technique implemented in the WIDIM software developed by Scarano and Riethmuller (1999) [44]. Spanwise visualization at mid-span height have been made using a single camera. The light was vertically redirected by a mirror placed underneath the airfoil as shown in the Figure 4.5.

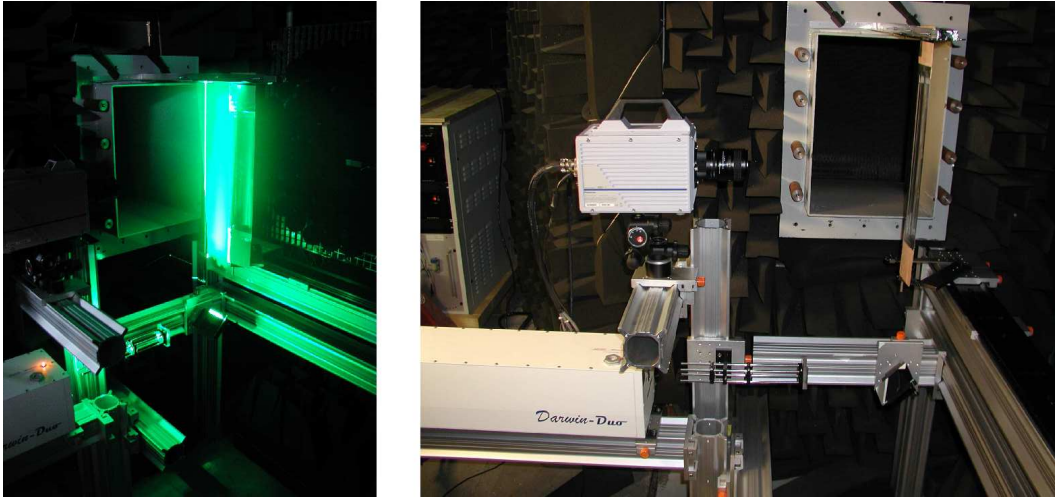


Figure 4.5: Laser orientation (left) and camera location (right) for spanwise measurements

4.4 Results of the experimental campaign

The results directly obtained from the eight inline microphones, perpendicular to the airfoil, were used to determine the acoustic far-field. For several measurements it was investigated how the sound pressure level decayed with distance from the source. Sufficiently far from the source, in the geometric far-field, a $1/R$ decay is expected. The Figure 4.6 (left) shows the narrow band spectra of the eight microphones, scaled to a reference distance of 1.25 m , for a rod-airfoil configuration with a 6 mm rod at $V = 20\text{ m/s}$.

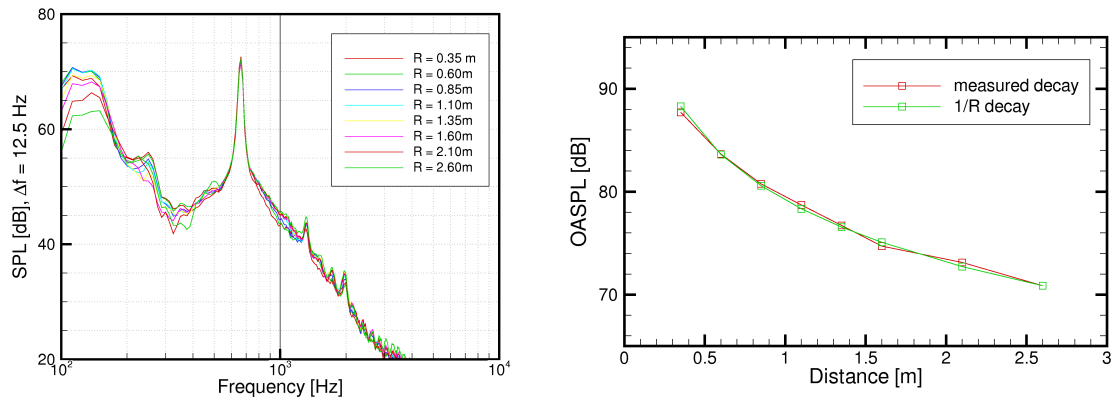
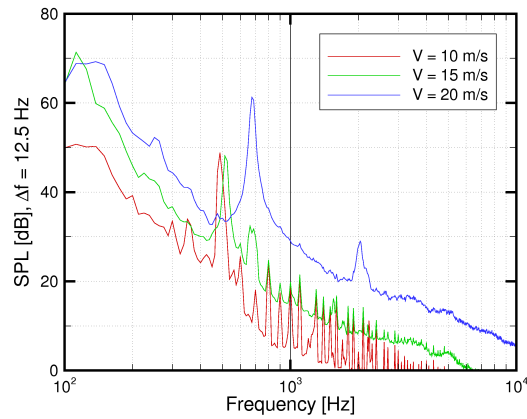


Figure 4.6: Small band spectra of the eight in-line microphones scaled to 1.35 m (left) and OASPL at microphone locations (right)

A cylindrical rod placed in a flow is known to possess a shedding frequency related to a Strouhal number of 0.21. From this relation the expected shedding frequency of Table 4.2 are calculated:

Table 4.2: Expected rod-shedding frequency at $St = 0.21$

	D [mm]	4	6	10
V [m/s]				
10		525	350	210
15		750	525	315
20		1050	700	720

**Figure 4.7:** Rod-alone noise narrow band spectra for $V = 10, 15$ and 20 m/s , rod diameter = 6 mm , $R = 1.25 \text{ m}$

The measured values of Figure 4.7 show good agreement with the expected Strouhal number of Table 4.2. At $10, 15$ and 20 m/s a measured Strouhal number of $0.211, 0.205$ and 0.202 is found. The first harmonic peak, corresponding to the Strouhal frequency of 350 Hz , for the 10 m/s case is not clearly visible but can be distinguished. This is due to acoustic masking caused by the wind tunnel noise. The peak of 487 Hz was shown to be related to the wind tunnel fans at speed of 10 m/s by the array plots in preliminary background noise measurements.

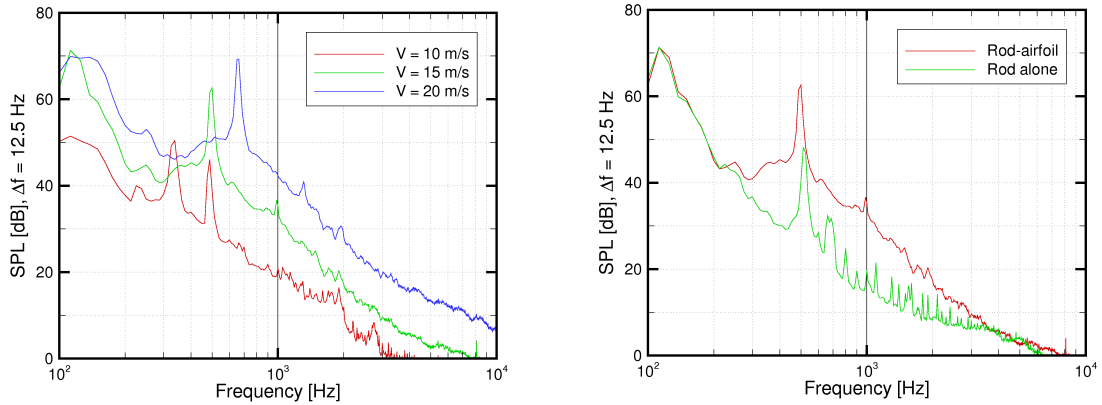


Figure 4.8: Rod-airfoil noise narrow band spectra for $V = 10, 15$ and 20 m/s , rod diameter = 6 mm , distance rod-airfoil = 10.2 cm , $R = 1.25$ (left) and rod alone vs rod-airfoil noise (right)

It was demonstrated by M. Jacobs in [29], by means of correlations of the flow structures with measured sound signal, that the noise produced by the airfoil in a rod-airfoil configuration is mainly due to the impingement of the vortices, shed by the cylinder, onto the aft part of the airfoil. The same localization of the noise sources on the airfoil surface can be observed in the array plots of Figure 4.18. The noise peak frequency is expected to correspond to the rod shedding frequency. This is also confirmed by the plots of Figure 4.8 (left). The first harmonic at 10 m/s , unlike Figure 4.7, is now clearly visible. The peaks for all the velocities are shifted to slightly lower frequencies with respect to the rod alone case of 4.7. A possible explanation, also proposed by Casalino in [10], is a hydrodynamic-acoustic feedback of the airfoil upon the cylinder shedding mechanism. The presence of the airfoil increases the intensity of the noise emitted by the rod of over 10 dB , as featured in 4.8 (right). A shift of the peak frequency from 525 Hz to 500 Hz and a broadening of the spectrum around it is noted. The appearance of a secondary harmonic peak at about 1000 Hz can be distinguished for the rod-airfoil configuration.

The PIV results for the most interesting runs for the purpose of the present investigation are indicated in the following sections. For a complete description of each run with the corresponding specifics the reader is referred to the NLR technical report [34].

4.4.1 Overall flow visualization

Field of View A (FOV-A) includes the rod and part of the airfoil. It gives an overall visualization of the vortex wake development and interaction with the airfoil. The field of view has dimensions of 18×18 cm^2 and the velocity measurement was performed with a spatial resolution of 1.4 $mm/vector$ (1.4 % chord), an overlap factor of 75% and an integration window size of 31×31 px^2 . The following results refer to the configuration of RUN 7 of the NLR technical report [34]: Field of View = FOV-A, velocity = 10 m/s , cylinder diameter = 6 mm and distance rod-airfoil = 8.3 cm . Figure 4.9 (left) is a PIV recorded particle image before processing whereas Figure 4.9 (right) shows the corresponding evaluated instantaneous velocity field. The rod and the airfoil sections are indicated by black surfaces. The velocity measurement was not available in the patched regions because the flow could not be illumi-

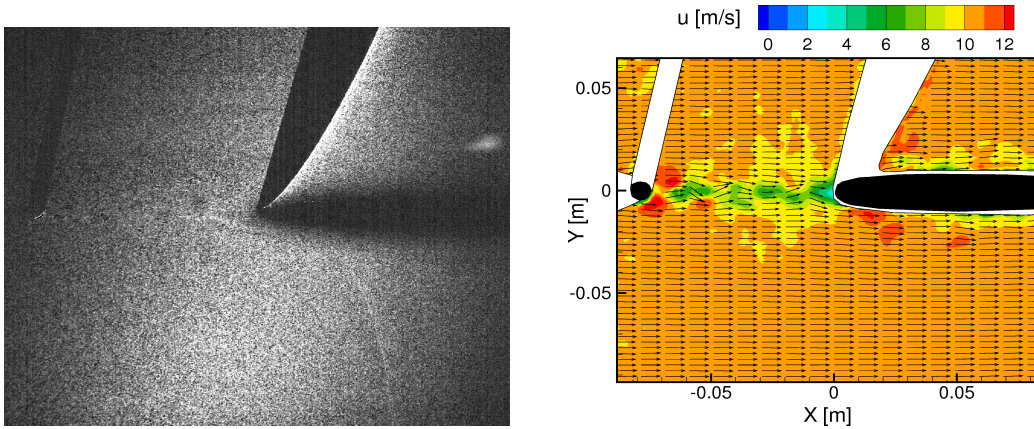


Figure 4.9: Raw PIV image (left), velocity vectors and contours of instantaneous horizontal velocity (right)

nated at this location. The origin of the reference frame has been chosen to coincide with the airfoil leading edge. The flow velocity increases along the sides of the cylinder and around the airfoil leading edge. The cylinder wake is visualized as a region of lower velocity. The instantaneous velocity vectors indicate a sinuous pattern for the instantaneous streamlines. In Figure 4.10 the time evolution of the vorticity field is shown.

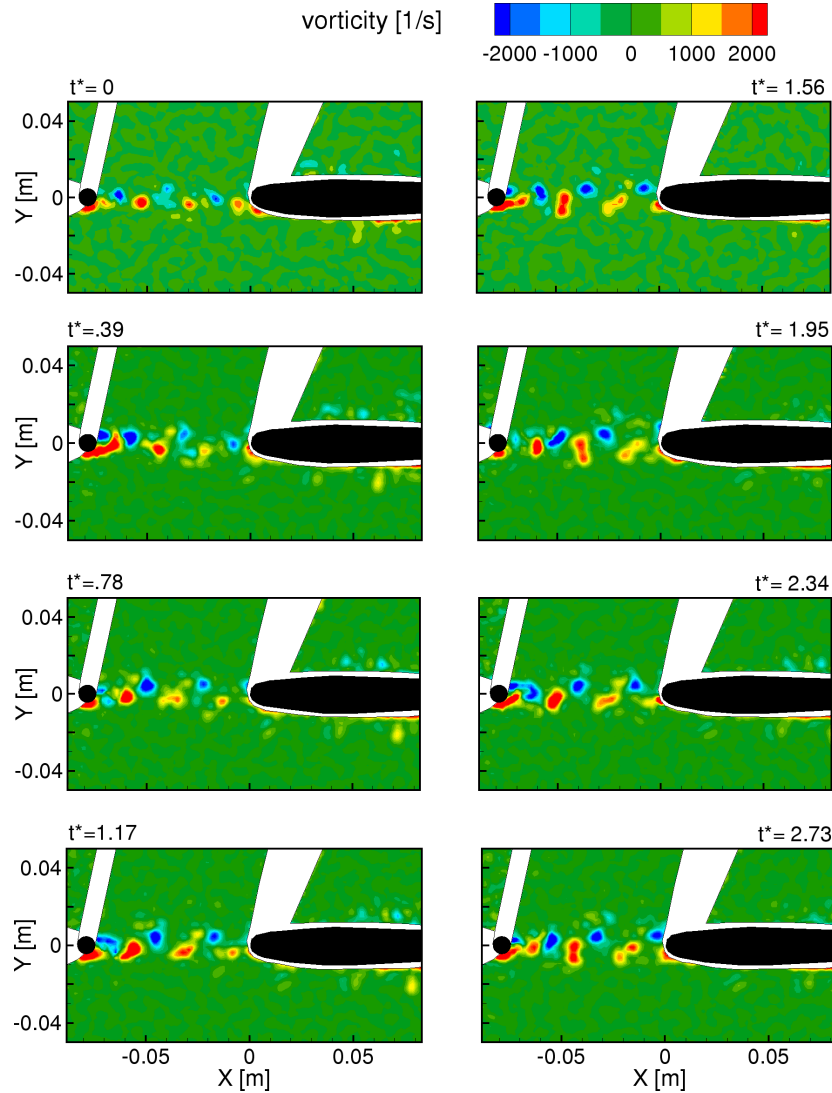


Figure 4.10: Vorticity field time evolution. Recordings are separated in time by roughly 40 % of the shedding period; Sequence order: top-bottom left column-top bottom right column for increasing t^* ; $V = 10 \text{ m/s}$, $d = 6 \text{ mm}$

The sequence of instantaneous snapshots of vorticity in Figure 4.10 show the presence of alternating vortices in the cylinder wake. $t^* = t/T_{shed}$ is the recording time normalized with respect to the shedding period. Red (counter-clockwise vorticity) and blue (clockwise vorticity) blobs indicate the counter-rotating vortices. Vortices are shed by the cylinder at a rate of 350 Hz and are conveyed with a mean spacing of 2.5 cm and traveling with a velocity of approximately 7 m/s (70% of the free stream velocity). The peak vorticity measured in this configuration is certainly underestimated due to insufficient spatial resolution and therefore, the value of 2000 s^{-1} should only be taken as a reference value. It is however, in good agreement with the reference vorticity obtained from dimensional analysis $\omega_{ref} = V_{\infty}/d = 1666 \text{ Hz}$. The vorticity significantly decays downstream of the cylinder due to three-dimensional effects acting early at vortex formation as well as later due to interaction between

neighboring vortices. As a result one can observe that the vortical structures loose coherence while approaching the airfoil. Finally, when the vortices impact on the airfoil LE they are rapidly displaced along the airfoil contour, which causes further degeneration.

4.4.2 Flow visualization around the airfoil

The FOV-2CAM view allows the visualization of the full flow field around the airfoil. Vectors have a spacing of $0.68 \text{ mm}/\text{vector}$ (0.7% chord) and the time resolution is $5.4 \text{ samples}/\text{shedding period}$ ($3.7\text{e-}4 \text{ s}$ per sample). An overlap of 75% for the correlation windows and final window size of $31 \times 31 \text{ px}^2$ were used. The camera views overlap by 9 mm as shown in the sketch of Figure 4.12. The simultaneous images from the two cameras have been merged into a single image before PIV processing. The composed images have dimensions of $1939 \times 1024 \text{ px}^2$, corresponding to a field of view of $16.39 \times 8.3 \text{ cm}^2$. The velocity fields are calculated in the configuration of RUN 32 of the NLR technical report [34]: Field of View = FOV-2CAM, velocity = 15 m/s , cylinder diameter = 6 mm and distance rod-airfoil = 10.2 cm . The PIV

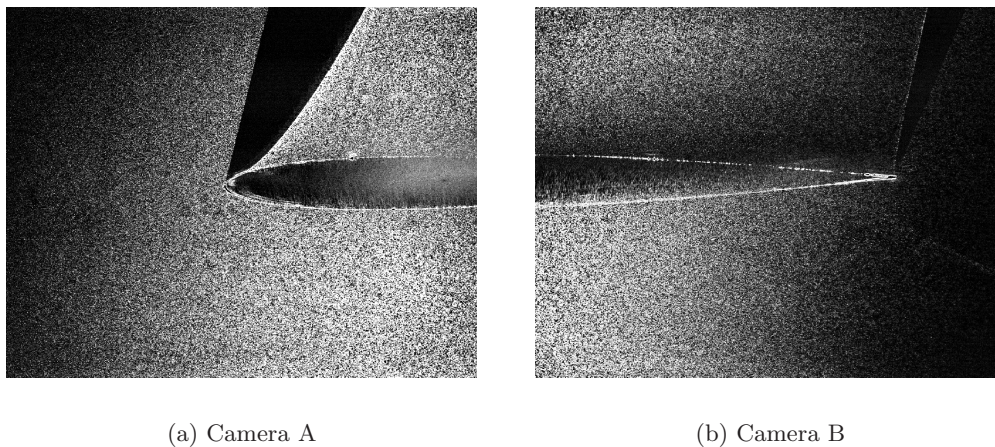


Figure 4.11: Raw PIV images for the 2 cameras

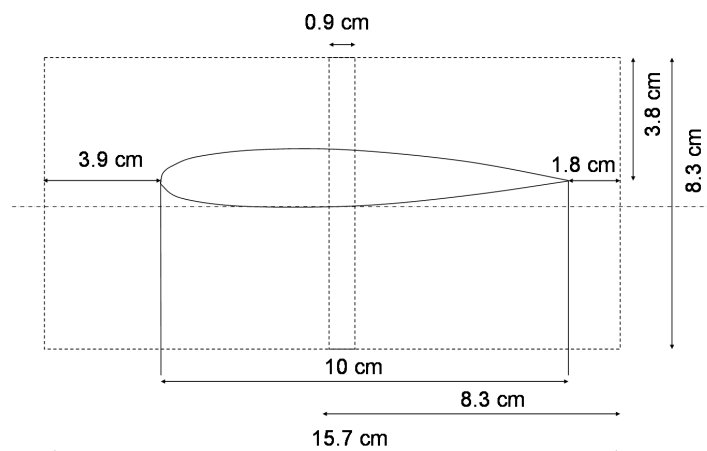


Figure 4.12: Two cameras (2CAM) field of view. The dashed lines show the single camera views

measurement parameters are summarized in Table 4.3.

Table 4.3: PIV measurement parameters ($V_\infty = 15 \text{ m/s}$ $D_{rod} = 6 \text{ mm}$)

Seeding material	Smoke particles $\approx 1\mu\text{m}$ diameter
Illumination	Quantronix Nd-YLF 2x12 mJ @ 2700 Hz
Recording device	2 x Photron Fast CAM SA1 CMOS cameras 12-bit (1024x1024 pixels, 20 μm pixel pitch)
Recording method	double frame/single exposure
Recording lens	$f = 105 \text{ mm}$, $f_\# = 2.8$
Operational frequency	2700 Hz double-pulsed mode
Combined sensor size	1939 x 1024 px (FOV 164 x 83 mm^2)
Pulse separation	50 μs
Space resolution	0.68 mm/vector (0.7 % chord)
Time resolution	≈ 5 samples/shedding period

The average flow velocity obtained from an ensemble of 1000 recordings corresponding to 185 shedding cycles is shown in Figure 4.13. The streamwise velocity component plotted in Figure 4.13-top shows a velocity deficit downstream of the cylinder. The cylinder wake appears to further expand due to the interaction with the airfoil upstream of the TE. A slight flow acceleration is visible around 30 % chord and the growth of a rather thick wake occurs downstream of the TE. The development of the airfoil boundary layer cannot be measured in the present configuration due to limits in the spatial resolution of the PIV measurements. The contours of vertical velocity component and streamlines in the bottom of Figure 4.13 illustrate a strong flow deflection at the LE and a weaker one at the TE.

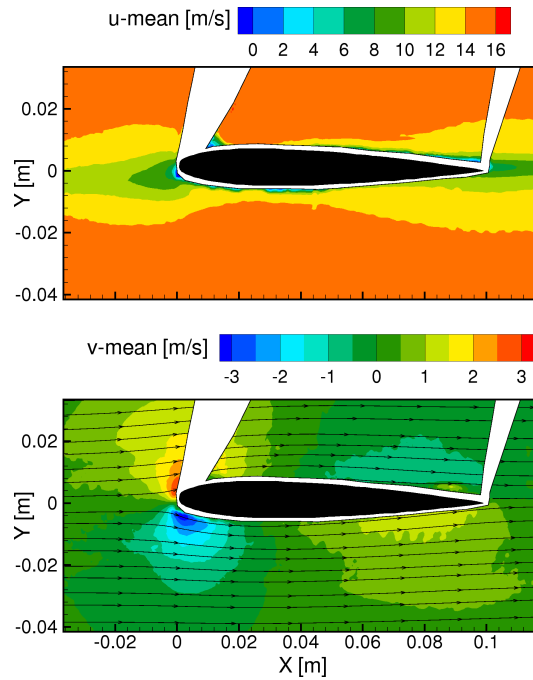


Figure 4.13: Mean velocity field. Contours of the horizontal velocity component (top). Vertical component and streamlines (bottom); $V=15 \text{ m/s}$, $d = 6 \text{ mm}$, distance rod-airfoil = 10.2 cm

The dynamical behavior of the Karman wake interaction with the airfoil is described in Figure 4.14 by a sequence of instantaneous velocity fields separated by $2\Delta t = 740\mu\text{s}$ (0.37 shedding cycle T_{shed}) in which Δt indicates the image acquisition time $\Delta t = 1/2700\text{s}$.

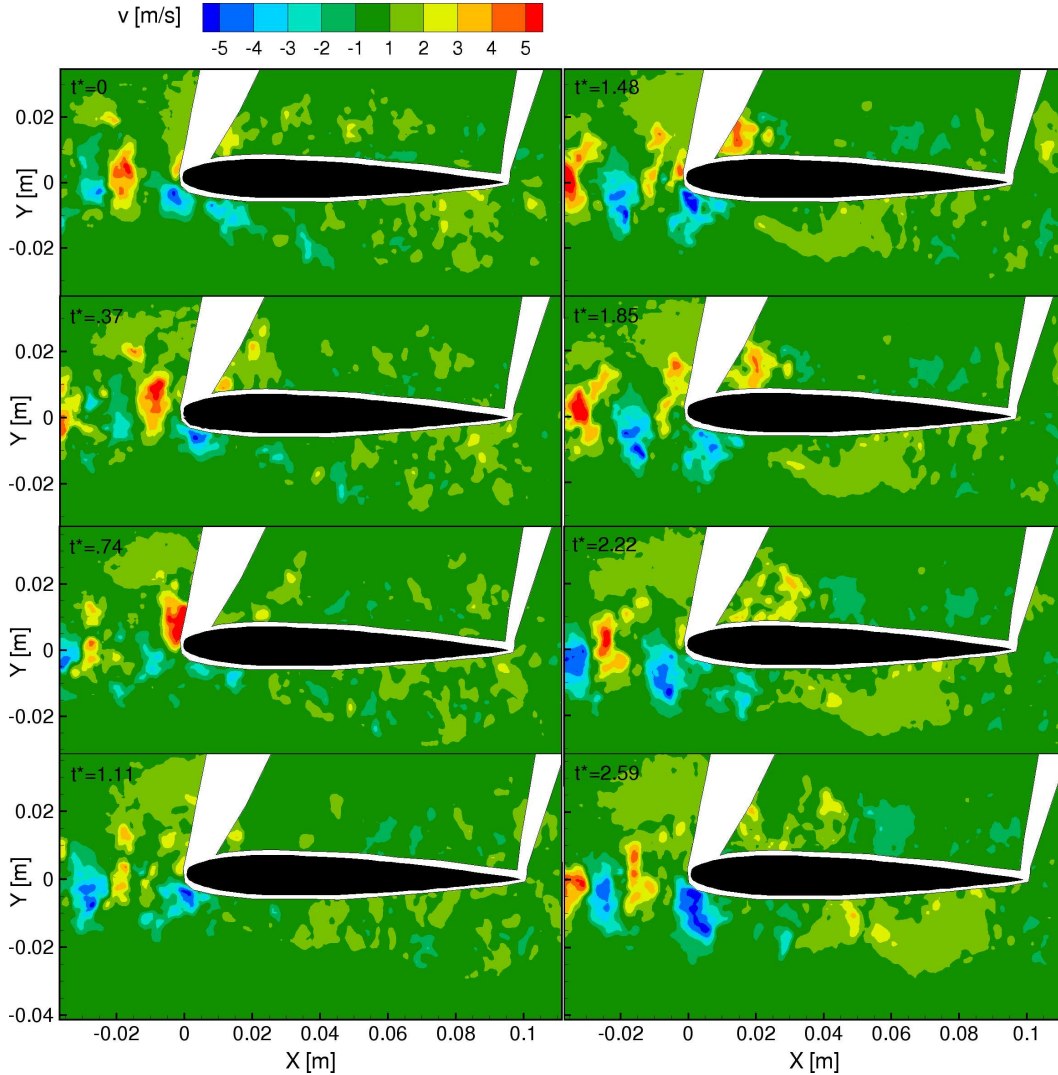


Figure 4.14: Time evolution of the vertical velocity components. t^* is the recording separation time normalized with respect to the shedding time. Sequence order: (I-IV top-bottom left column, V-VIII top-bottom right column)

The vortex street impinging on the airfoil LE is visualized by the contours of vertical velocity component, which exhibits patches of positive and negative values. The vortices however appear significantly less coherent than in the previous case (FOV-A) as a result of the higher resolution of the measurement and the higher flow speed. It is well known that the Karman vortices are composed of smaller structures originating from the instability of the shear layer separating from the cylinder surface. These structures self organize forming a large rotating structure (see reference by Williamson in [55]). Despite the three-dimensional degeneration of the vortices in the Karman wake a clear periodicity is observed just upstream of the LE. Close alternating upward (red) followed by a downward (blue) velocity indicate a clockwise rotating vortex. The vertical velocity fluctuations in the Karman vortices approaching the LE have a magnitude of approximately 4 m/s ($27\% V_\infty$), whereas after the interaction such fluctuation levels are shown to decrease to less than 15% with respect to the free-stream

velocity. The interaction may be described as follows: counter-clockwise rotating vortices approaching the LE progressively shift towards the lower side of the wake axis. Conversely clockwise rotating vortices shift towards the upper side. By approaching the LE the vortex is accelerated towards one of the two sides. At the interaction with the leading edge the larger vortical structures break down into smaller ones which convect along the airfoil sides. As the flow is accelerated along the first 20% of the airfoil chord the vortices undergo a prominent loss of coherence.

The velocity pattern does not show presence of any Karman shedding in the region behind the trailing edge, as would be expected for this airfoil without upstream rod at zero incidence (see [12]). This result is confirmed by the acoustic measurements in [34], where the TE tonal noise disappears when the rod is placed in front of the airfoil. Such behavior may be justified by the increased turbulence level in the rod wake, which prohibits the formation of a thin laminar separation bubble at the TE, necessary for the generation of the vortices responsible for the noise emission.

Correlation coefficients of the vertical and horizontal velocity components were calculated over 5 blocks of 530 ensembles each, spaced by $\Delta t = 370\mu s$. The correlation period has been estimated for three different points, as indicated in Figure 4.15. Point A in the cylinder wake, point B outside the direct wake and point C on the lower side of the airfoil at 40 % chord.

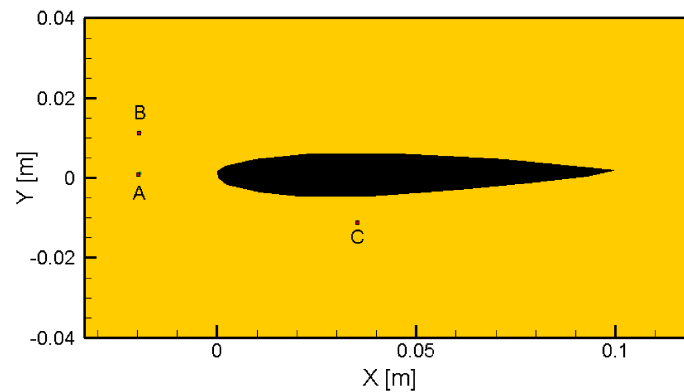


Figure 4.15: Points for correlation coefficients estimation: A in the cylinder wake, B outside the wake, C on airfoil lower side at 40 % chord

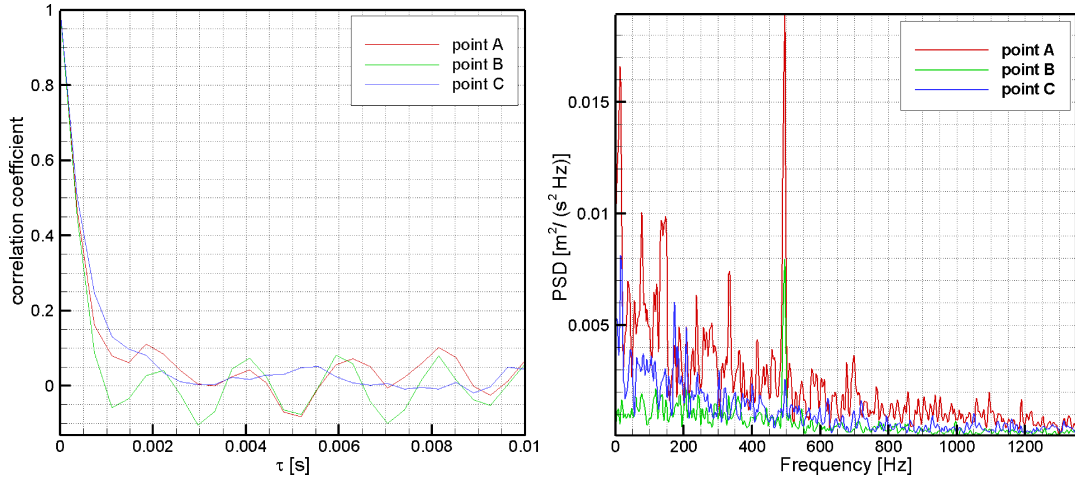


Figure 4.16: Correlation coefficient (left) and power spectral density (right) of the horizontal velocity component at check points: A, B and C

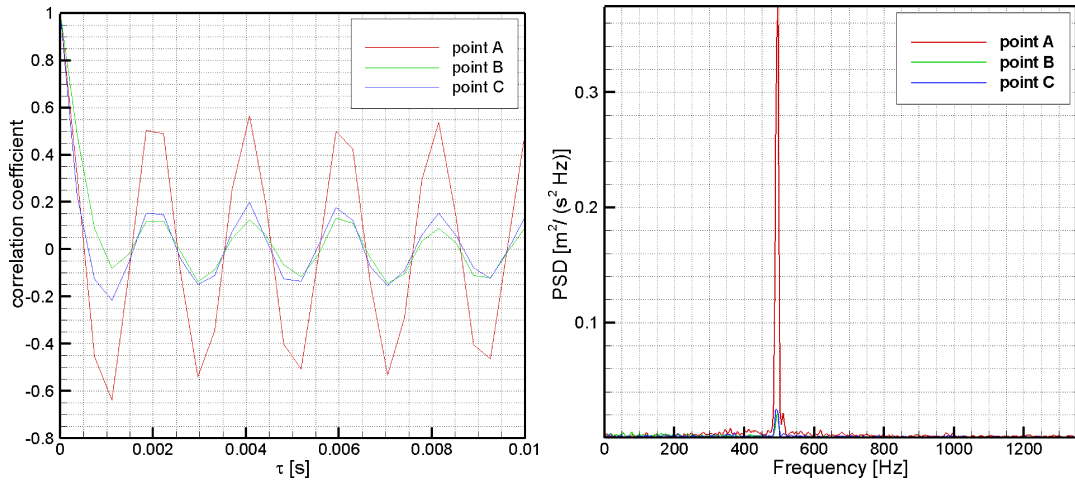


Figure 4.17: Correlation coefficient (left) and power spectral density (right) of the vertical velocity component at check points: A, B and C

The normalized time correlation of the vertical Figure 4.16 (left) and vertical Figure 4.17 (right) velocity components show an identical pattern. Point A has the highest correlation level. The amplitude of the correlation in point B, slightly outside the wake, is reduced by a factor 6 but still features the same periodic behavior as point A. The velocity fluctuations loose coherence after interaction with the airfoil as indicated by autocorrelation of the signal at point C.

In Figure 4.18 the source plot of the rod-airfoil configuration at $V=15 \text{ m/s}$ is shown. The position of local acoustic maxima confirms that most of the noise generation in a rod-airfoil configuration is effectively caused the airfoil. The maximum noise emission of about 78 dB occurs around 500 Hz and remarkably, appears to be shifted towards the airfoil trailing edge region as opposed to the expected leading edge region [29]. The causes of this have been mainly ascribed to the slight angle of incidence of the airfoil with respect to the free-stream direction, also revealed by the mean velocity contours in Figure 4.13 and to the dipolar nature

of the airfoil emission not revealable by the array. Interference with the noise emitted by the rod could also have contributed to the misalignment. For higher frequencies the main source location is found at the center of the airfoil. From 3000 Hz the interaction of the model support with the tunnel shear layer becomes a dominant noise source. However, the attained noise levels are far below peak level.

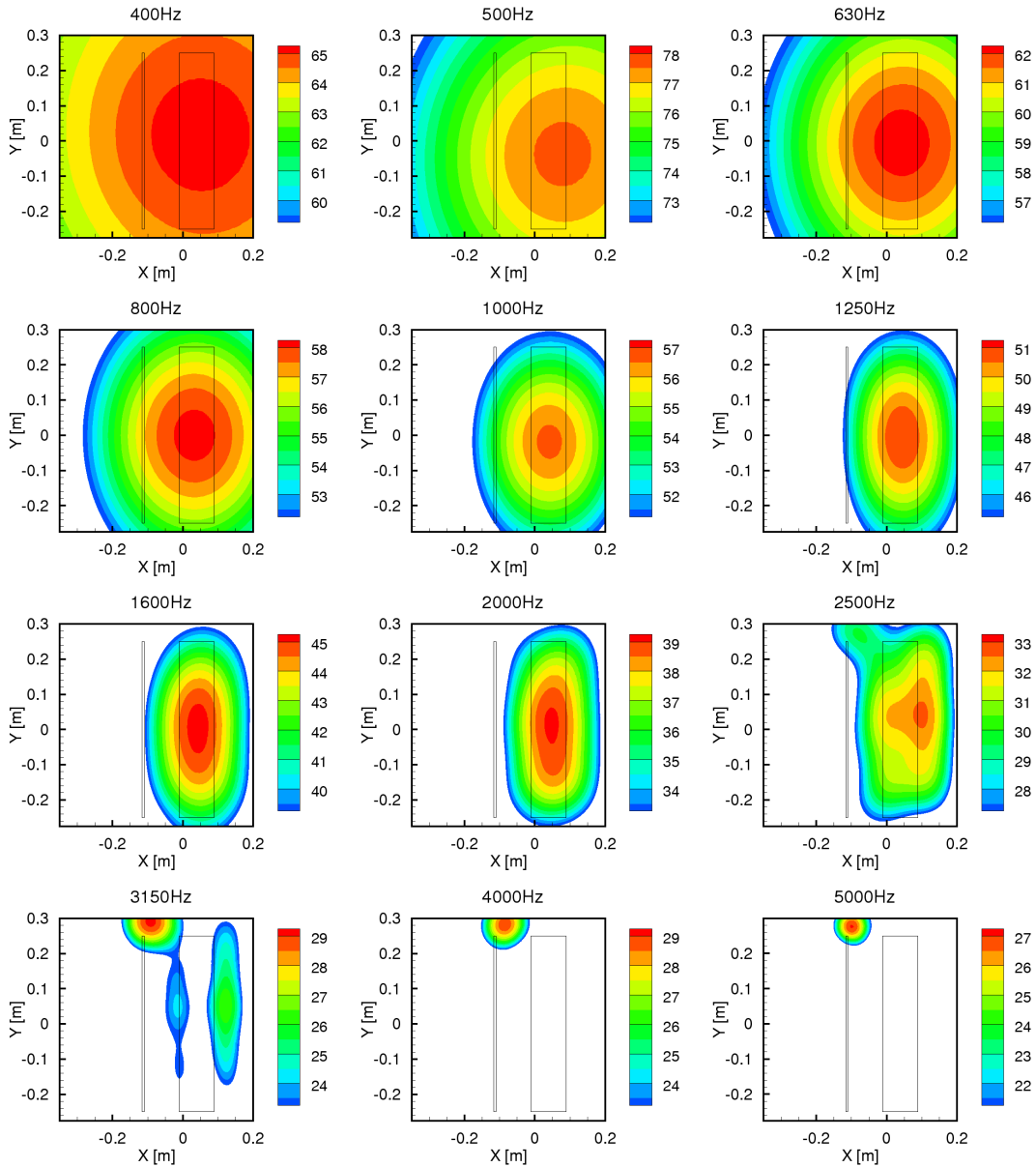


Figure 4.18: Source plot of rod-airfoil noise at $V = 15 \text{ m/s}$, cylinder diameter = 6 mm

4.4.3 Spanwise visualization

Spanwise velocity measurements have been performed in order to estimate the spanwise phase coherence of the line vortices impinging on the airfoil leading edge. The free stream velocity

and cylinder diameter are the same as for RUN 32: 15 m/s and 6 mm respectively. The distance between the rod and the airfoil is 10.8 cm . The field of view (FOV-SPAN) is 13.3 X 13.3 cm^2 wide and allows a space resolution of 1.31 $mm/vector$ (1.3 % chord) with an overlap of 75% and integration window size of 31x31 px^2 . Time resolution is the maximum attainable: 1/2700 s . The figures refer to RUN 42 of the PIV test matrix in [34]. The

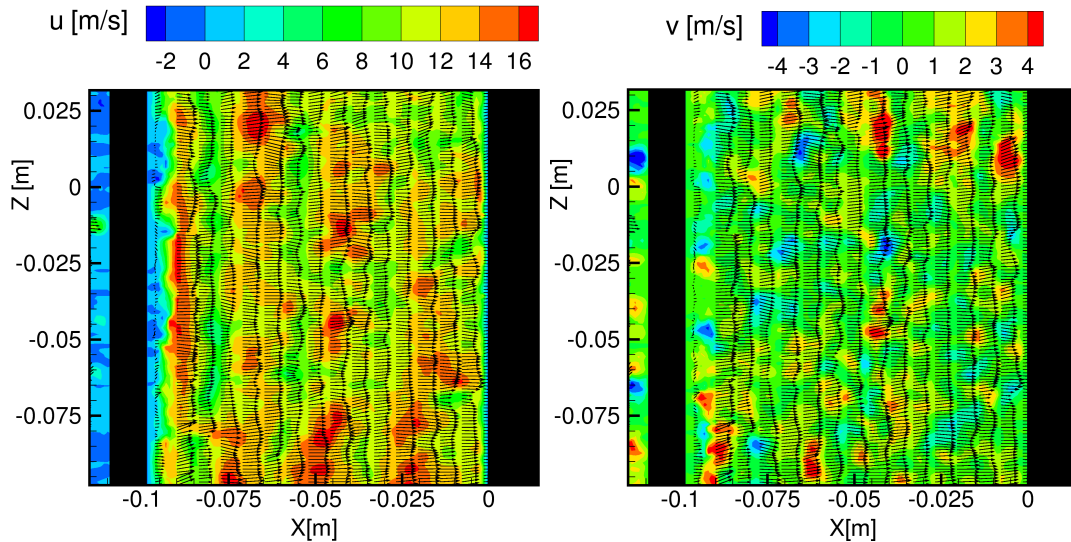


Figure 4.19: Contours of the instantaneous horizontal (left) and vertical (right) velocity components

cylinder and the airfoil are denoted by a black fill. The vertical velocity corresponds to the out of plane motion of the field of view FOV-2CAM. Its maximum value is about 25 % of the free stream velocity. The general flow motion in the cylinder wake is shown to be three dimensional. In the horizontal velocity contour spanwise coherent structures can be detected. The vertical velocity contour features alternating upward and downward displacement spots that increase in dimensions and deform while approaching the airfoil. The order of magnitude is comparable with the in-plane vertical velocity as seen in Figure 4.14. To emphasize span wise coherence a sequence of the horizontal velocity is shown in Figure 4.20. This figure gives a visualization of the phase coherence of the vortex shedding along the span wise direction. The horizontal velocity contour indicates the presence of correlated structures in the spanwise plane. The images are phase locked at consecutive shedding periods in the limits of the given time resolution of the PIV recording. The red stripes of iso-velocity represent vortex lines at a fix phase angle. These appear to be non parallel to the cylinder axis. It is known from Williamson [55] and Casalino [10] that even at low Reynolds numbers a circular cylinder sheds vortices at discrete angles with respect to the span axis because of the indirect effect of the extremities. The shedding assumes a tilde-like shape of opposite angles with respect to the mid-span section, partially visible in Figure 4.20. The inclination of the in-phase velocity lines increases as they are conveyed downstream toward the airfoil.

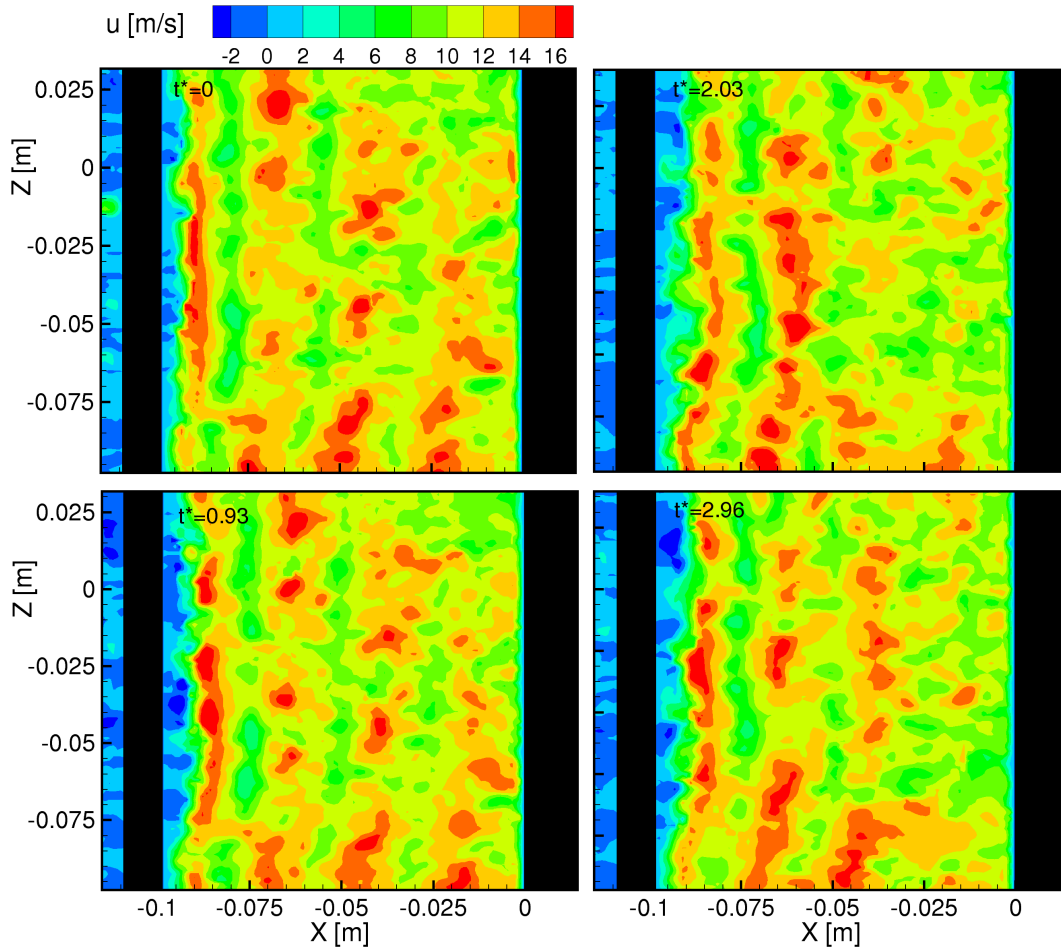


Figure 4.20: Time sequence of the horizontal velocity along the spanwise direction at normalized times t^*

4.5 Discussion of the results of the experimental campaign

Combined acoustic and PIV measurements were performed on a rod-airfoil configuration for three different free-stream velocities of respectively: 10, 15 and 20 m/s .

Preliminary acoustic measurements, conducted with eight in-line microphones, showed that a distance of 1.25 m from the airfoil was sufficiently far to be considered in the geometric far field characterized by an acoustic pressure decay inversely proportional to the first power of the distance. When the airfoil is in the Karman wake of the rod, the main process of noise generation is the impingement on the airfoil of the vortices released by the rod. The frequency of the recorded sound coincided with the peak frequency of the horizontal and vertical velocity spectra in front of the airfoil. This confirmed the hypothesis that the sound emission in the rod-airfoil configuration is mainly due to the large vortical structures in the flow upstream of the airfoil.

The presence of the airfoil reduced the peak frequency with respect to the rod alone case, as also experienced by Casalino and Jacob for investigations over the same configuration [10, 29]. A possible explanation can rely on a hydrodynamic-acoustic interference of the airfoil on the

rod shedding mechanism itself. The noise level increased of more than 10 dB and the sound spectrum broadened around the peak in presence of the airfoil.

The contours of the vertical velocity in the spanwise visualization showed that the flow in the cylinder wake is only nominally 2-dimensional. The amplitude of the velocity component in the span direction had peaks of 30 % of the free-stream velocity. This out of plane component has not been accounted for by the planar PIV computation technique. Phase-locked sequence of horizontal velocity contours allowed for the detection of a non uniform shedding phase distribution along the rod span. Iso-velocity lines assumed a tilde-like shape which further deformed downstream towards the airfoil. The latter phenomenon is described by Williamson in [55].

The velocity fields obtained from field of view FOV-2CAM, for free stream velocities of 10 and 15 m/s , have been further implemented as source terms in an aeroacoustic code together with the planar pressure field from the PPI algorithm in order to numerically predict the noise level at specific far-field locations and to compare it with the one measured by the microphones.

Data reduction techniques

The following chapter offers a general overview of the procedure followed for the determination of the acoustic field starting from the results of PIV experiment. First the Poisson based method for pressure field deduction is presented. Then follows the description of the methodologies and assumptions for evaluation of the acoustic sources. The algorithm developed by the author for implementation of the aeroacoustic analogies is then described in both discrete and integral formulation.

5.1 Planar Pressure Imaging

The Planar Pressure Imaging (PPI) is a method for the computation of local static pressure from velocity PIV data. The knowledge of local pressure around a body immersed in the fluid is of crucial importance within aerodynamic studies since it allows for the determination of relevant aerodynamics quantities such as integral aerodynamic loads. Integral determination of the aerodynamic loads on a square section cylinder by means of time resolved pressure and velocity data has been performed by Kurtulus *et al* (2007)[31].

The pressure field from 2D-PIV data has been calculated by van Oudhousden *et al.*(2007) [38] and A. Ashok (2008) based on the direct spatial integration of the Navier-Stockes equations. This method when applied to the present experiment has revealed to be particularly sensitive to local discontinuities of the velocity gradients encountered during the “space marching”. The strategy followed in this work for the pressure determination is based on integration of the planar components of the Poisson equation for the pressure. The algorithm has been developed by R. de Kat for pressure determination around a square section cylinder by means of time-resolved PIV [15, 53].

The 2D Poisson equation is obtained by applying the in-plane divergence operator to the 2D Navier-Stockes equations

$$\frac{\partial^2 p}{\partial x^2} + \frac{\partial^2 p}{\partial y^2} = f, \quad (5.1)$$

where, for an incompressible 2D flow, the vector f is defined as:

$$f = -\rho \left[\left(\frac{\partial u}{\partial x} \right)^2 + 2 \frac{\partial u}{\partial y} \frac{\partial v}{\partial x} + \left(\frac{\partial v}{\partial y} \right)^2 \right]. \quad (5.2)$$

For an incompressible three-dimensional flow the in-plane divergence of the velocity does not vanish

$$\frac{\partial u}{\partial x} + \frac{\partial v}{\partial y} = \text{div}_{xy} = -\frac{\partial w}{\partial z} \neq 0, \quad (5.3)$$

hence the term $\frac{\partial u}{\partial x} + \frac{\partial v}{\partial y}$ has to be retained and in-plane component of the Poisson equation then becomes

$$\begin{aligned} \frac{\partial^2 p}{\partial x^2} + \frac{\partial^2 p}{\partial y^2} = & -\rho \left[\left(\frac{\partial u}{\partial x} \right)^2 + 2 \frac{\partial u}{\partial y} \frac{\partial v}{\partial x} + \left(\frac{\partial v}{\partial y} \right)^2 \right] \\ & -\rho \left[\frac{\partial \text{div}_{xy}}{\partial t} + u \frac{\partial \text{div}_{xy}}{\partial x} + v \frac{\partial \text{div}_{xy}}{\partial y} \right] + \\ & -\rho \left[\frac{\partial w}{\partial x} \frac{\partial u}{\partial z} + \frac{\partial w}{\partial y} \frac{\partial v}{\partial z} \right]. \end{aligned} \quad (5.4)$$

The first terms in square brackets are the components Poisson equation for 2D flow. The second term of equation (5.4), arising in a 3D flow, is due to convection of the planar divergence. Planar PIV only provides the in-plane quantities. The velocity components and velocity gradients in the out of plane direction have been not considered in this work. De Kat showed in [15] that neglecting these terms has minor influence on the pressure determination for a quasi-2D flow. Stereo PIV would not improve the calculation because of the missing knowledge of the out-of-plane gradients. A tomographic PIV approach would permit the determination of both out-of-plane components and gradients¹.

Boundary conditions of Dirichlet and Neumann type, for the pressure and pressure gradient respectively, have to be set at the domain boundaries and at the interface with the immersed bodies. Neumann conditions are directly provided by the Navier-Stokes equation in all the points of the domain where velocity and velocity gradients are defined. Dirichlet conditions, at least in one point, are needed as scaling reference values. In the present case the latter conditions have been derived from the steady Bernoulli relation in irrotational flow regions.

5.1.1 PPI results

The elliptic nature of the differential operator implies that the integration does not have any preferential integration path and that every discontinuity inside the domain influences the whole field. In order to preserve the solution from spurious oscillations it has been necessary to mask some regions of the domain characterized by unreliable velocity gradients. These regions correspond to:

- The shadow regions shown in Figure 4.4 are caused by refraction at interaction of the laser light with the airfoil.
- The left side of the flow field where the highest intensity three dimensional motion occurs.

In Figure 5.1 (right) these regions are denoted by a white fill. Figure 5.1 shows a sequence of instantaneous vertical velocity fields (left) and the corresponding pressure fields (right)

¹Implementation of Tomo-PIV for aeroacoustic purposes is one of the aims of the FLOVIST project [34].

at subsequent normalized time ($t^* = t/T_{shed}$, where T_{shed} indicates the shedding time). In order to highlight the unsteady behavior of the flow only the velocity and pressure temporal fluctuations over the local time average are shown, respectively

$$v_{fluct}(x, y, t) = v(x, y, t) - \langle v(x, y) \rangle,$$

and

$$p_{fluct}(x, y, t) = p(x, y, t) - \langle p(x, y) \rangle.$$

The vertical velocity fluctuations in the Karman wake approaching the LE show high degree

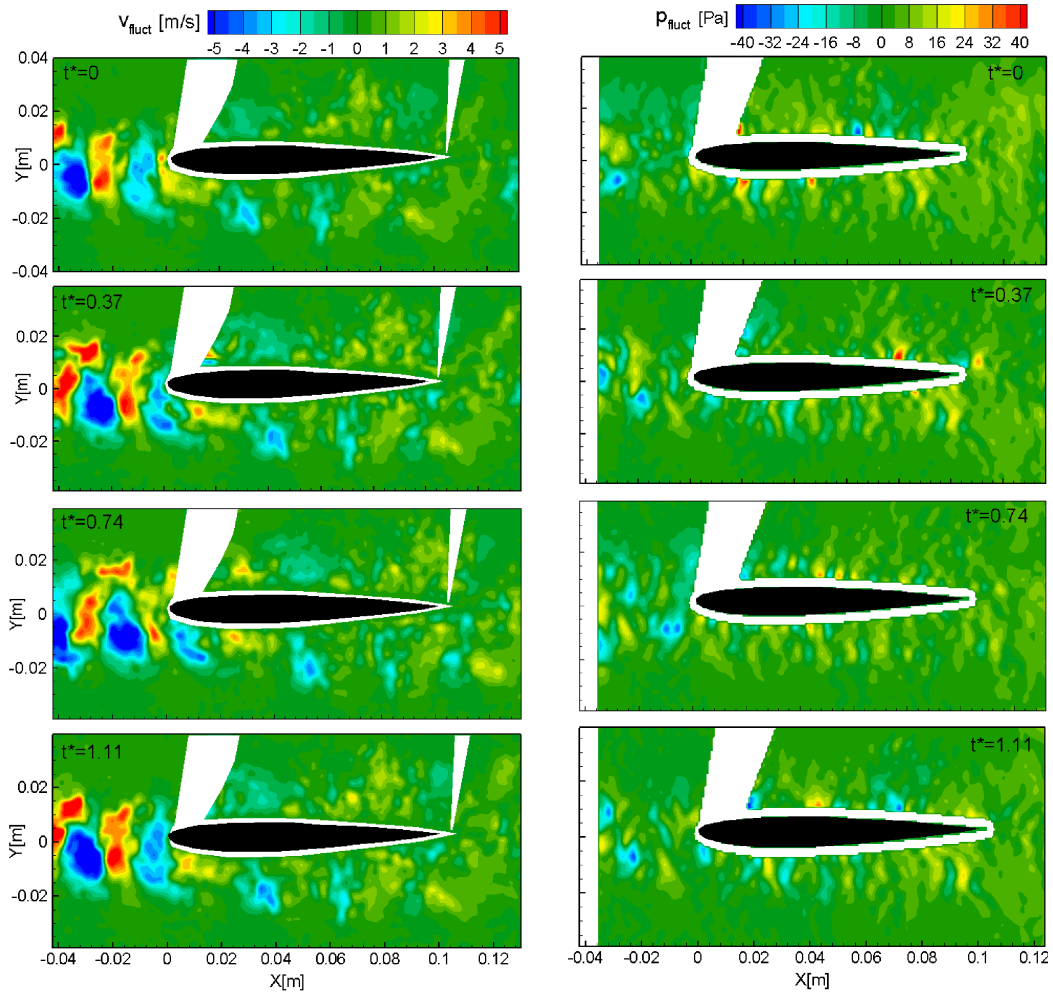


Figure 5.1: Time sequence of the instantaneous velocity fluctuations v_{fluct} and relative pressure fluctuations p_{fluct} at normalized times t^* . $V_\infty = 15 \text{ m/s}$, $D_{rod} = 6 \text{ mm}$.

of coherence until interaction with the LE. During the interaction larger vortical structures break down into smaller ones which convect along the airfoil sides. As the flow is accelerated along the first 20% of the airfoil chord the vortices undergo a prominent loss of coherence.

The pressure fluctuations upstream of the airfoil exhibit a less clear pattern. Figure 5.1 (right), however, reveals a still distinguishable convection process of the local pressure fluctuations

towards the LE and coherence loss at interaction with the airfoil. The points embedded by upward (red) and downward (right) velocity bulges in Figure 5.1 (right) are indicative of a coherent vortex and correspond to minima of the local pressure, as indicated by the low pressure (blue) regions of Figure 5.1 (right).

The time history of the fluctuation of the static pressure around the atmospheric pressure $\Delta p = p - p_0$ has been evaluated in point A, indicated in Figure 4.15 of Chapter 4, and is shown in Figure 5.2.

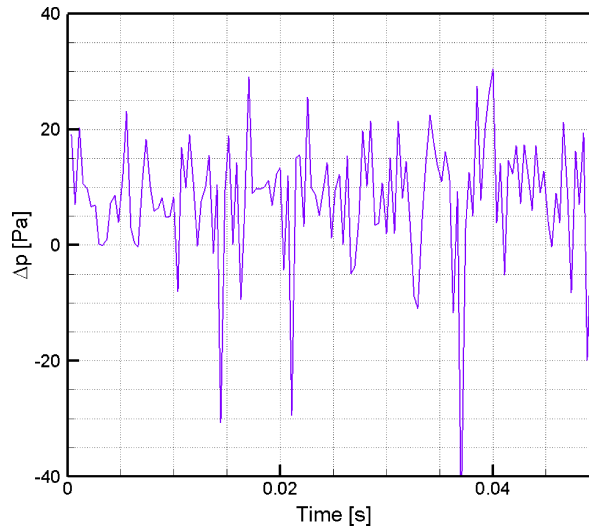


Figure 5.2: Time history of the static pressure fluctuations around the reference pressure p_0 evaluated at point A

The causes of the intermittency of the pressure signal have at present been ascribed to the following factors:

- Non sufficient time resolution of the measured velocity field
- Spurious velocity gradients at interface with masked regions
- 3D effects not accounted for by the pressure algorithm, particularly relevant inside the cylinder wake

The increase of the spatial and temporal resolution of the velocity field would certainly improve the evaluation of the pressure signal and, consequently, the accuracy of the aeroacoustic prediction. This will be an essential requirement for future experiments inside the FLOVIST project.

Autocorrelation and power spectrum of the fluctuating pressure have been calculated on the three check points A, B and C, indicated in Figure 4.15. Periodicity of the pressure signal at about 500 Hz, corresponding to the vortex shedding frequency, is still revealed by the power spectral density of the pressure signal in Figure 5.3 (right), for all the check points.

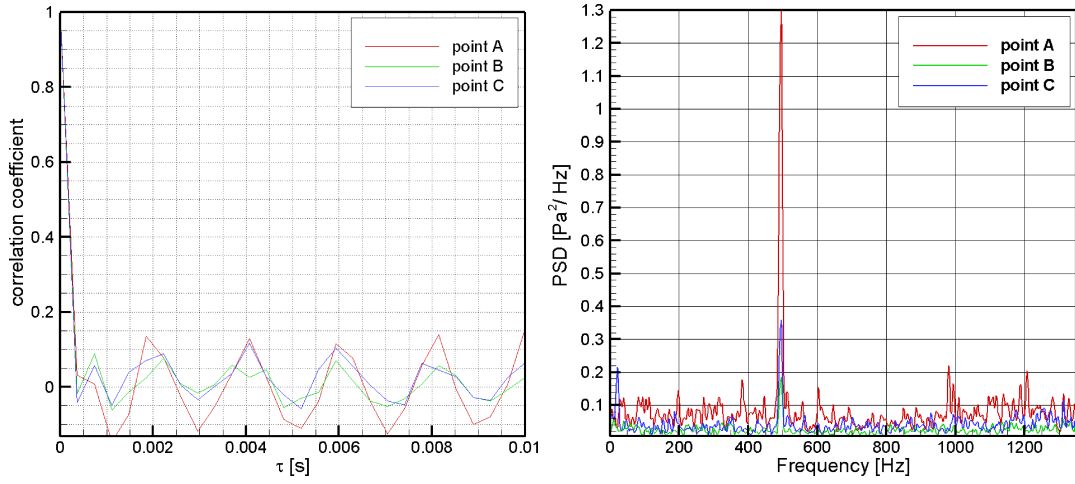


Figure 5.3: $\Delta p = p - p_0$ correlation coefficient (left) and power spectral density (right) at check points: A, B and C

The static pressure exhibits lower correlation coefficients with respect to the velocity components of Figure 4.16 and 4.17. Point A, in the cylinder wake, still features a slightly higher correlation peak with respect to Point B and Point C although the magnitude of the correlation coefficient is reduced by a factor 3 with respect to the horizontal velocity component and a factor 1.5 with respect to the vertical velocity component.

The convection of the instantaneous pressure fluctuation along the lower side of the control surface S , approximating the physical airfoil surface, is shown in Figure 5.4. The x-axis corresponds to the local coordinate of the lower airfoil surface from a to b , indicated in Figure 5.8 (left), and the y-axis to a generic observation time interval in physical units.

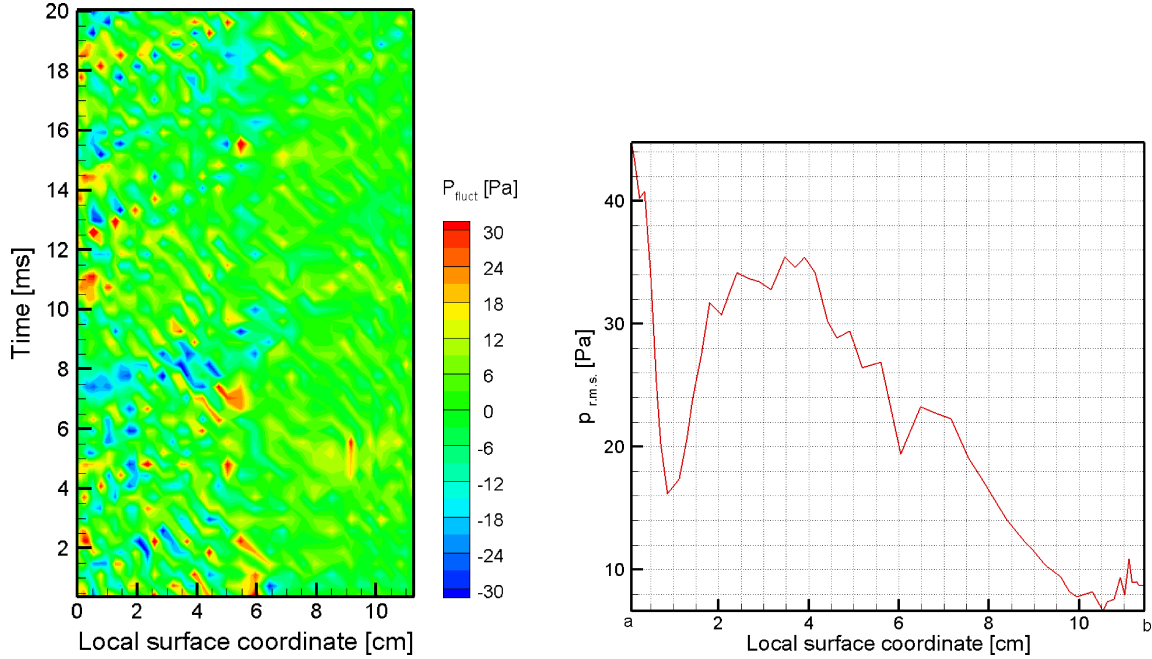


Figure 5.4: Time evolution of the pressure fluctuations (left) and root mean square value of the pressure (right) on the lower side of integration surface (from a to b)

The diagonal stripes are representative of convection of the pressure fluctuation along the lower side of the control surface. The stripes are spaced in time-wise direction by about 2 m/s , which approximatively corresponds to a shedding cycle. The discontinuous feature of the stripes is due to the scattering of the pressure signal.

Figure 5.4 (right) shows the root-mean square of the pressure fluctuation Δp along the local coordinate s between point a and point b and gives an indication of the average spatial distribution of the pressure along the control surface.

5.2 Aeroacoustic computation

The main purpose of the present investigation is the computation of the acoustic pressure signal in the acoustic far-field, based on the experimental flow data, and its comparison with the measurements of the four far-field microphones indicated in the experimental setup section of Chapter 4.

The analytical formulation of the aeroacoustic problem is represented by equation (2.52), renamed in Chapter 2 as Curle/FW-H formulation. At the low Mach number of the present experiment ($M < 0.05$), relatively high Reynolds number (over 10,000 with respect to the airfoil) and far-field location for the acoustic evaluation, the following simplifying assumptions can be made:

- Quadrupolar sources represent the direct contribution of the turbulence to the overall acoustic field. By an order of magnitude estimation (see Chapter 2) it has been shown that this term scales with a power of M higher than the dipolar term. In vortex-

structure interaction problems, for sufficiently low Mach numbers, it is thus common practice to neglect the quadrupolar term in comparison to the dipolar term.

- At the distance where the evaluation of the pressure signal is performed the acoustic waves propagate as quasi-plane waves and space derivative can be replaced by time derivatives (see section 2.25).
- In low Mach numbers flows pressure variations due to elasticity of the fluid medium (usually defined as “compressibility effects”) are much weaker than pressure variations due to hydrodynamic fluid motion and the flow in the source region can be considered to act as nearly incompressible. Constant density is assumed throughout the source region $\rho \simeq \rho_0$.
- For compact integration surfaces, i.e. for a surface small compared to the wavelength of the emitted sound, in open configuration, the pressure fluctuation of acoustic nature acting on the integration surface, due to acoustic propagation inside the source region, give a negligible contribution to the total radiation.
- Because of the relatively high Reynolds number viscous stresses are neglected.

Exploitation of the previous assumptions results in the simplified Curle/FW-H equation

$$\begin{aligned}
 p'(\mathbf{x}, t) &= -\frac{x_j}{4\pi c_0 |\mathbf{x}|} \frac{\partial}{\partial t} \int_{\partial V_y} \frac{\rho_0 v_i v_j + p' \delta_{ij}}{r} \Big|_{t=t_e} n_i dS \\
 &- \frac{1}{4\pi} \frac{\partial}{\partial t} \int_{\partial V_y} \frac{\rho_0 v_i}{r} \Big|_{t=t_e} n_i dS,
 \end{aligned} \tag{5.5}$$

where V_y indicates the control volume and ∂V_y its boundary.

When the control surface is located close enough to the physical airfoil surface the assumption of no-cross flow at the surface is made, leading to the standard Curle’s analogy formulation, herein called *non-permeable Curle/FW-H*. When the control surface is moved away from the airfoil the velocity terms have to be retained in the source evaluation and a permeable Ffowcs Williams-Hawkings formulation, here referred to as *permeable Curle/FW-H*, is adopted. The characteristics of two approaches are described in the following sections.

5.2.1 Non-permeable Curle/FW-H

When a *non-permeable* Curle’s integration surface is used for the source evaluation, the velocity components at the control surface drop out and the pressure fluctuations constitute the only forcing term of the radiated acoustic field. The standard Curle’s analogy requires to set the control surface on the physical surface of the immersed body. Since PIV measurement allowed only limited spatial resolution of the flow field in the proximity of the airfoil solid surface, the region immediately close to the surface has been excluded from the pressure evaluation and the control surface has been placed at a “safe” distance of 5 grid points (3.4 mm) from the airfoil. If the boundary layer thickness is much smaller than the characteristic length of the incoming vortices, Prandtl’s simplified equations for boundary layer flows can

be used and the normal gradient of the pressure, through an order of magnitude estimation, can be shown to scale as

$$\frac{\partial p}{\partial n} \propto \frac{\delta}{\lambda} \frac{(\Delta u)^2}{\lambda},$$

where δ represents the boundary layer thickness (in this case $\delta < 1mm$), λ the characteristic length of the vortices (in first approximation equal to the cylinder diameter) and Δu the vortex strength (about 30 % of the free stream velocity). For relatively big vortices, i.e. $\lambda \gg \delta$, the static pressure normal to the airfoil is about constant through the boundary layer. In the present case the assumption has been made that the pressure at the control surface coincides with the pressure at the physical airfoil surface.

The aeroacoustic problem can thus be analytically reformulated in a simpler way as

$$p'(\mathbf{x}, t) = -\frac{x_j}{4\pi c_0 |\mathbf{x}|} \frac{\partial}{\partial t} \int_{\partial V_y} \frac{p' \delta_{ij}}{r} \Big|_{t=t_e} n_i dS, \quad (5.6)$$

which indicates that only pressure variations at the control surface contribute to the acoustic pressure perceived by the listener at position \mathbf{x} . The results of this approach are shown for 10 and 15 m/s free stream velocities in Chapter 6.

5.2.2 Permeable Curle/FW-H

The contribution of the momentum and mass fluxes at the integration surface is accounted for by the use of a *permeable* control surface. The velocity components at the surface are retained and the resulting analytical formulation in far-field assumption becomes

$$p'(\mathbf{x}, t) = -\frac{x_j}{4\pi c_0 |\mathbf{x}|} \frac{\partial}{\partial t} \int_{\partial V_y} \frac{\rho_0 v_i v_j + p' \delta_{ij}}{r} \Big|_{t=t_e} n_i dS - \frac{1}{4\pi} \frac{\partial}{\partial t} \int_{\partial V_y} \frac{\rho_0 v_i}{r} \Big|_{t=t_e} n_i dS. \quad (5.7)$$

The 2nd surface integral source term

$$TN = -\frac{1}{4\pi} \frac{\partial}{\partial t} \int_{\partial V_y} \frac{\rho_0 v_i}{r} \Big|_{t=t_e} n_i dS, \quad (5.8)$$

known as *thickness noise* or *monopole term*, represents the total mass injection into the control surface. This is particularly important in case of pulsating bodies or moving surfaces and its acoustic power, based on the same order of magnitude estimation proposed by Lighthill, scales with the fourth power of the Mach number.

If the characteristic dimension of the aeroacoustic source (body or eddy) is small, compared to the distance between source and listener, the distance between different emitting points on the source surface can be neglected and the source listener distance can be approximated as

$$r = |\mathbf{y} - \mathbf{x}| \simeq |\mathbf{x}| = R.$$

Furthermore, if the wavelength of the emitted sound is much larger than the distance between the sources it can be assumed that there is no reciprocal cancelation of the noise emitted by the sources due to emission phases shifts and a single retarded time for all the acoustic sources can be assumed. Making use of the Green's theorem, at far enough distances from the sources and in compact body assumption, the monopole term can then be rewritten as

$$TN = -\frac{\rho_0}{4\pi R} \frac{\partial}{\partial t} \int_{V_y} \frac{\partial v_i}{\partial x_i} \Big|_{t=t_e} dV, \quad (5.9)$$

where the integrand represents the in-plane components of the velocity divergence. For a purely 2D flow this term would be only generated by compressibility effects, which as already shown in Chapter 2, scale with the square of the flow Mach number. Since compressibility effects at the present Mach number are reasonably negligible, the non-zero value of the integral is attributed to the out-of-plane velocity component, not valuable in the present analysis.

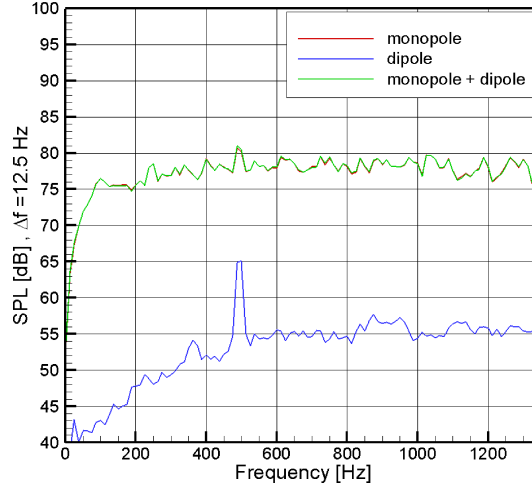


Figure 5.5: Acoustic spectra computed with and without retaining the monopole term

If the acoustic evaluation is performed retaining the monopole term, a non-physical high magnitude broadband contribution to the computed acoustic emission is revealed. The monopole term dominates the whole acoustic spectrum as shown in Figure 5.5 in comparison to the dipole term. This effect has been mainly attributed to 3D motion effects not included in the flow description. Since a proper evaluation of the monopole term was not possible in the present investigation and expecting a partial cancelation of the out-of-plane velocity component over the whole integration surface, the monopole term has been neglected in the acoustic computation.

The analytic formalism implemented in the code while using a permeable surface approach, finally reduces to

$$p'(\mathbf{x}, t) = -\frac{x_j}{4\pi c_0 |\mathbf{x}|} \frac{\partial}{\partial t} \int_{\partial V_y} \frac{\rho_0 v_i v_j + p' \delta_{ij}}{r} \Big|_{t=t_e} n_i dS, \quad (5.10)$$

which only differs from the impermeable Curle's approach by the introduction of the quadratic velocity "stresses" (in analogy to the common definition of Reynolds stresses) at the control surface, represented by the term $\rho_0 v_i v_j$.

When using a permeable integration surface formulation the pressure fluctuations p' at integration surface must account for both hydrodynamic and acoustic contributions. The acoustic wave generated in the region embedded by the surface propagate as sound into the far field and constitute the solution of the wave propagation equation to be solved. Neglecting this effect by the use of incompressible flow descriptions is in principle non correct as remarked by

Greschner *et al.* in [24]. In the present investigation pressure fluctuations and relative velocity fluctuations due to acoustic propagation could not be evaluated due to the limited spatial resolution of the PIV experiment. The hypothesis, however, has been made that for integration surfaces inside the turbulent flow region the pressure fluctuations of hydrodynamic nature dominate over pressure fluctuations due to acoustic compression of the medium and neglecting the contribution of the acoustic pressure may result only in a slight underestimation of the total acoustic pressure field.

The results of the implementation of a permeable control surface, disregarding the acoustic phenomena in the source region, are presented in Chapter 6. The use of a permeable approach relaxes the need to set the integration surface coinciding with the physical airfoil surface and could reveal particularly useful in case of experimental flow descriptions which generally become less accurate in proximity to solid walls. Future 3D flow visualizations by means of Tomographic PIV would allow the complete description of out of plane motion and a proper evaluation of the thickness noise monopolar term. Further investigations on the effect of including acoustic waves in the evaluation of the surface source terms on the total acoustic prediction are also required.

5.2.3 Compact body simplification and lift evaluation

When the acoustic pressure is evaluated at large distances from the source region equation (5.5) can be simplified as

$$\begin{aligned}
 p'(\mathbf{x}, t) &= -\frac{x_j}{4\pi c_0 R^2} \frac{\partial}{\partial t} \int_{\partial V_y} [\rho_0 v_i v_j + p' \delta_{ij}]_{t=t_e} n_i dS \\
 &\quad - \frac{1}{4\pi R} \frac{\partial}{\partial t} \int_{\partial V_y} \rho_0 v_i|_{t=t_e} n_i dS.
 \end{aligned} \tag{5.11}$$

If integration is performed on a non-permeable surface coinciding with the physical body surface, following the standard Curle's approach, the second integral and the velocity components of the first integral vanish because of non-penetrability and no-slip conditions at the wall. The first integral, in case of a compact body, reduces to equation 2.38, which can be rewritten as

$$p'(\mathbf{x}, t) = -\frac{x_j}{4c\pi R^2} \frac{\partial}{\partial t} F_j(t - \frac{R}{c}), \tag{5.12}$$

where F_i is the total aerodynamic force acting on the body [14, 25].

The aeroacoustic radiation in the case of a compact body, in agreement with Gutin's principle (see Chapter 2), can be completely computed by knowledge of the aerodynamic loads acting on the body.

The calculated values of the lift and drag forces acting on the airfoil and the relative spectra are shown in Figure 5.6.

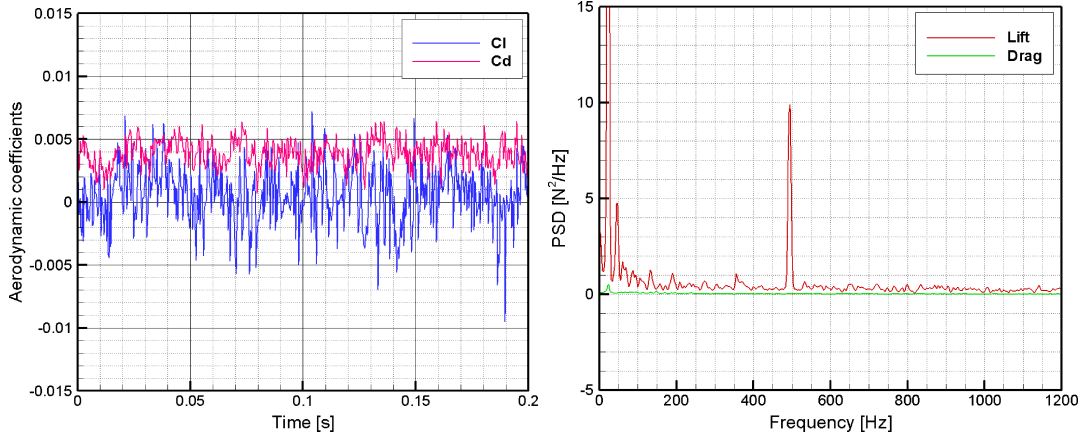


Figure 5.6: Time history of the lift and drag coefficients (left) and power spectral density of lift and drag forces (right) evaluated on surface S

In the present case the contribution of the drag force is lower than the lift contribution by a factor 6. This indicates that most of the aeroacoustic emission is due to the time-varying lift force acting on the airfoil, in direction perpendicular to to free-stream velocity. The spectrum of the drag force does not exhibit any relevant peak.

As a rule of thumb for first emission directivity predictions, if the emitting object is smaller than a quarter of wavelength of the radiated sound phase shifts between different source points can be neglected and the emitting object can be considered as a unique in-phase emitter with main directivity perpendicular to the free stream velocity [25].

An airfoil immersed in the Karman wake of an upstream body experiences a fluctuating lift force as a consequence of the variation of the velocity circulation at the surface due to the incoming vorticity. The lift force acting on the airfoil has been calculated using both the definition of lift as integral of the pressure at the body surface and using an integral formulation of the momentum equation also adopted by Kurtulus *et al.* in [31].

The horizontal and vertical components of the momentum equation in conservative form, integrated over the control volume VL of Figure 5.7, surrounding the airfoil, can be rewritten as

$$\begin{aligned} \rho_0 \int_{VL} \frac{\partial u}{\partial t} dV + \rho_0 \int_{VL} \left(\frac{\partial u^2}{\partial x} + \frac{\partial uv}{\partial y} + \frac{1}{\rho_0} \frac{\partial p}{\partial x} \right) dV &= -D(t), \\ \rho_0 \int_{VL} \frac{\partial v}{\partial t} dV + \rho_0 \int_{VL} \left(\frac{\partial uv}{\partial x} + \frac{\partial v^2}{\partial y} + \frac{1}{\rho_0} \frac{\partial p}{\partial y} \right) dV &= -L(t), \end{aligned} \quad (5.13)$$

where viscous stresses and compressibility have been neglected and the terms $D(t)$ and $L(t)$ indicate the time varying reactive forces per unit span exerted by the airfoil onto the flow. A sketch of a generic integration volume and the normals to the surface are shown in Figure 5.7.

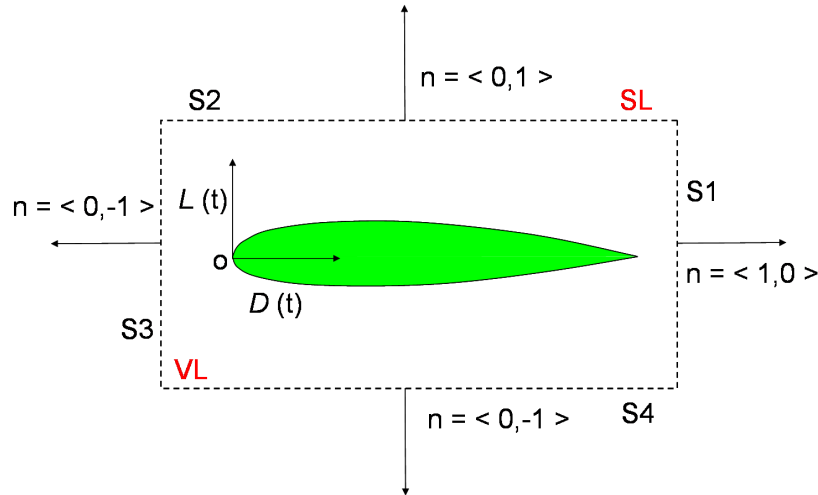


Figure 5.7: Control volume for evaluation of the aerodynamic forces

The lift force has been calculated both as integral vertical projection of the static pressure at surface S (Figure 5.8 (left)) and exploiting the integral momentum conservation on three different control volumes bounded by the surfaces $SL1$, $SL2$ and $SL3$ (Figure 5.8 (right)).

A symmetric airfoil at zero angle of attack immersed in the core of a symmetric Karman wake should experience no-mean lift force. The lift force calculated as an integral of the pressure over the surface S features a non-zero mean value as shown in Figure 5.6 which can be attributed to a slight angle of attack of the airfoil with respect to the free-stream or to a relative misalignment between the rod and the airfoil. The computed mean Cl is approximately 0.03 which, according to the literature, corresponds to a NACA0012 airfoil at an incidence between 2° and 4° .

The effect of a non-zero mean lift is to incline the main radiation pattern of the airfoil, that is perpendicular to the airfoil chord, at an angle with respect to the normal to the free stream. The effect of the angle of attack on the radiation directivity and the results of the aeroacoustic calculation based on integral forces approach are presented in Chapter 6, for different integration volumes. The calculated radiation pattern accounting for both lift and drag forces is shown and compared with literature results.

5.3 Numerical implementation of the algorithm

The aeroacoustic algorithm has been developed within the MATLAB software. The discretized form of equation (5.10) is implemented. The computation is made both with and without retaining the velocity terms at the control surface according to the two methodologies indicated, respectively, as: *non-permeable Curle/FfW-H* and *permeable Curle/FW-H*.

The time-resolved pressure and velocity data needed as source terms for the aeroacoustic prediction, have been evaluated on the point-wise defined control surfaces: S , $SL1$, $SL2$ and $SL3$ indicated in Figure 5.8 (left and right).

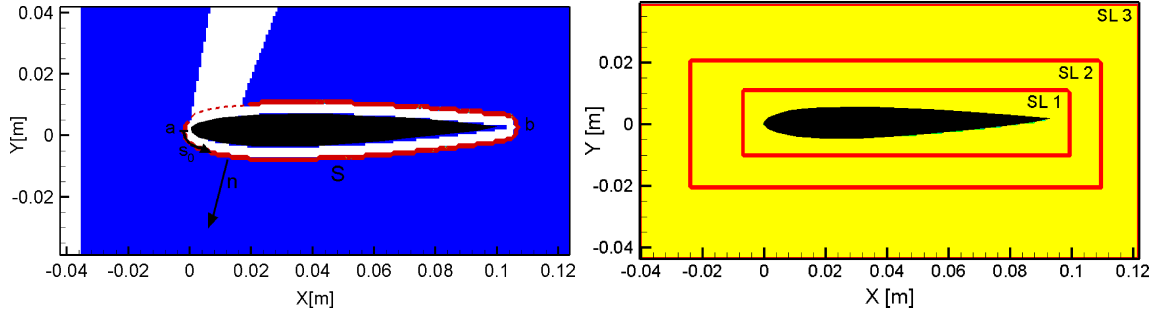


Figure 5.8: Surface S for non-permeable surface approach (left) and surfaces SL1, SL2 and SL3 for permeable surface approach and integral momentum evaluation

The discretized integral on the right hand side of the Curle/FW-H formulation in equation (5.10) over the source surface is computed by means of trapezoidal rule, yielding

$$\int_{S_y} \left(\frac{p' \delta_{ij} + \rho v_i v_j}{r} \right)_{t=t_e} n_i dS = \sum_{k=1}^2 \sum_{i=1}^{N_{source}-1} \sum_{sp=1}^{N_{span}-1} \left[\frac{1}{r(i, sp)} p'_{mid}(i, t - \frac{r(i, sp)}{c}) L_{seg}(sp) n(k) \right] SP_{seg}(i) list(k). \quad (5.14)$$

N_{source} is the number of points on the source line, N_{span} the number of elements in which the span has been divided, p'_{mid} is the value of p' at the midpoint of each surface segment, L_{seg} the length of the segment along the line source, $n(k)$ with $k = 1, 2$ are the component of the outward pointing normal, $list(k)$ the components of the vector indicating the listener position and SP_{seg} the length of a spanwise element. The process is repeated for different listener locations with respect to the airfoil leading edge. Parametric analyses have been performed varying the number of source points, the distance between the source-line and the airfoil and the spanwise correlation length.

The source contribution is taken all around the airfoil. For low frequencies the airfoil has no masking effects on the noise propagation and the contribution of the upper and lower sides of the airfoil on the sound emission are equally perceived by the listener.

Each source contribution term is evaluated in both the vertical lift direction perpendicular to the incoming flow and horizontal drag direction parallel to the incoming flow.

The retarded time is evaluated as $t_e(i, sp) = t - \frac{r(i, sp)}{c}$ in which $r(i, sp)$ indicates the distance between the listener and the surface element locations varying along both the surface plane and the span. When the compact body assumption is made $r(i, sp) \simeq const = R$ and a single retarded time for the source surface is considered.

The time spacing of the velocity and pressure source data coincides with the PIV acquisition time $1/2700$ s. The value of the pressure integral at the retarded time t_e is interpolated by means of cubic spline functions. The time derivative is performed using a first order forward method. The r.m.s. of the acoustic signal and spectrum are calculated. The spectrum calculation is based on the Welch algorithm (see Appendix B) on blocks of 216 ensembles, which allow a frequency resolution of 12.5 Hz, the same as the microphone measurement output.

The 3D nature of the airfoil emission is accounted for by assuming that an equal in phase

emission occurs along a section of the span corresponding to a fraction of the physical span length. The length of the airfoil span outside the shear layers, caused by the wind tunnel nozzle, corresponds to approximately 0.4 m . The correlation length, denoted as C.L. in the plots, is a percentage of the total span and indicates the effective reduced length used for the computation. Autocorrelation of the horizontal velocity component of the spanwise visualization of Figure 4.19 on a window between the rod and the airfoil, is shown in Figure 5.9

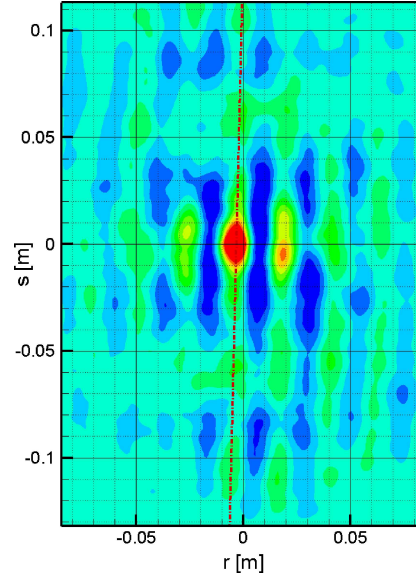


Figure 5.9: Autocorrelation of the horizontal velocity in cylinder wake on a plane aligned with the airfoil span

The inclination of the correlation stripes with respect to the span direction is approximately 2 degrees which, at an average convection velocity of 12 m/s in the Karman wake (see Figure 4.13 and Figure 4.20), corresponds to a maximum phase shift of the vortical impingement lower than 90° . For the observed field of view it can be fairly assumed that no acoustic cancelation due to out of phase emission occurs. Since the performed experiment allowed visualization of only about 25% of the vortical organization along the whole span, the possible cancelation or interference in the noise radiation of different sources along the span could not be properly evaluated. For the aeroacoustic computation it has been assumed a coherent length of in-phase emission ranging from 50% to 100% of the total span length. The variation of the coherence length equally shifts all the components of the computed spectra.

Future aeroacoustic investigations, in the context of the FLOVIST project, will aim at providing 3-D flow field measurements around the noise emitting bodies.

Chapter 6

Results and discussion

In this chapter the results of the implementation of the aeroacoustic code are presented. The dependence of the prediction on numerical parameters is investigated by means of a parametric analysis of the different analogy formulations, the integration surfaces and discretization methods. The results of the aeroacoustic prediction, obtained by implementation of both the non-permeable Curle/FW-H and the permeable Curle/FW-H approaches, are shown for free stream velocities of respectively 10 and 15 m/s . Noise predictions based on integral aerodynamic loads are also presented. For the permeable surface and integral formulations a parametric study has been performed varying the distance of the control surface from the airfoil and the number of surface elements. The results of the aeroacoustic computation are compared with radial far-field microphone measurements and commented. All the computed acoustic pressure signals are presented as small band spectra of 12.5 Hz resolution allowing a direct comparison with the microphones. The airfoil radiation pattern is calculated for several angular and radial positions. A comparison with the results obtained by D. Casalino [10] for the same configuration is also made.

6.1 Comparison between non-permeable and permeable surface formulations

The acoustic spectra resulting from implementation of the non-permeable Curle/FW-H (a) and permeable Curle/FW-H (b) on surface S, at a distance of 1.25 m perpendicular to the airfoil chord ($\theta = 90^\circ$), are compared with the microphone measurements at the same location for 10 and 15 m/s free-stream velocity in Figure 6.1 and 6.2 respectively. The label C.L. in the legend indicates the assumed correlation length of in-phase emission, in percentage of the physical airfoil span length (see section 5.3). The microphone measurements refer to the geometrical configuration of RUN 32 of Chapter 4: $D_{rod} = 6 mm$, distance rod-airfoil = 10.2 cm .

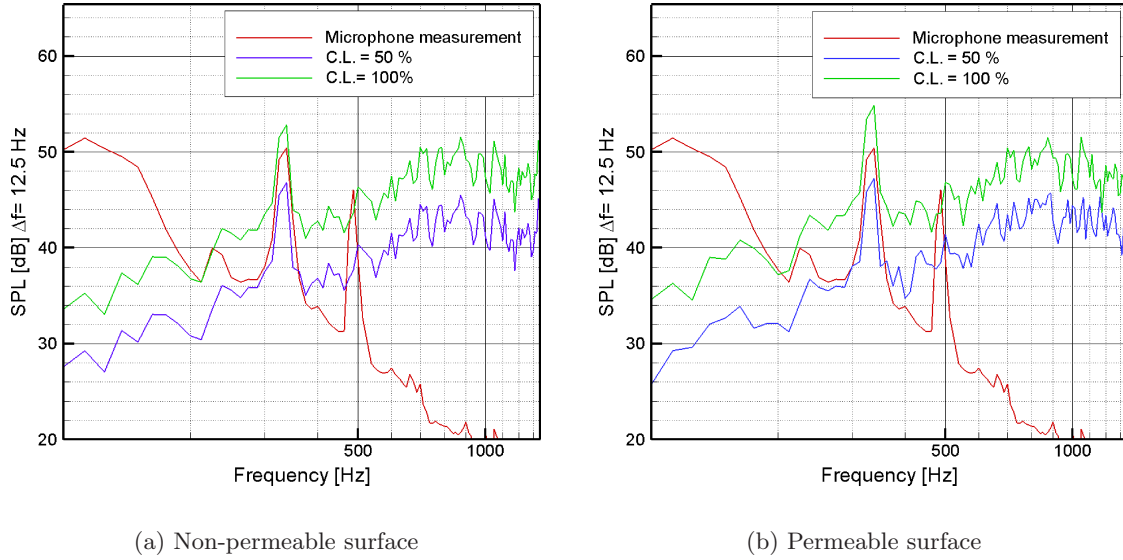


Figure 6.1: Comparison of the non-permeable (a) and permeable (b) formulations on control surface S , with the microphone measurement at $V_\infty = 10 \text{ m/s}$

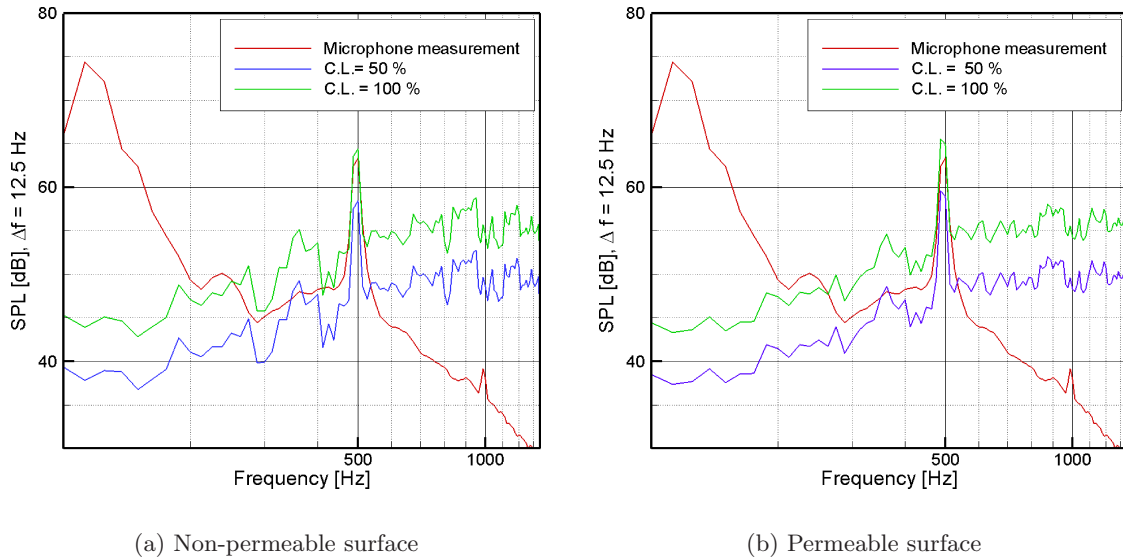


Figure 6.2: Comparison of the non-permeable (a) and permeable (b) formulations on control surface S with the microphone measurement at $V_\infty = 15 \text{ m/s}$

All the computed spectra feature a local peak in correspondence of the rod-shedding frequency at approximately 320 Hz and 500 Hz , respectively for the 10 and 15 m/s case. The low frequency components of the measured spectra have been shown to be caused by the wind tunnel, during preliminary background measurements. These components are not related to the airfoil emission and, consequently, are not revealed by the computation. The measured spectra for the 10 m/s case exhibit a second peak at 487 Hz due to the wind tunnel fans, also

revealed by preliminary acoustic measurements. The higher harmonics, corresponding to 700 Hz for the 10 m/s case and to 1000 Hz for the 15 m/s case, measured by the microphones, are barely visible in the computed spectra because of the dominating noise level at the high frequencies.

The permeable surface approach for both the free-stream velocities exhibits higher amplitude levels at the peak frequency probably due to the inclusion of the velocity fluctuations at the control surface as additional source contribution. The broadband component of the computed spectra does not decay according to the measurements since it is strongly affected by experimental and numerical noise which has been ascribed to:

- 3D motion effects
- Insufficient time resolution of the velocity and pressure fields
- Inaccuracy of the experimental data

The discontinuous character of the pressure signal revealed by Figure 5.2 is mostly responsible for the appearance of the high frequency components of the spectrum. These have no physical nature and cannot be compared with the microphone measurements.

Linearity of the sound propagation allows the separate analysis of each single component of the spectrum. As long as one is interested in the magnitude of the acoustic emission at the tonal frequency, implementation of the aeroacoustic analogies reveals an accuracy within 10 % with respect to the measured SPL, for both 10 and 15 m/s free-stream, varying with the spanwise coherence length.

It has been found by preliminary analysis, performed with synthetic sources, that the accuracy of the computed SPL decreases as the frequency of the source increases. This is because the sampled signal does not allow for an accurate reconstruction of actual signals for frequencies above a fraction of the Nyquist cut-off. A comparison between Figure 6.1 and 6.2 reveals this condition in which the prediction of the 10 m/s , for both the analogy approaches, shows higher magnitude (relative to the microphone spectrum) with respect to 15 m/s velocity. The 10 m/s free-stream corresponds to a Strouhal frequency of about 320 Hz meaning approximatively 8 samples per cycle at 2700 Hz sampling frequency. The number of samples reduces to about 5 for the 15 m/s free-stream. A better accuracy for the former case was indeed expected.

6.2 Effect of the discrete method used for time derivatives

The time derivative in equation (5.10) has been calculated using forward and central discretization methods, for both the permeable and non-permeable formulations. The results are shown in Figure 6.3 for 10 m/s (a) and 15 m/s (b).

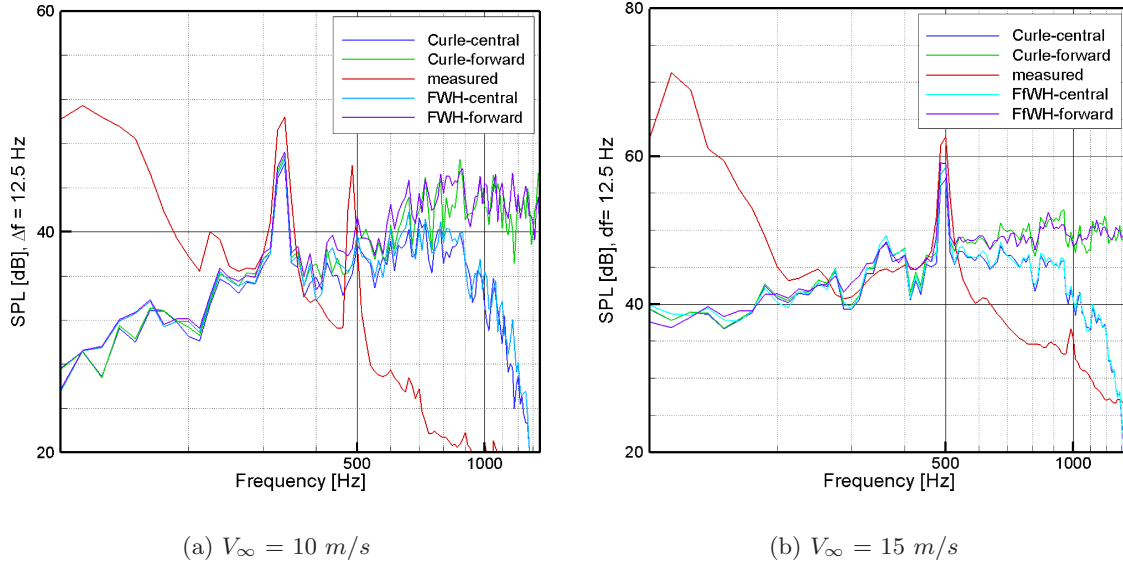


Figure 6.3: Effect of forward and central discretization schemes for the time derivative with C.L. = 50 % on surface S

The spectra computed with the permeable and non-permeable Curle/FW-H approaches approximately coincide for both the 10 and the 15 m/s case. The main influence on the spectra is determined by the method chosen for the time derivative. The sharp decay of the spectrum calculated with the central scheme, has no physical meaning. This is mainly due to numerical smoothing of the signal in the evaluation of the derivatives. The peak levels obtained by the use of a forward scheme exhibit slightly higher magnitude with respect to the central scheme. This is better appreciable for the 15 m/s case.

The numerical evaluation of the derivatives causes an artificial magnitude reduction, when compared with the analytical derivative, which becomes more significant with increasing the frequency. The reduction becomes more effective in case of a central scheme because of the use of a wider kernel for the computation of the differences.

The forward discretization method has been shown, in previous computations, to provide better magnitude estimations for monochromatic signals with frequencies corresponding to the Strouhal frequencies of the 10 and 15 m/s cases, at the present sampling frequency. This method, on the other hand, overestimates the high frequency components in the case of noisy data as revealed by Figure 6.3.

A forward discretization scheme for the time derivatives has mostly been used in the present calculations since the analysis is mainly focused on the tonal peak. The present investigation does not allow the resolution of the broadband spectral component.

6.3 Influence of the integration surface

The spectra calculated using the permeable Curle/FW-H formulation on the four integration surfaces indicated in Figure 5.8, assuming 50% spanwise correlation length, are presented in Figure 6.4

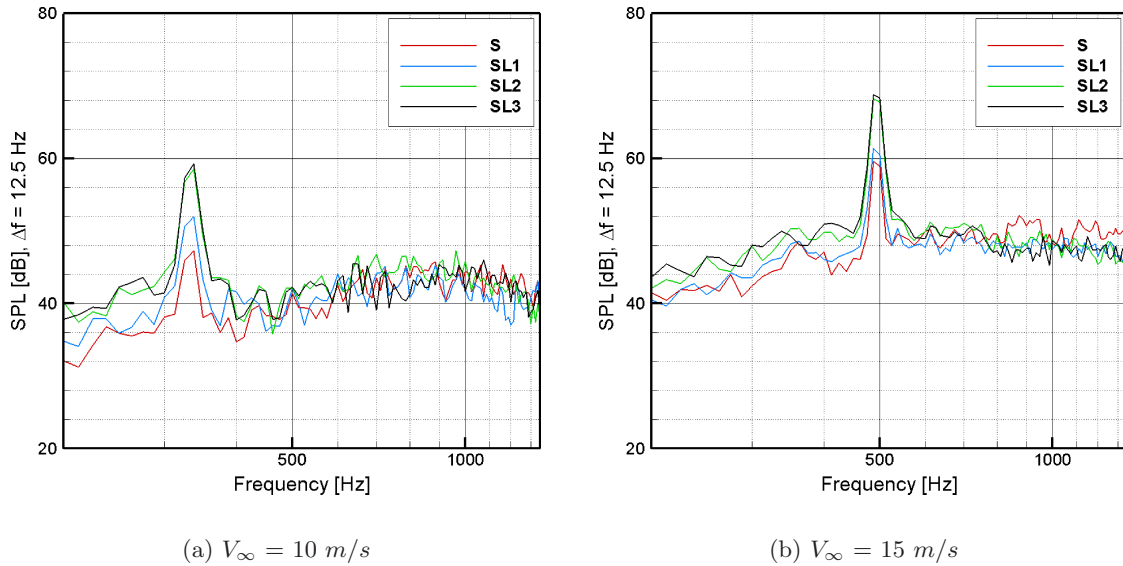


Figure 6.4: Acoustic computation based on permeable Curle/FW-H formulation on different permeable surfaces with C.L. = 50 %

The magnitude of the low frequency components of the computed spectrum, including the peak frequency, increases as the control surface is moved away from the airfoil surface. The increase has been ascribed to the fact that an higher number of quadrupolar source terms, generated by the turbulence surrounding the airfoil, are accounted for by the integration surface as this increases in dimensions. Quadrupolar sources external to the surface have been neglected in the present investigation. This could explain the lower level of the prediction for surfaces S and S1. The agreement between the spectra at surface S2 and S3 seems indicating that at the distance of surface S2 the acoustic prediction by means of the permeable FW-H approach becomes independent of the integration surface. Further systematic studies are required to confirm the latter conclusion and to carefully analyze the influence of the integration surface on the noise prediction. The effect of the variation of the integration surface is not noticeable for high frequency because of the high noise level.

The spectra relative to the non-permeable surface approach on the four integration surfaces are shown in Figure 6.5.

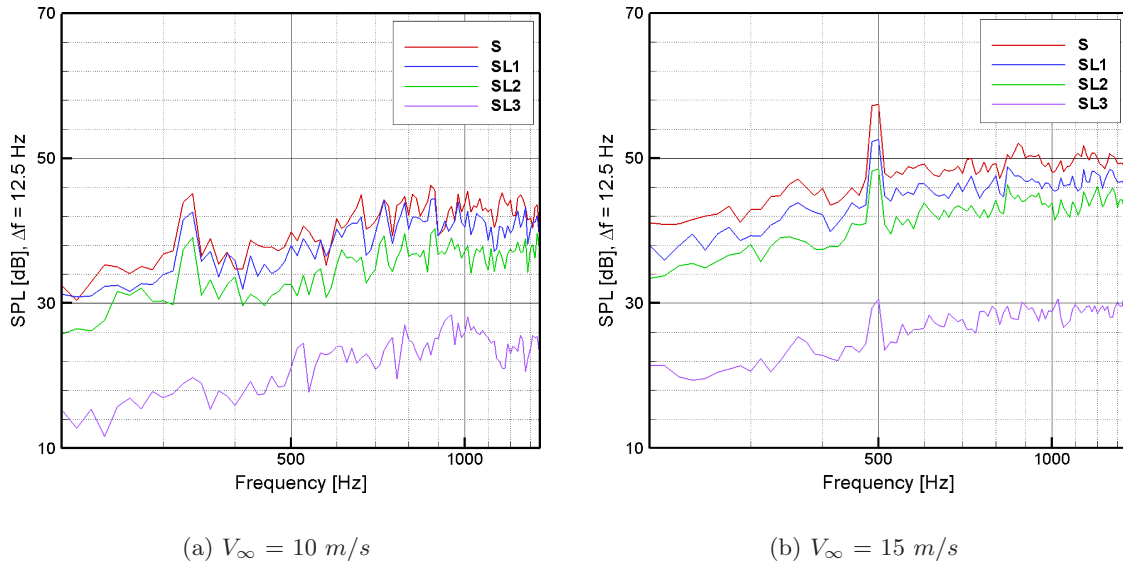


Figure 6.5: Acoustic computation based on non-permeable Curle/FW-H formulation on different permeable surfaces with C.L. = 50 %

The contribution of the static pressure at the integration surface to the total noise emission decreases as the surface is moved away from the airfoil. The noise prediction based on the non-permeable surface approach loses accuracy as far as the surface does not coincide with the physical surface. When a permeable surface is employed, the decrease of static pressure with the distance from the body is balanced by an increase of the dynamic pressure contribution represented by the velocity components in the integral of equation (5.10). It can be concluded that the applicability of the non-permeable Curle/FW-H is confined to a region strictly close to the physical noise generating surface.

The permeable control surface S1 has been discretized using different numbers of piecewise linear elements, namely: 184 and 92. The influence on the computed spectra is shown in Figure 6.6 (a) for 10 m/s and (b) for 15 m/s free-stream.

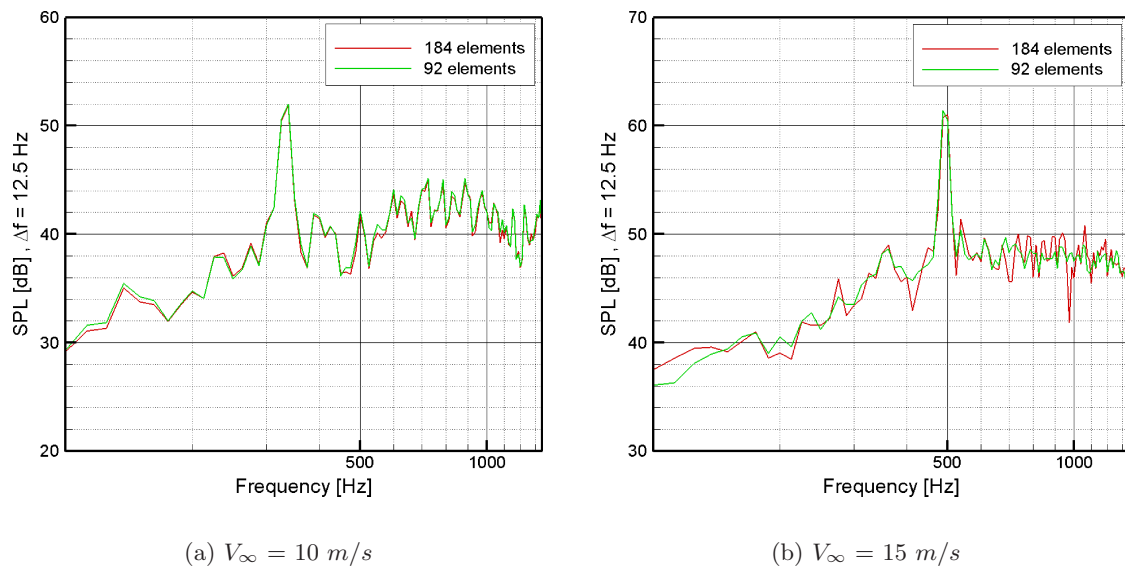


Figure 6.6: Acoustic spectra based on the permeable surface SL1 for different numbers of surface elements with C.L. = 50 %

Variation of the number of points reveals having small influence on the computed spectrum. The discrepancies increase for the 15 m/s case. A possible explanation is that vortical structures generated at the interaction with the airfoil decrease in dimensions as the strength of the impingement (proportional to the velocity) increases and the relative spatial resolution of the integration surface to detect them decreases. This results in an overall smoothing of the spectrum as the number of surface elements decreases.

6.4 Integral loads approach

The aeroacoustic predictions based on integral evaluation of the lift and drag forces (see Gutin's principle in Chapter 2) are presented in Figure 6.7 for 10 and 15 m/s respectively and for the three integration surfaces SL1, SL2 and SL3 indicated in Figure 5.8 (C.L. = 50 %).

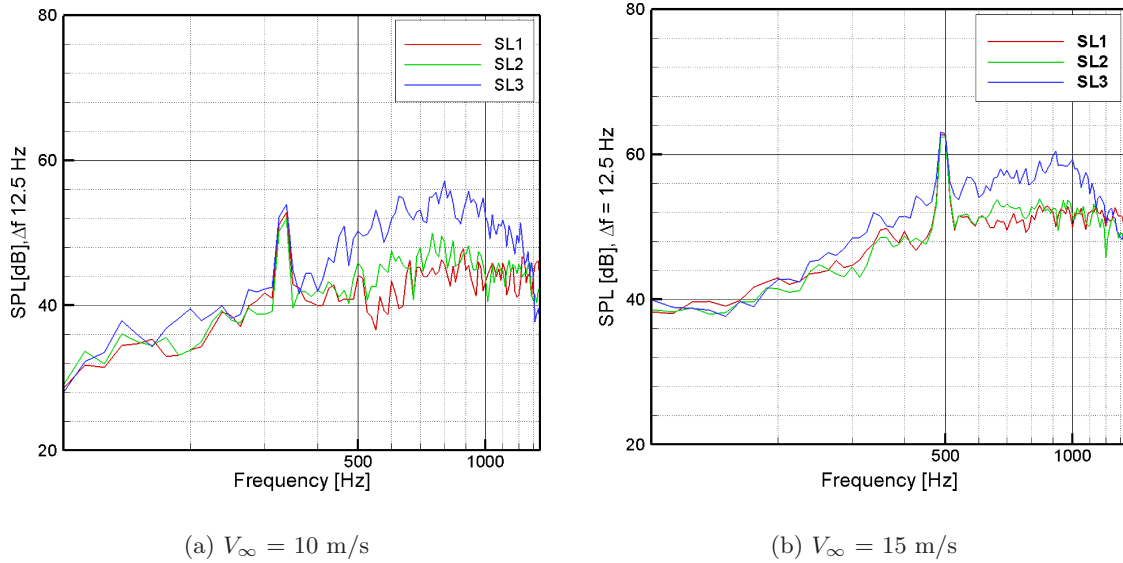


Figure 6.7: Acoustic spectra calculated by integral loads approach on different integration volumes with C.L. = 50 %

The magnitude of the tonal component does not change with the variation of the integration surface. On the other hand, the high frequency spectral components increase as the surface is moved away from the body. When the control volume for evaluation of the momentum integral is enlarged a bigger part of the flow region is included in the computational domain. Additional high frequency noise is included by the integration of the velocity time derivatives over a larger surface. As the distance from the airfoil increases this contribution becomes increasingly significant.

In the low frequency range, the integral loads approach reveals a stronger invariance for different integration surfaces with respect to the discrete approach, probably because of mutual cancelation of random errors during the volumetric integration. The latter approach seems preferable in case of nonsmooth source data, provided that the compact body requirement is met.

6.5 Radiation directivity

The sound spectra measured by the four microphones indicated in Figure 4.3 in the acoustic setup section 4.2, for rod-airfoil configuration with 6 mm rod diameter at 10 m/s (a) and 15 m/s (b) free-stream, are shown in Figure 6.8. Microphone 1, 2, 3 and 4 correspond to angles of respectively 90°, 117°, 135° and 143° with respect to the airfoil chord at 1.25 m distance.

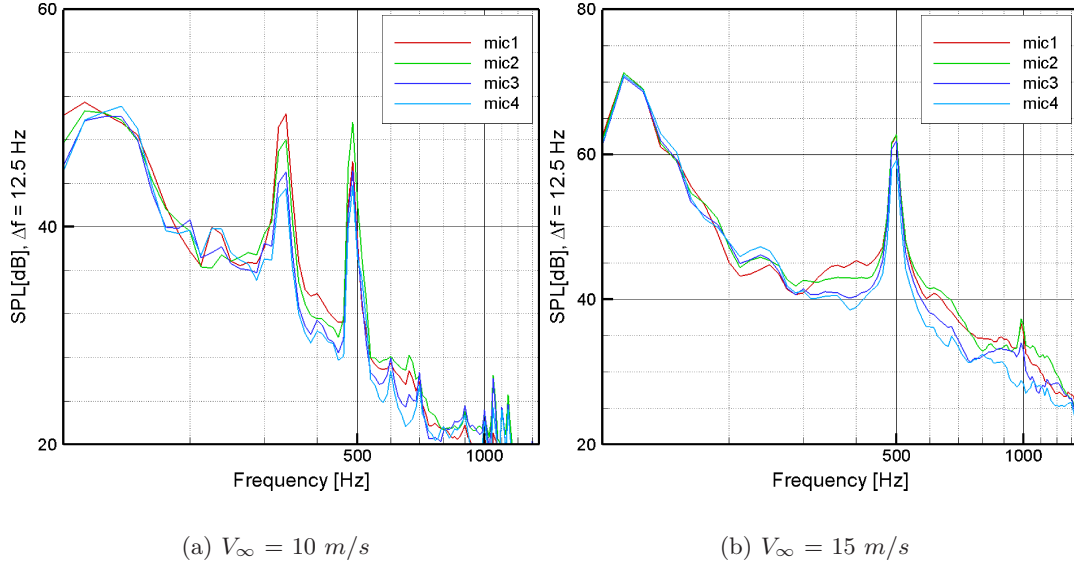


Figure 6.8: Rod-airfoil noise spectra measured by four microphones at 1.25 m distance. $D_{rod} = 6$ mm, rod-airfoil distance = 10.2 cm

The pressure signals measured by microphones 2, 3 and 4 have been corrected for the presence of the wind tunnel shear layer between the airfoil and the microphones. Refraction of the acoustic waves due to the shear layer induces an alteration of the effective observation angle of the microphone and an amplitude modulation due to the variation of the effective distance between the source and the microphone. The adopted angular correction follows the procedure indicated by Amiet in [3]. Amplitude corrections can be neglected for radial microphones disposition in the case of small distance between the center of curvature and the position of the shear layer. The angle correction for the three microphones are indicated in Figure 6.9. For microphone 1 perpendicular to the shear layer no angular correction is needed, according to Snell's law of refraction.

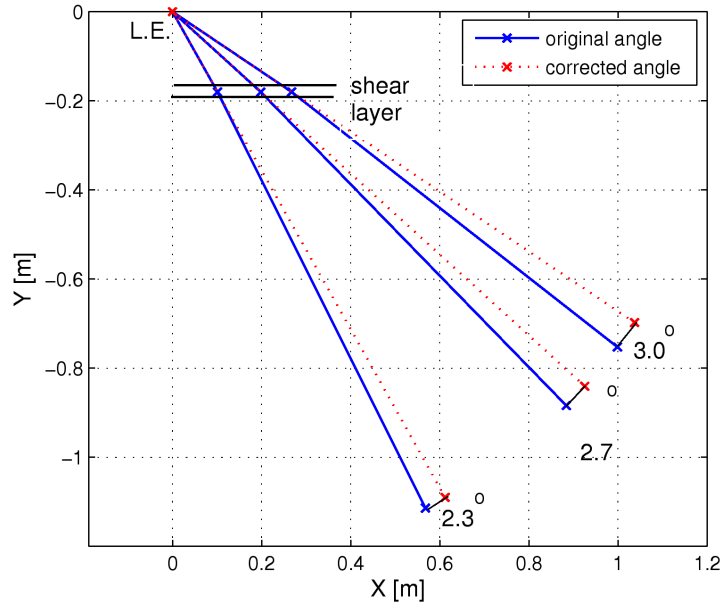


Figure 6.9: Amiet's angular correction for refraction due to the shear layer.

The corrected observation angles of the microphones are: 90° , 119° , 138° and 146° . Computation of the spectra at the corrected angles has been performed for 10 (a) and 15 m/s (b). The spectra are shown in Figure 6.10

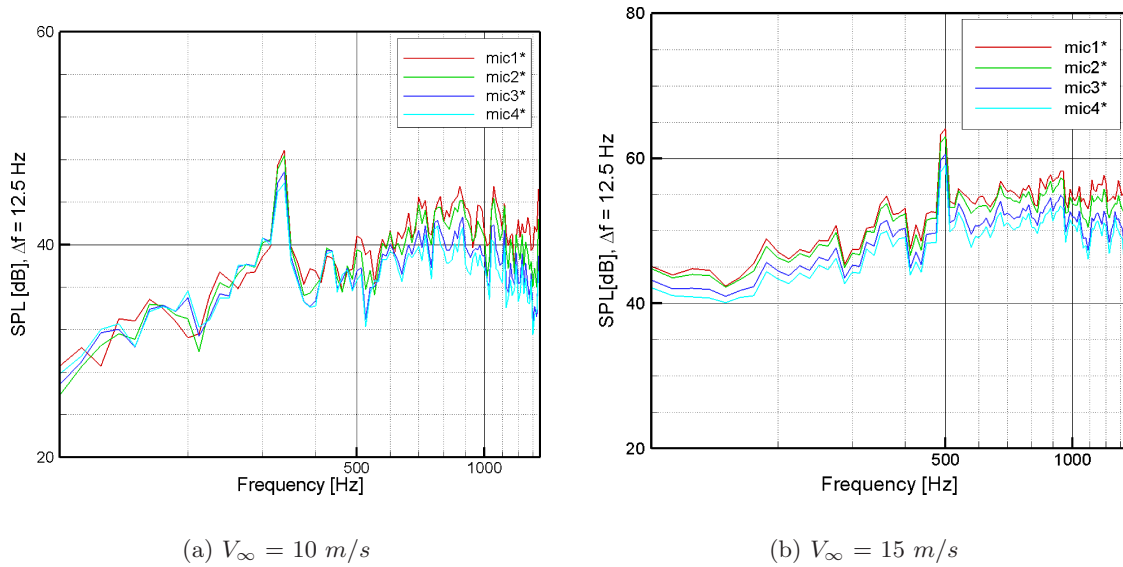


Figure 6.10: Computed small band spectra at four angular microphone locations: $D_{rod} = 6 \text{ mm}$, C.L. = 50 %

The symbol * on the microphone name indicates that the microphone position has been corrected for the shear layer. The magnitude decay of the computed spectra for increasing angle

θ with respect to the normal to the airfoil chord shows good agreement with the measured spectra of Figure 6.8 for both 10 and 15 m/s cases for all the spectral components.

Figure 6.11 shows the decay of the pressure signal moving away from the airfoil. The decay of the SPL for the small band around peak frequency coincides with the expected $1/R$ decay, characteristic of spherical acoustic waves. The decay of the OASPL, over the all computed spectrum, does not match the physical $1/R$ decay because of the additional broadband numerical noise affecting the acoustic pressure signal.

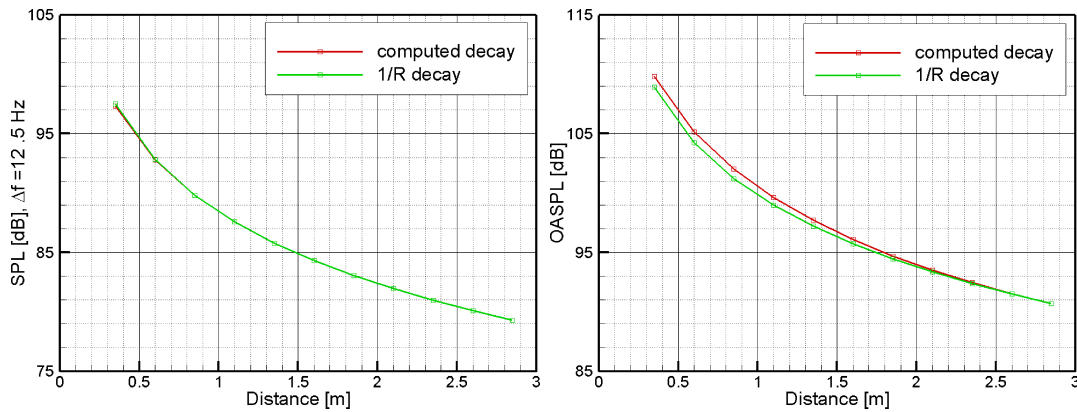


Figure 6.11: Decay of the SPL at peak frequency(left) and of the OASPL (right) with distance R from the airfoil

The spatio-temporal distribution of the acoustic fluctuations has been analyzed. For the chosen configuration the analogy equations are solved in polar coordinates and later represented in a Cartesian system of coordinates. Figure 6.12 shows a time sequence of the numerically computed sound radiated by the airfoil at a distance of 1.25 m (where the microphones are located) to 2.25 m . The noise propagation is mainly perpendicular to the airfoil chord. Similar propagation features can be noticed between two contours on the same row, spaced by approximatively 1 shedding period.

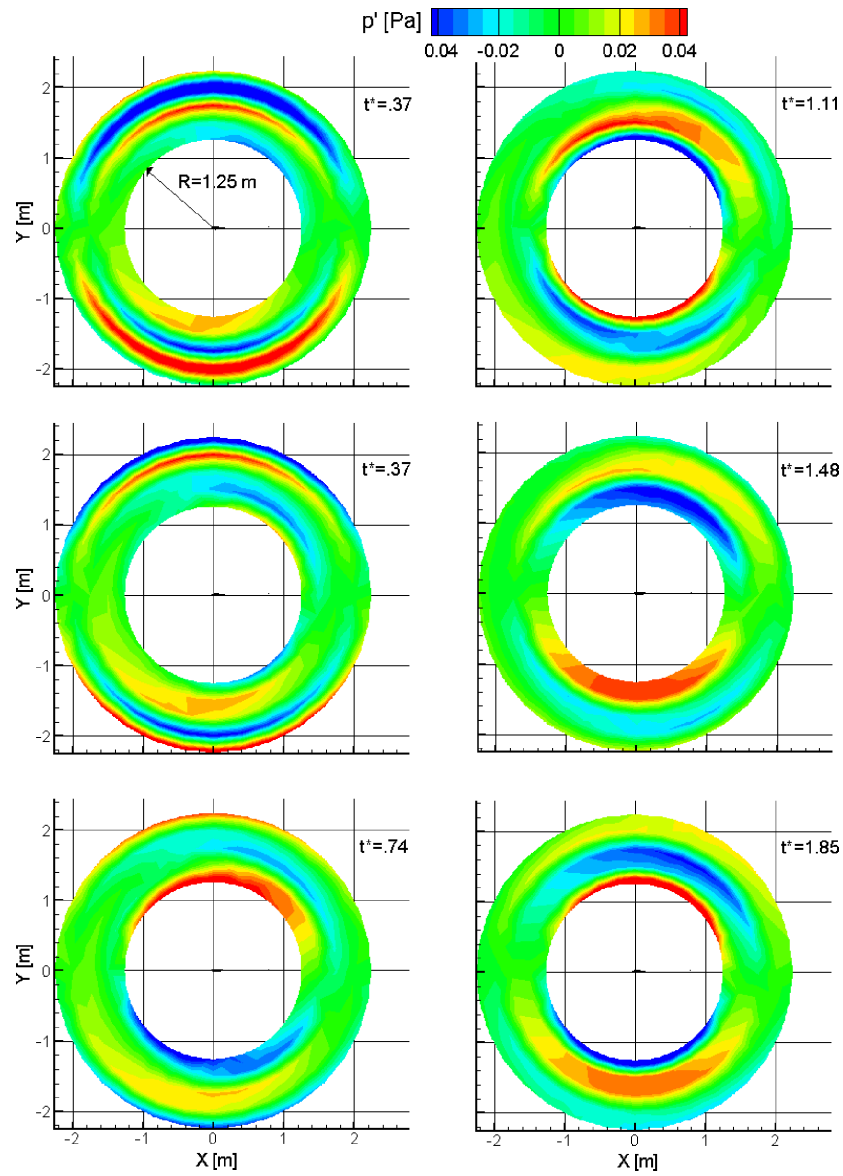


Figure 6.12: Time sequence of the radiated pressure fluctuation p' at normalized times t^*

6.6 Comparison with the results of Casalino

A comparison with the results obtained by D. Casalino [10] on a rod-airfoil configuration using a hybrid RANS-FW-H method together with far-field acoustic measurements is presented. The specifics of the analysis performed by Casalino are summarized in Table 6.1.

Table 6.1: Specifics of Casalino's investigation

General configuration	
Free-stream velocity:	20 <i>m/s</i>
Cylinder diameter:	1.6 <i>cm</i>
Airfoil chord:	10 <i>cm</i>
Airfoil span:	30 <i>cm</i>
Distance rod-airfoil :	10.4 <i>cm</i>
Reynolds number (chord):	1.38×10^5
Acoustic measurement setup	
Distance airfoil-microphone:	1.38 <i>m</i>
Angular measurement locations:	60 (6° spacing)
Small band resolution:	32.5 <i>Hz</i>

The vortical release and impingement process has revealed to be an intrinsic highly 3D phenomenon in particular in proximity to the airfoil leading edge. When the spectra are computed based on a purely 2D model the broadband components of the acoustic spectrum are usually underestimated [29]. Casalino [10] exploited a statistical model for the spanwise correction based on Gaussian correlation functions. The width of the correlation function relies on statistical quantities measured by pressure transducers placed along the rod and airfoil spans. The measured correlation length is used to evaluate a different retarded time, corresponding to an introduced random emission phase shift for every span element, the latter having the dimension of one correlation length.

Introduction of random three dimensional spanwise effects increases the accuracy of the prediction of broadband components as shown in Figure 6.13(b). The model, however, requires a priori knowledge of the spanwise correlation length which can be achieved by the use of pressure transducers or by 3D flow visualization. A similar statistical correlation modeling has been employed in the present analysis and the results, for spanwise coherence length of 10 cm and a random retarded time corresponding to a phase shift between 0° and 90°, are shown in Figure 6.13(a).

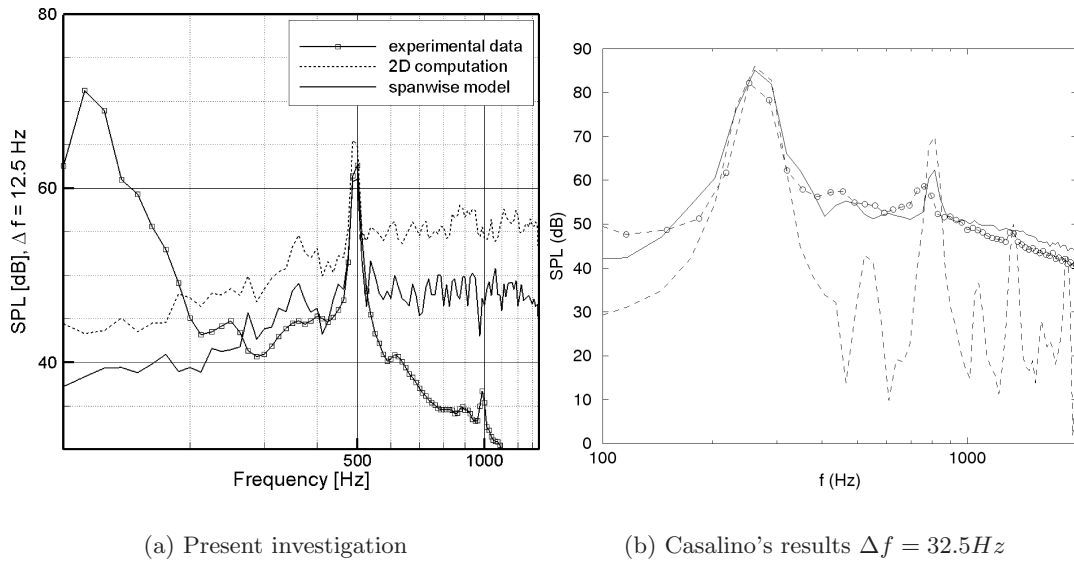


Figure 6.13: Qualitative comparison of the acoustic spectra calculated with a spanwise random model with the results of Casalino. Experimental data (labeled line), 2D flow computation (dashed line) and spanwise statistical modeling (solid line)

Including a spanwise random emission shift improves the prediction of the low frequency components with respect to the fully 2D prediction. The magnitude of the peak frequency component shows a slightly better agreement with the measured spectrum. The improvements in the prediction of the broadband component can be only partially appreciated in the present analysis because of the masking effect of the high noise level.

The radiation directivity of the airfoil has been calculated for 90 angular locations ($\Delta\theta = 4^\circ$) at 1.25 m distance. The result is shown in Figure 6.14 (left).

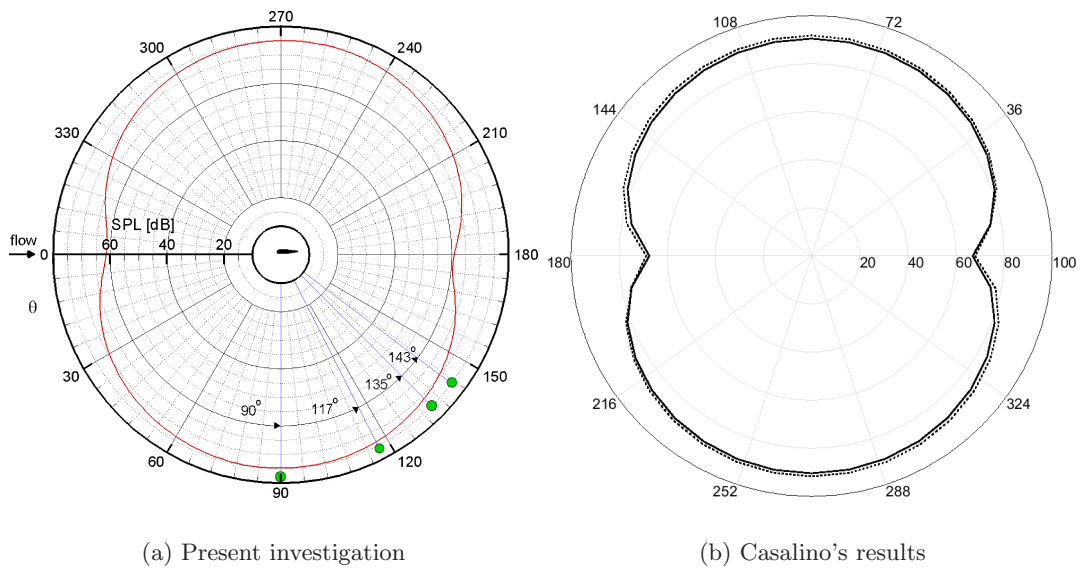


Figure 6.14: Airfoil radiation directivity

The emission directivity is mainly perpendicular to the airfoil chord, aligned with the direction of the fluctuating lift experienced by the airfoil as a consequence of the vortical impingement, in fair agreement with the results of Casalino. The slight backward tilting of the dipolar lobe is attributable to the non zero angle of attack of the airfoil revealed by the non-zero mean lift force shown in Figure 5.6 corresponding to an angle between 2° and 4° . This is confirmed by the dashed lobe in Figure 6.14 (b) measured by Casalino for an angle of attack of -4° of the airfoil with the free-stream direction. Casalino's plot is made for an opposite angle of attack with respect to the present experiment. This explains the opposite tilting of the emission lobes.

Conclusions and recommendations for further investigations

An aeroacoustic investigation on a rod-airfoil configuration has been performed using time-resolved PIV data. The velocity fields calculated around the airfoil were used to calculate the unsteady pressure field by means of a 2D based Poisson solver. Velocity and pressure evaluated on specific integration surfaces constituted the source term of the implemented aeroacoustic analogy based on both non-permeable and permeable surface approaches. The acoustic predictions based on numerical computation were compared with microphone measurements at corresponding locations. Variation of the acoustic spectra for different geometries of the integration surface was analyzed. A comparison was made with the results obtained by Casalino, for a similar configuration, regarding the effects of spanwise modeling and the radiation directivity pattern.

7.1 Conclusions

The purpose of the present work was to prove the feasibility of a time-resolved PIV flow description for an aeroacoustic prediction. The linearity of the acoustic propagation phenomenon allows to analyze the accuracy of the prediction independently for each component of the computed spectra.

The high-frequency components of the spectrum are strongly influenced by the 3D motion effects and by the time resolution of the velocity data. The pressure deduced from the Poisson solver is already strongly affected by these effects.

The low frequency components of the measured spectra are not directly related to the airfoil emission, therefore a direct comparison with the computed spectra was not possible.

All the calculated acoustic spectra exhibit a local peak corresponding to the rod-shedding frequency. When the analysis is focused on this component of the spectrum, which gives the highest contribution to the total noise emission, the method is capable of predicting the SPL with an accuracy of over 90 % with respect to the microphone measurements, depending on the assumed spanwise correlation length. The latter correlation length revealed having a strong influence on the overall magnitude of the predicted SPL.

The small band spectra calculated with the permeable Curle/FWH exhibit a higher overall magnitude level with respect to the non-permeable approach due to the inclusion of the velocity components at the surface.

The integral loads formulation reveals higher invariancy for different integration surfaces with respect to the discrete formulation attributable to the mutual cancelation of random errors during integration over the control volume. The latter approach seems preferable in case of nonsmooth source data, provided that the compact body requirement is met.

The implementation of a statistical model for the spanwise radiation based on 4 spanwise elements seems to allow a slightly more accurate evaluation of the peak and low frequency components with respect to the purely 2D approach. Only partial improvements in the evaluation of the broadband component could be achieved because of the overwhelming noise level.

The calculated Sound Pressure Level (SPL) revealed to be influenced by several factors mainly connected to the experimental limitations of the present investigation. The most relevant are summarized in the following:

3D effects Span wise visualizations between the rod and the airfoil revealed a considerable instantaneous out-of-plane velocity component with maxima of the order of 30 % of the convection in-plane velocity. The pressure algorithm does not account for 3D flow motion. When the planar pressure is evaluated based only on the planar velocity components, the occurrence of out-of-plane motion implies a readjustment of the planar pressure field to account for the sudden variation of the in-plane velocity field. This results in a non-smooth pressure signal in time which affects the calculation of the time derivatives needed for the acoustic prediction.

The thickness noise term of the FW-H equation can be calculated as the total mass flux across a three dimensional surface embedding the whole emitting body. In the present case it was not possible to evaluate this term.

The lack of spanwise flow description precludes an accurate evaluation of the vortical impingement along the airfoil span. This implies that possible acoustic interaction or cancelation due to out of phase emissions along the span could not be taken into account.

Low time-resolution The time resolution of the velocity and pressure fields corresponds to the image acquisition frequency of the PIV system (2.7 kHz). This allows for a reliable evaluation of only a limited part of the noise spectrum. As the radiation frequency increases, the number of available samples per wavelength decreases. The inaccuracy in the SPL prediction due to low sampling of the data affects the spectral components far below the Nyquist cut-off frequency because of aliasing. When only the peak frequency is analyzed the 10 m/s case, corresponding to a shedding frequency of about 320 Hz , offers a resolution of about 8 samples per cycle against the 5 samples per cycle of the 15 m/s case. The 20 m/s case has not been analyzed in the present investigation due to insufficient time resolution. Time derivatives performed on a non-smooth signal result in a strong amplification of the signal noise which can eventually overwhelm the quantity to be measured, especially for the high frequency spectral components. Higher order time differentiation schemes involving a wider kernel introduce an amplitude reduction of the signal which becomes more significant as the number of samples per wavelength decreases.

Space resolution The space resolution of the velocity field depends on both the physical field of view and the PIV processing. The choice of the field of view FOV-2CAM has been a compromise between space resolution and completeness of information. Implementation of the aeroacoustic analogies requires knowledge of velocity and pressure on a closed surface embedding the whole radiating body. Detection of the smaller velocity scales on the other hand, depends on the spacing of the velocity vectors. In the present analysis, the use of the WIDIM iterative algorithm with final integration window size of 31×31 *pixels* with 75 % overlap allowed for a resolution to 0.68 mm per vector. Curle's approach requires evaluation of the fluctuating pressure at the physical surface of the noise emitting body. The spatial resolution of the present PIV analysis provided reliable velocity field vector at a minimum distance of about 5 pixels with respect to the airfoil surface because of correlation of the particles light immediately outside the surface with the zero-velocity mask coinciding with the airfoil.

Incompressibility assumption The Poisson solver and the aeroacoustic formulations assume constant density throughout the domain. Variation of specific volume of fluid elements are usually neglected in fluid dynamic computations, giving a minor contribution to the dynamics of the flow for low Mach numbers. It, consequently, constitutes a minor source of inaccuracy in the evaluation of the pressure field. When dealing with acoustics particular attention must be paid to local density variations due to elasticity of the acoustic medium. From an aeroacoustic point of view an unsteady flow can be considered incompressible if the following conditions are satisfied:

- a $M \ll 1$, flow convection much slower than acoustic propagation (steady incompressibility condition)
- b $He^2 \ll 1$, where He indicates the Helmholtz number $He = \frac{2\pi L}{\lambda}$, L is the characteristic length scale of the flow and λ the wavelength of the emitted sound. It requires that the distance traveled by the flow in a certain time interval is much smaller than the distance traveled by the acoustic perturbation in the same time interval.

The flow Mach number of the present experiment slightly varied around the value 0.05. The first condition for incompressibility is thus fully fulfilled. The second incompressibility condition requires the integration surface to be small compared to the acoustic wavelength. This is true if the quantity L is referred to the dimensions of the planar integration surface. As long as the airfoil span length is considered, a comparison with the wavelength at 15 m/s free-stream corresponding to approximately 70 cm would reveal that the second incompressibility condition is not completely satisfied and possible acoustic scattering along the airfoil span should be analyzed. This has not been possible in the present investigation because of the 2D character of the visualization. Density variations of acoustic nature inside the flow region, according to an order of magnitude estimation based on linearized acoustics, scale with the square of the Mach number. Acoustic pressure fluctuation have been neglected at the integration surface in comparison with hydrodynamic pressure fluctuations. When the surface is moved away from the body these contributions would become increasingly more important. The aeroacoustic radiation perceived by a listener is indeed, constituted by these minor acoustic density (pressure) fluctuations. Neglecting acoustic contributions in the evaluation of the surface term, for non-compact geometries can strongly influence the final

acoustic prediction. The incompressibility assumptions can be released by the use of a flow description including acoustic phenomena.

Spurious velocity zones In the shadow regions caused by refraction of the laser light behind the airfoil and close to the airfoil surface no velocity data were available and the velocity inside was set to zero. The local discontinuity of the velocity field affected the computation of the total pressure field decreasing the signal to noise ratio of the pressure signal. The total field of view FOV-2CAM around the airfoil has been obtained by merging the single fields of view of two cameras. The cameras were slightly tilted with respect to the airfoil span plane resulting in a slightly prospective view of the airfoil. While merging the images, the local particle discontinuities gave rise to spurious velocity gradients in the velocity computation. This could be avoided making the configuration more closely accessible or making use of a single camera in future experiments.

Strong improvements in the determination of velocity and pressure fields have been obtained by PIV image treatment. Normalization of the light intensity of each pixel with its time average increased the signal to noise ratio of the velocity field also increasing the spatial resolution, in particular near the airfoil surface. The shadow regions were completely removed by mirroring the recorded particles at interface with the shadow zone. Major improvements in the time resolution of the signal have been obtained by a second order Lagrangian interpolation of the velocity field based on the Taylor hypothesis. This led to an increase of time resolution of the velocity and pressure fields by a factor 5.

Aeroacoustic predictions based on the refined velocity and pressure data will be performed.

7.2 Recommendations for further investigations

The present study revealed the degree of applicability and the limitations of the specific PIV experiment for an aeroacoustic prediction. Although most of the results refer to the specific case under consideration, some general conclusions can be drawn which could reveal useful for further investigations inside the FLOVIST project.

Possible solutions to overcome the above mentioned experimental limitations are:

3D flow visualization The use of Tomographic PIV [20] would allow visualization of the flow all around the emitting body (or flow source region). This would release from any assumption on the actual 3D phase emission and would include the effects of sources interaction along the span. The use of a 3-dimensional control surface together with an improved time resolution of hydrodynamic fields would permit an accurate evaluation of the aeroacoustic sources including the thickness noise term.

Higher time resolution The increase of the time resolution of the velocity, and consequently the pressure field, would improve the evaluation of the broadband component of the acoustic spectrum. If the signal is well resolved in time, local filtering could also be applied in order to remove part of the experimental noise.

Higher space resolution Higher spatial resolution of the velocity and pressure fields would allow a description of the smaller flow scales responsible for the highest components of the noise spectrum. Improvements in the spatial resolution of the velocity field in

proximity to the surface can be achieved by iterative deformation and size reduction of the correlation window for the PIV computation approaching the surface. This would allow the implementation of Curle's analogy on a control surface closer to the actual airfoil surface and a better evaluation of the pressure at the wall. In presence of relevant acoustic phenomena, a high spatial resolution of the PIV measure would enable to solve the acoustic velocity scales. This would mean including compressibility effects in the measurement and remove the incompressibility assumptions.

Influence of the integration surface Systematic studies on the influence of the integration surface on the acoustic prediction should be performed, varying both location and resolution of the control surface in order to obtain the independence of the acoustic prediction from the resolution method.

Alternative approaches for future investigations on vortex-structure interaction problems have been proposed:

- A way to avoid the problems connected with the time derivation of the signal would be a reformulation of the aeroacoustic equations in the frequency domain. This would allow a straightforward evaluation of the time derivative. High time resolution of the source quantities is however required for a proper evaluation of the high frequency components of the DFT of the signals.
- Computation of the pressure field by means of PPI numerical procedure, especially in presence of experimental errors, introduces further inaccuracies in the aeroacoustic prediction. Calculation of the pressure field can be completely by-passed by the use of Taylored Green's functions (see Appendix C) which automatically satisfy the boundary condition at the control surface. These functions are usually obtained by conformal mapping techniques and apart from easy geometries need to be numerically calculated for the specific analyzed configuration.
- An alternative approach proposed by Amiet (1974) [2] for noise prediction for turbulence-airfoil interaction, is based on the evaluation of turbulence statistical quantities and analytical response function of the airfoil. Time-resolved PIV can be used for evaluation of the statistical quantities of the flow field [48]. Amiet's formalism for noise radiated by an airfoil with small chord relative to the sound wavelength leads to the identification of the fluctuating aerodynamics loads on the airfoil as main noise source terms, similarly to Howe [27] and Curle [14] analogies for compact geometries (Gutin's principle).

Quantities to be evaluated in an aeroacoustic analogy are usually very small compared to the causes of the noise radiation. A detailed description of the sources is indispensable for a reliable acoustic prediction. The present investigation, in the limits of the experimental conditions, revealed that experimental approaches are suitable for aeroacoustic predictions provided that the requirements on spatio-temporal resolution can be met by the measurement apparatus. The continuous improvements of the experimental devices for time-resolved flow visualization techniques provide good prospects for developments of experimental PIV-based aeroacoustic investigations.

Bibliography

- [1] *Microphone Handbook*. Brüel & Kjær, 1996. [37]
- [2] R. K. Amiet. Acoustic radiation from an airfoil in a turbulent stream. *Journal of Sound and Vibrations*, 41:407–420, 1974. [103]
- [3] R. K. Amiet. Refraction of sound by a shear layer. *Journal of Sound and Vibration*, 58: 467–482, 1978. [91]
- [4] J. Anthoine. Fundamentals of aero-acoustical analogies. In *Basics of Aero-Acoustics and Thermo-Acoustics*, J. Anthoine editor, LS 2007-09. von Karman Institute, Rhode-St-Genèse, 2007. [19]
- [5] B. Barsikow. Experiences with variuos configurations of microphone arrays used to locate sound sources on railway trains operated by the DB AG. *Journal of Sound and Vibration*, 193:283–293, 1996. [41]
- [6] G. K. Batchelor. *An Introduction to Fluid Dynamics*. Cambridge University Press, 1967. [119, 120]
- [7] J. S. Bendat. *Engineering application of correlation and spectral analysis*. 1980. [117]
- [8] M. M. Boone and D. de Vries. *Geluidbeheersing/Sound Control*. TUDelft press, Faculteit Technische Natuurwetenschappen/Faculty of Applied Physics, September 2004. [8, 37]
- [9] K. S. Brentner and F. Farassat. Analytical comparison of the Acoustic Analogy and Kirchhoff formulation for moving surfaces. *AIAA*, 36, No. 8:1379–1386, 1998. [5, 20, 22]
- [10] D. Casalino. *Analytical and numerical methods in vortex-body aeroacoustics*. PhD thesis, Politecnico di Torino et L'École Centrale de Lyon, 2002. [3, 12, 56, 66, 67, 83, 95]
- [11] D. Casalino, M. Jacob, and M. Roger. Prediction of rod-airfoil interaction noise using the Ffowcs-Williams-Hawkings analogy. *AIAA*, 41:182191, 2003. [3]
- [12] T. Colonius and S. K. Lele. Computational aeroacoustics: progress on nonlinear problems of sound generation. In *Progress in Aerospace Science*. Elsevier, 2004. [9, 63, 109, 113]
- [13] C. Scharam. Hybrid approach for aeroacoustic prediction in confined flows. In *Basics of Aero-Acoustics and Thermo-Acoustics*, J. Anthoine editor, LS 2007-09. von Karman Institute, Rhode-St-Genèse, 2007. [16]

- [14] N. Curle. The influence of solid boundaries upon aerodynamic sound. *Proc. Roy. Soc. Lon.*, A 231:505–514, 1955. [2, 5, 14, 16, 78, 103]
- [15] R. de Kat, B. W. van Oudheusden, and F. Scarano. Instantaneous planar pressure field determination around a square-section cylinder based on time-resolved stereo PIV. In *14th Int Symposium on the Application of Laser Techniques to Fluid Mechanics*, Lisbon, Portugal, July 2008. [69, 70]
- [16] W. De Roeck. *Hybrid methodologies for the computational aeroacoustic analysis of confined, subsonic flows*. PhD thesis, Katholieke Universiteit Leuven, 2007. [113]
- [17] W. Desmet. Boundary element method in acoustics. In *KU-Leuven Lecture series*, KU Leuven press. Leuven, 2006. [113]
- [18] P. di Francescantonio. A new boundary integral formulation for the prediction of sound radiation. *J. Sound and Vibration*, 202:491–509, 1997. [5, 20, 23]
- [19] A. P. Dowling and E. Ffowcs Williams. *Sound and sources of sound*. Cambridge university press, Cambridge, 1982. [20]
- [20] G. E. Elsinga, F. Scarano, B. Wieneke, and B. W. van Oudheusden. Tomographic particle image velocimetry. *Experiments in Fluids*, 41:933–947, 2006. [34, 102]
- [21] J. E. Ffowcs Williams. Aeroacoustics. *Journal of Sound and Vibrations*, 190:564–587, 1996. [5]
- [22] J.E. Ffowcs Williams and D.L. Hawkings. Sound generated by turbulence and surfaces in arbitrary motion. *Proc Roy. Soc. Lon.*, A264:321–342, 1969. [2, 5, 19]
- [23] X. Gloerfelt, F. Prot, C. Bailly, and D. Juv. Flow-induced cylinder noise formulated as a diffraction problem for low Mach numbers. In *Journal of Sound and Vibration*, 287:129–151. ELSEVIER, 2005. [14, 16]
- [24] B. Greschner, F. Thiele, M. Jacob, and D. Casalino. Prediction of sound generated by a rod-airfoil configuration using EASM DES and the generalized Lighthill/FW-H analogy. *Computers & fluids*, 37:402-413, 2008. [3, 78]
- [25] A. Hirschberg and C. Schram. A primitive approach in aeroacoustics. In *Lecture Notes in Physics*, Y. Aurégan, A. Maurel, V. Pagneux, and J.-F. Pinton editors, 586:1–30. Springer-Verlag Berlin Heidelberg, 2002. [10, 11, 16, 78, 79]
- [26] A. Hirshberg. Internal aeroacoustics. In *Advances in aeroacoustics*, J. Anthoine and C. Schram editors, LS 2000-01. von Karman Institute, Rhode-St-Genève, 2001. [1, 9, 119]
- [27] M. S. Howe. *Theory of Vortex Sound*. Cambridge university press, 2003. [1, 10, 16, 20, 24, 44, 103, 119, 120]
- [28] M. Jacob, M. Ciardi, L. Gamet, B. Greschner, Y. J. Moon, and I. Vallet. Assessment of CFD broadband noise predictions on a rod-airfoil benchmark computation. *AIAA, 2008-2899*, 2008. [3]

- [29] M. C. Jacob, J. Boudet, D. Casalino, and M. Michard. A rod-airfoil experiment as benchmark for broadband noise modeling. *Theoretical and Computational Fluid Dynamics*, 19: 171-196, 2004. [3, 56, 64, 67, 95]
- [30] L. Koop. Beamforming methods in microphone array measurements. Theory, practice and limitations. In *Experimental Aeroacoustics*, M. L. Riethmuller and M. R. Lema editors, LS 2007-01. von Karman Institute, German Aerospace Center, Germany, 2006. [41]
- [31] D. F. Kurtulus, F. Scarano, and L. David. Unsteady aerodynamics forces estimation on a square cylinder by TR-PIV. *Experiments in Fluids*, 42:185-196, 2007. [69, 79]
- [32] M. J. Lighthill. On sound generated aerodynamically, part I: General theory. *Proc. Roy. Soc. Lon., A* 211:564-587, 1952. [2, 5, 9, 11, 14]
- [33] *LMS-SYSNOISE Rev.5.6*. LMS International, Interleuvenlaan 68, 3001 Leuven Belgium, first edition, March 2003. [113]
- [34] V. Lorenzoni, M. Tuinstra, and F. Scarano. Combined PIV and acoustic measurements on a rod-airfoil configuration. Pilot test of the FLOVIST project. Technical report, Nationaal Lucht-en Ruimtevaart laboratorium (NLR), 2008. [50, 56, 59, 63, 66, 70]
- [35] P. Martinez, A. Pradera, and C. Schram. Efficient implementation of equivalent sources from CFD data in Curle's analogy. *AIAA*, 224:449-463, 2007. [12, 113]
- [36] P. Moore, H. J. Slot, and B. Boersma. Simulation and measurement of flow generated noise. *Journal of Computational Physics*, 224:449-463, 2007. [111]
- [37] F. K. Nielsen. Measuring good sounds aeroacoustics. In *Experimental Aeroacoustics*, M. L. Riethmuller and M. R. Lema editors, LS 2007-01. von Karman Institute, Brüel & Kjær, Denmark, 2006. [37]
- [38] B. W. van Oudheusden, F. Scarano, E. W. M. Rosenboom, E. W. F. Casimiri, and L. J. Souverein. Evaluation of integral forces and pressure fields from planar velocimetry data for incompressible and compressible flows. *Experiments in Fluids*, 43:153-162, 2007. [69]
- [39] J. F. Piet and G. Elias. Localization of acoustic source from a landing aircraft with a microphone array. *AIAA 99-1811*, 1999. [41]
- [40] A. Powell. Theory of vortex sound. *Journal of the Acoustical Society of America*, 36: 177-195, 1964. [10, 17, 119]
- [41] M. Raffel, C. Willert, S. Wereley, and J. Kompenhans. *Particle Image Velocimetry. A practice guide*. Springer, 2nd edition, 2008. [26]
- [42] M. Roger. Aeroacoustics: some theoretical background – The acoustic analogy. In *Computational Aeroacoustics*, J. Anthoine and T. Colonius editors, LS 2006-05. von Karman Institute, Rhode-St-Genève, 2006. [2]
- [43] M. Roger. Fundamentals of aeroacoustics. In *Experimental Aeroacoustics*, M. L. Riethmuller and M. R. Lema editors, LS 2007-01. von Karman Institute, Rhode-St-Genève, 2006. [2, 3, 6, 22]

- [44] F. Scarano and M. L. Riethmuller. Iterative multigrid approach in PIV image processing. *Experiments in Fluids*, 26:513–523, 1999. [34, 53]
- [45] C. Schram. *Aeroacoustics of subsonic jets: prediction of sound produced by vortex pairing based on particle image velocimetry*. PhD thesis, Tu/e Eindhoven, 2003. [4, 10, 119]
- [46] C. Schram, J. Anthoine, and A. Hirshberg. Calculation of sound scattering using Curle’s analogy for non-compact bodies. *AIAA*, 2007. [11, 16]
- [47] C. Schram, M. Tournour, and P. Martinez. Two dimensional in-duct vortex leapfrogging as a validation benchmark for internal aeroacoustics. *Proceedings of the 13th International Congress of Sound and Vibration*, 224:449–463, 2007. [11]
- [48] W. Schröder, U. Dierksheide, J. Wolf, M. Herr, and J. Kompenhans. Investigation on trailing-edge noise sources by means of high-speed PIV. In *12th international Symposium on Application of Laser Techniques to Fluid Mechanics*, 2004. [4, 103]
- [49] W. Schröder, R. Ewert, T. P. Bui, and E. Gröschel. An LES-APE approach in computational aeroacoustics: Theory and applications. In *Computational Aeroacoustics*, J. Anthoine and T. Colonius editors, LS 2006-05. von Karman Institute, Rhode-St-Genèse, 2006. [2, 9, 109, 110, 112]
- [50] P. Sijtsma. Experimental techniques for identification and characterization of noise sources. In *Experimental Aeroacoustics*, M. L. Riethmuller and M. R. Lema editors, LS 2007-01. von Karman Institute, Rhode-St-Genèse, 2006. [41, 47]
- [51] P. Sijtsma, S. Oerlemans, and H. H. Holthusen. Localization of rotating sources by phased array measurements. *AIAA 2001-2167*, 2001. [41]
- [52] M. J. Stanek, J. A. Ross, J. Odedra, and J. W. Peto. High frequency acoustic suppression - the mystery of the rod-in-crossflow revealed. *AIAA*, 19:171-196, 2004. [1]
- [53] A. Turella. On accuracy assessment of instantaneous planar pressure imaging based on TR-PIV. Master’s thesis, Università degli Studi di Padova, 2008. [69]
- [54] F. M. White. *Viscous fluid flow*. Mc Graw-Hill, 2006. [26]
- [55] C. H. K. Williamson. Vortex dynamics in the cylinder wake. *Annual review of fluid mechanics*, 1996. [3, 62, 66, 68]

Appendix A

Computational aeroacoustics

Analytical solution of the aeroacoustic equations are not available for complex configurations. Noise prediction analysis are often carried out by means of numerical methods referred to as computational aeroacoustics or CAA. While performing acoustic numerical calculations, some relevant aspects have to be taken into account, mainly with regard to memory and accuracy problems, in particular, at low Mach numbers (see [12] and [49]).

Computational fluid dynamics is able to describe very well the hydrodynamic behavior of the flow, at least for limited Reynolds numbers. There is a significant overlap between the CFD techniques used to detect the flow and acoustic propagation algorithms; usually in developing numerical methods for sound generation and propagation problems, it is natural to try to adapt methods generally used in CFD to acoustic purposes.

The major problems connected with CAA methods are the following:

- 1 Noise generation is mainly due to turbulent fluctuations. Numerical procedure as RANS, unsteady RANS or LES involve a filtering process of high frequency and small space fluctuation; the impact of such filtering on the sound prediction is a common research topic.
- 2 Acoustic waves can propagate coherently, without any attenuation for long distances in the flow. Artificial dispersion and dissipation due to numerical schemes can lead to unacceptable attenuations of the sound waves.
- 3 Acoustic radiation efficiency is very low; small numerical errors in the flow calculation can overwhelm the sound field, producing serious overestimates of sound generation; for example truncation of the computation domain can introduce artificial acoustic sources which have to be taken into account for the acoustic prediction.
- 4 The computational domain needed to embrace the acoustic field, extends over large distances. Meshes able to describe simultaneously the fluid domain and the acoustic field, require a very high number of cells, resulting in computationally demanding simulations.

A.1 Computational methods

The numerical methods used for acoustic computations fall under two broad branches on the basis of whether they aim or not at directly describing the unsteady flow and the sound at the same time.

- Direct Methods (DNS, LES, VLES, DES)
- Hybrid Methods (DNS+LEE, LES+BEM, RANS+SNGR, etc.)

A.2 Direct Methods

Direct Methods aim at solving contemporarily the noise-producing flow region and at least a part of the near acoustic field. This purpose is achieved by creating meshes that are able to enclose and describe the characteristic length scales of both the turbulent flow and acoustic waves. The acoustic field can then be extended further away using a coarser cartesian mesh and simplified propagation equation describing the far-field domain, for example linearized Euler equations or (convected) wave equations. Attention must be paid at the interface between the near and the far-field, in order to ensure an accurate and stable information transfer, if different equations are used. Highly accurate interpolation schemes for the meshes are needed. Analytical methods can also be used in the extended region if the flow disturbances satisfy the acoustic wave equation. Kirchhoff and permeable Ffowcs Williams-Hawking can be exploited at the computation domain boundary or, for the second method, on other suitable existing surfaces in the interior of domain. The far-field propagation is then obtained by means of numerical integration of the surface terms, evaluated at appropriate retarded times.

A.2.1 DNS

Direct Numerical Simulation (DNS) consists of solving all the turbulent scales that characterize the flow up to the smallest ones. At a first sight this approach seems extremely convenient because it does not need any modeling and the acoustics is directly computed; there are, however, some limitations to DNS applications, mostly due to memory space, computational time and accuracy (see [49])

If we denote with L the characteristic length of the biggest turbulent eddy (usually comparable to the dimension of the body generating turbulence) and with η the Kolmogorov length scale (dimension of the smallest turbulent scale), the total number of grid points of a 3D uniform mesh is

$$N_{uni} \approx \left(\frac{L}{\eta}\right)^{\frac{3}{4}}.$$

As the Re number increases it can be shown that the Kolmogorov microscale decreases as

$$\left(\frac{L}{\eta}\right) \sim c_f Re^{\frac{3}{4}}.$$

The number of points required for a calculation is thus:

$$N_f \approx c_f Re^{\frac{9}{4}}.$$

For quasi-incompressible flows, i.e. at very low Mach numbers, the problem further deteriorates. The acoustic wavelength lengthens with decreasing the acoustic Mach number $Ma = \frac{L}{\lambda_a}$. In order to capture a sufficient number of wavelength for the acoustic description, the computation domain has to be extended over a wider space. It implies conspicuous additional amount of mesh points and high computational costs. The application of DNS has been limited to simple flow configurations.

Formidable, although expensive, Direct Numerical Simulation on free-jet flow configuration has been successfully performed by Peter Moore at the TUDelft in 2005 [36], for high subsonic Mach number on an a mesh of over 10^8 grid point, combined with permeable Ffowcs Williams-Hawkings analogy for the acoustic propagation.

A.2.2 LES

In a Large Eddy Simulation method only the big turbulent scales, which are responsible for most of the sound production, are directly resolved. The basic conservation equation are filtered from the smallest scales. Usually the filter size corresponds to the size of smallest mesh cell or, in presence of a body, it is often weighted with the normal wall coordinate y^+ . The effect of the sub-grid scales (SGS), more statistically isotropic, is accounted for by sub-grid models: Smagorinsky, Dynamic Smagorinsky, WALE. The hypothesis behind the introduction of LES for CAA is that larger scales are more effective than small ones to noise radiation. The contribution of sub-grid scales on the total radiation is still an open question. The computational costs of LES simulation, however, remains relatively high.

A.2.3 RANS

The flow variables and the Navier-Stokes equations are time averaged over a period that is short compared to the flow time evolution, but large compared to the time-scale of the turbulent fluctuations. The effect of turbulent fluctuations is accounted for through a so called turbulence model. The most used models are: Reynold's stress model, $\kappa - \epsilon$, $\kappa - \omega$.

A.2.4 DES

In presence of a solid body in the flow domain the need for smaller cells near the solid surface brought into the idea of combining a RANS modeling for the attached boundary layers together with a LES method for the separated region flow field. This mixed LES-RANS method is called Detached Eddy Simulation (DES). It fastens the calculations because it allows the use of a relative courser mesh for the LES; the RANS model does not spoil the accuracy of the discretization since its application is confined to fairly isotropic small structure, which can be well enough modeled through a Reynold-stress formulation. The effects of this approach on the acoustic prediction is still under investigation.

A.3 Hybrid Methods

The description of the flow field in Hybrid Methods does not include the sound propagation and a second calculation is used for the acoustic prediction.

A.3.1 LEE

A possible approach to extend the near-field compressible flow data to the radiated acoustical field is the numerical implementation of linearized Euler equations (LEE); acoustic propagation, being an isentropic inviscid process, allows the use of Euler equations in which viscosity is neglected; the small amplitude of acoustic oscillations, regard to the main flow, further allows linearization (for SPL below 140 dB, i.e. $p' = 0.02P_0$). These equations are then numerically resolved in a courser acoustic mesh overlapping the flow source domain and extending to the propagation region.

The main problem connected with LEE stems from the fact that they admit non-trivial instability wave solutions of the homogeneous equations. Vorticity and entropy modes are convected as well as acoustic waves. They give no problem as long as the source terms due to field nonlinearities, viscosity effects or external sources do not excite these modes. If excitation occurs the these instabilities grow and even small errors in boundary definitions or mesh non-uniformities can reflect them into radiating acoustic waves, spoiling the acoustic prediction. A feasible solution to overcome instability problems is the use of APE equations.

A.3.2 APE

The acoustic perturbation equations (APE) are obtained in the same way as LEE from a linerization of inviscid Navier-Stokes equations. An additional irrotational assumption is made for the acoustic velocity field. They can be obtained with a decomposition of Crocco's theorem. Four different APE can be distinguished depending on the variable used to describe the acoustic field ([49]). This set of equation, unlike the LEE, is shown to render perfectly stable solutions.

A.3.3 SNGR

Computational cost can be highly reduced by the use of steady-RANS CFD calculations in lieu of LES or DES. Stochastic Noise Generation Method allows the prediction of broadband noise using steady RANS results. Steady fluid data do not contain by themselves information about the acoustic phenomena. The time variation of the turbulence is reconstructed by means of a combination of random Fourier modes. The use of random Fourier modes is justified by the assumption of stochastic turbulence.

LES simulations usually lack a description of the high frequency acoustic contribution of the small turbulent scales removed by the filtering process. Attempt is made to combine LES for middle-low turbulent scales description with SNGR aiming at describing the effect of smaller turbulent scales. A new software for SNGR acoustic prediction, has been developed by the company TNO in Delft. Turbulent kinetic energy, velocity vector and decay rate are calculated through a RANS simulation, the spatial wave-number spectrum is modeled according to a Von-Karman spectral distribution. Anti-transformation of the Fourier spectrum is performed with statistic phase shifts. The time evolution of the turbulence is then solved using a convection equation that also accounts for the turbulence decay rate. The hydrodynamic fluctuations are, finally, rearranged as source terms of LEE equations. Numerical integration of LEE equations defines the radiated sound.

A.3.4 BEM

Once acoustic sources have been detected by a CFD computation, the sound pressure in the far-field can be estimated using a Boundary Integrals formulation. The sound waves propagation equations are integrated over the surfaces enclosing the acoustic domain. The pressure contribution at a given position inside the domain is determined by the pressure and velocity contribution on solid bodies inside the domain. The integrals can be discretized using polynomial series expansion. BEM methods together with FEM method are particularly suitable for vibro-acoustic problems [17]. Modern softwares for noise prediction like Sysnoise or Virtual-Lab [33], developed at the company LMS, are based on BEM or FEM discretization techniques. The cited softwares have been used by the author, together with an LES simulation, for an aeroacoustic investigation of a duct-flow at the company LMS in Leuven.

A.3.5 Boundary Conditions

A still open challenge in CAA methods is the estimation of proper boundary conditions. Colonius and Lele [12] underline the strong influence of the mesh discretization at interface between fluid domain and acoustic domain, in order to include all the information needed when using for example a Kirchhoff approach. Particular attention must be paid to the truncation of the source domain, which can introduce further acoustic spurious sources as discussed by P. Martinez in [35].

To the knowledge of the author active research is currently carried out at the KU-Leuven for implementation of time-varying boundary conditions for LEE solvers.

A.3.6 Discretization Methods

The specific features associated with sound wave propagation require an extension of the common CFD codes towards more specific applications, accurate enough to account for the high dispersive and dissipative character of aero-acoustic simulations.

The currently most used discretization techniques in CAA studies are:

- FD(Finite Difference)
- DG (Discontinuous Galerkin)

Finite Difference Method The great advantages of FD schemes are the simple implementation and the ease of extending them to higher order accuracy. High order schemes are, however, extremely sensitive to the generation of spurious high-frequency waves. In order to provide a remedy for incorrect or even unstable results due to *spurious waves*, artificial dissipation, artificial viscosity or explicit filtering are usually applied [12, 16]. The problem associated with FD methods is that they can be implemented only on structured meshes and, as a consequence, only on relatively simple geometries.

Discontinuous Galerkin's Method DG method, similar to Finite Element Methods, is based on high-order polynomial basis functions. The fluxes between internal elements, instead of being determined by a continuity condition as in FEM schemes, are calculated in DG

solving an approximated Riemann problem. This produces more compact discretization that is amenable for larger meshes, usually needed in acoustic problems. This method can be applied on non-structured meshes, still giving accurate results; boundary conditions can be easily implemented, the order of accuracy easily increased and parallelization simply applied. The use of DG method is likely to increase in the CAA field, where complex geometries are often involved.

Appendix B

Basics of Signal Processing

The purpose of the present chapter is to offer a general description of the relevant statistical quantities and techniques used during the investigations.

B.1 Relevant Statistical Quantities

A signal is the time evolution of the state of a system. When the studied signal is random a measured time record will give incomplete information to fully analyze the signal. The collection of time histories $x_i(t)$ defines the ensemble of the random process. The *moments* of the statistical process are the quantity used to describe the phenomenon. If the probability density function $p(x)$ for a stochastic variable is known, the different statistical moments can be calculated using the *expected value* operator also known as E-operator

$$E[g(x)] = \int_{-\infty}^{+\infty} g(x)p(x)dx, \quad (\text{B.1})$$

where $g(x)$ is a single valued function of x .

The statistical moments can be calculated as

$$\mu_n = E[x^n] = \int_{-\infty}^{+\infty} x^n p(x)dx. \quad \text{for } n = 1, 2, 3...$$

The signal $x(t)$ is called ergodic if the statistical quantities calculated on a single time ensemble coincide with the ones calculated over the entire time history.

For stationary ergodic signals the most common statistical moments are:

$$\begin{aligned} \mu &= E[x(t)] = \lim_{T \rightarrow \infty} \frac{1}{T} \int_0^T x(t)dt, \\ \phi^2 &= E[x^2(t)] = \lim_{T \rightarrow \infty} \frac{1}{T} \int_0^T x^2(t)dt, \\ \sigma^2 &= E[(x(t) - \mu)^2] = \lim_{T \rightarrow \infty} \frac{1}{T} \int_0^T (x(t) - \mu)^2 dt. \end{aligned}$$

The first quantity μ is called *Mean Value*, ϕ^2 the *Mean Square* and σ^2 the *Variance*. The square root of the mean square is often used as an indicator of the amplitude of fluctuating quantities, it is called the *r.m.s Value* or *Root Mean Square* and formally reads

$$r.m.s[x(t)] = \sqrt{\frac{1}{T} \int_0^T x^2(t)dt}. \quad (\text{B.2})$$

For signal with zero mean the r.m.s value coincides (apart from the denominator) with the *Standard Deviation* that is a widely used quantity in statistics. Higher order moments are indicators of the symmetry of the signal around the mean (3rd *skewness*) or the presence of spikes and transients (4th *kurtosis*).

B.2 Correlations and Spectra

Cross correlation functions give an indication of the periodicity of a certain phenomenon in its domain of definition. In case of time signal it indicates how well future events can be predicted using past observation, while in space domain it describes the main disposition of a specific structure. The following discussion refers to time signals but the same concepts apply to spatial domain as in case of PIV evaluations.

The general formulation of cross correlation function of two mono-dimensional continuous time signals $x(t)$ and $y(t)$ is defined as:

$$R_{xy}(\tau) = \lim_{T \rightarrow \infty} \frac{1}{T} \int_{-\frac{T}{2}}^{\frac{T}{2}} x(t)y(t + \tau)dt. \quad (\text{B.3})$$

Cross-correlation of sinusoidal signals with the same frequency produces a periodic function with the same frequency of the signals. Sinusoidal signals with different frequencies cancel out because of orthogonality of the sine functions. In case that $x(t) = y(t)$ the function $R_{xy}(\tau) = R_{xx}(\tau)$ is called auto-correlation function.

$$R_{xx}(\tau) = \lim_{T \rightarrow \infty} \frac{1}{T} \int_{-\frac{T}{2}}^{\frac{T}{2}} x(t)x(t + \tau)dt. \quad (\text{B.4})$$

It is clear that for $\tau = 0$

$$R_{xx}(0) = (r.m.s[x(t)])^2.$$

If the signals $x(t)$ and $y(t)$ are subtracted by their mean values, respectively μ_x and μ_y , the resulting correlation function of often called *Covariance* and reads

$$R_{xy}(\tau) = \lim_{T \rightarrow \infty} \frac{1}{T} \int_{-\frac{T}{2}}^{\frac{T}{2}} (x(t) - \mu_x)(y(t + \tau) - \mu_y)dt. \quad (\text{B.5})$$

The Fourier transform of the correlation function is called *Power Spectral Density*(PSD) and is defined as

$$S(f) = \int R_{xx}(\tau)e^{-2i\pi f\tau}d\tau. \quad (\text{B.6})$$

The power spectrum is a real quantity since $R_{xx}(\tau)$ is an even function of τ , it is positive (or zero) for all frequencies and is an even function of the frequency f . If the signal has physical dimension, e.g. $[x(t)] = [L]$ the dimensional units of the PSD are $[\frac{L^2}{Hz}]$.

An equivalent method to calculate cross-correlation functions, which is usually adopted in PIV processing, relies on the definition of the PSD and the Wiener-Khinchin relationship

$$S_{xx}(f) = \lim_{T \rightarrow \infty} \frac{1}{T} E [\|X_k(f, T)\|^2], \quad (\text{B.7})$$

where E indicates the expected value and $X_k(f, T)$ the Fourier transform of the signal $x(t)$ on the ensemble time T .

Parseval's relation provides an important connection between the energy of the signal in time domain and in frequency domain

$$\int_{-\infty}^{+\infty} x^2(\tau) d\tau = \frac{1}{2\pi} \int_{-\infty}^{+\infty} \|X_k(f, T)\|^2 d\omega. \quad (\text{B.8})$$

The Power Spectrum, energy content per bandwidth, and the r.m.s. values in discrete form are related as

$$(r.m.s.)^2 = \sum P(K) \Delta f = \sum \|X_k(f, T)\|^2, \quad (\text{B.9})$$

in which Δf indicates the frequency band on which each component of the spectrum is calculated.

B.3 DFT and FFT

Analogously to the continuous case a transformation of the a discrete signal $x(n\Delta t)$ defined on the interval $T = N\Delta t$ from time domain into frequency domain is possible. The operation is called Discrete Fourier Transform and reads

$$X_k(f, T) = \frac{1}{N\Delta t} \sum_{N=0}^{N-1} x(n) e^{-i2\pi \frac{1}{N\Delta t} n\Delta t} = \frac{1}{N} \sum_{N=0}^{N-1} x(n) e^{-\frac{i2\pi nk}{N}}. \quad (\text{B.10})$$

The number of discrete frequencies of the DFT equals the number of time samples on which $x(n)$ is defined. The frequency resolution of the transformation is the frequency interval between two following frequencies corresponding to $f_0 = \frac{1}{T}$ with T indicating the ensemble time.

The Fast Fourier Transform (FFT) algorithm, developed by Cooley and Tukey in the 1970's, speeds up the computation of DFT. The number of operation for an common N point DFT is N^2 where each operation consists of one complex multiplication and one summation. The FFT algorithm first splits the total amount of samples into two sub-blocks of $\frac{N}{2}$ samples and applies a Discrete Fourier transform to each sub-block. This would take $2 \left(\frac{N}{2}\right)^2$ operation. Recombining the DFT of the 2 sub-blocks would cost N operations. The splitting can be applied recursively over the sub-blocks; it is evident that the efficiency increases when the total number of samples N is a power of 2, which is usually the case for A/D converters. The total number of operation can be shown to be reduced from N^2 to $N \log_2 N$ which correspond to more 90% reduction of the total computational time.

B.4 Spectrum computation algorithm

The spectra shown in the the present work are calculated using a routine developed by the author, based on Welch algorithm [7]. The steps followed for the computation of the PSD are:

1. Subdivision of the signal in blocks (with optional overlap factor)

2. Windowing of each block to avoid leakage using Hanning, Blackharris or Gaussian windows
3. FFT calculation for each windowed block
4. Evaluation of the Power Spectrum Density as product of complex conjugate FFTs
5. Amplitude correction for windowing
6. Average over all the blocks
7. Bandwidth transformation to the required resolution

The PSD gives a measure of the energy contained in each bandwidth of dimension equal to the frequency resolution of the DFT.

B.5 Data filtering

The velocity data obtained from WIDIM have been spatially filtered using a least-square regression method on a cubic function of kernel 2 in (x and y) direction. The shadow regions on the back of the airfoil where no data were available have been reconstructed by an interpolation method based on least-squares regression for each time step.

Appendix C

Theory of Vortex Sound

A. Powell in 1994 [40] developed an alternative analogy formulation for low Mach number flows called *Vortex Sound Theory* in which the source term is constituted by pure kinematic quantities. Howe [27] further proposed a generalization to wall-bounded flows for arbitrary Mach numbers. Howe assumed a potential flow as reference state and considered the total enthalpy perturbation $B' = B - B_0$ as propagation variable. For non vibrating bodies at relative high Reynolds numbers (for which viscous effects can be neglected) the acoustic radiation in the far-field is determined by the equation

$$\frac{p}{\rho_0}(\mathbf{x}, t) = - \int_{V_y} (\boldsymbol{\omega} \times \mathbf{v})(\mathbf{y}, \tau) \cdot \frac{\partial G}{\partial \mathbf{y}}(\mathbf{x}, \mathbf{y}, t - \tau) dV d\tau, \quad (\text{C.1})$$

using the properties of the Green's function, equation (C.1) can be rearranged leading to the definition of the Powell-Howe source term

$$\rho_0 \nabla \cdot (\boldsymbol{\omega} \times \mathbf{v}).$$

The quantity $(\boldsymbol{\omega} \times \mathbf{v})$ is known as Lamb vector and can be seen as the Coriolis acceleration experienced by an observer moving with the flow. The time (-space) variation of the Lamb vector indicates vortex deformation and is the mechanism responsible for sound generation. Potential flows are silent, as stressed by Hirshberg in [26]. Deviation from potential flow behavior is due to injection of rotational fluid from the viscous boundary layer into the main flow. The sentence of Miller and Obermeier (1988): "*Vortices are the voice of a flow*" highlights the importance of vorticity in the sound generation process. The mechanism of boundary layer separation and vortex release that takes place on the vocal folds is responsible for the speech.

For low Mach number flows it is possible to demonstrate the equivalence of the dipolar Powell-Howe source term with the quadrupolar Lighthill's stress tensor. The main advantage of the Vortex sound Theory (see Schram [45]), however, is that the region where vorticity is not vanishing is much more confined than the sound source of Lighthill. Howe carried out analytical derivations of the noise emission for several geometric configurations. The presence of the bodies is accounted for by introduction of the so called *Compact Green's function* usually derived from Conformal Mapping transformations [6].

For two dimensional potential flows the velocity components can be rewritten respectively as: $u = \frac{\partial \varphi}{\partial x}$ and $v = \frac{\partial \varphi}{\partial y}$. For a solenoidal field the velocity can be expressed by means of the

Lagrangian stream function Ψ as $u = \frac{\partial\Psi}{\partial y}$ and $v = -\frac{\partial\Psi}{\partial x}$. For an incompressible irrotational flows the previous relations are both satisfied such that $\frac{\partial\varphi}{\partial x} = \frac{\partial\Psi}{\partial y}$ and $\frac{\partial\varphi}{\partial y} = -\frac{\partial\Psi}{\partial x}$. The last relations are known as the Cauchy-Riemann conditions which are necessary and sufficient for the function $\varphi + i\Psi$ to be an *analytic* or ('regular') function of $z = x + iy$. The real functions φ and Ψ are conjugate functions. We can define a complex potential

$$w(z) = \varphi + i\Psi.$$

Every function of z , irrespective of its form, can be interpreted as complex potential and a description of a possible irrotational incompressible flow in two dimensions. Only particular choices of the function lead to flow descriptions that are acceptable from a physical point of view. This is the basis of the Conformal Mapping technique which has been widely used for analytical descriptions of potential flow patterns around airfoils and other geometries (see Howe and Batchelor [27],[6]).

